University of Tennessee, Knoxville

TRACE: Tennessee Research and Creative Exchange

Doctoral Dissertations

Graduate School

5-2018

Probing the Interfaces of Semiconducting Nanoparticles using Sum Frequency Generation: Instrumentation Development and Design

Brianna Renee Watson
University of Tennessee, bwatso15@vols.utk.edu

Follow this and additional works at: https://trace.tennessee.edu/utk_graddiss

Recommended Citation

Watson, Brianna Renee, "Probing the Interfaces of Semiconducting Nanoparticles using Sum Frequency Generation: Instrumentation Development and Design. " PhD diss., University of Tennessee, 2018.
https://trace.tennessee.edu/utk_graddiss/4951

This Dissertation is brought to you for free and open access by the Graduate School at TRACE: Tennessee Research and Creative Exchange. It has been accepted for inclusion in Doctoral Dissertations by an authorized administrator of TRACE: Tennessee Research and Creative Exchange. For more information, please contact trace@utk.edu.

To the Graduate Council:

I am submitting herewith a dissertation written by Brianna Renee Watson entitled "Probing the Interfaces of Semiconducting Nanoparticles using Sum Frequency Generation: Instrumentation Development and Design." I have examined the final electronic copy of this dissertation for form and content and recommend that it be accepted in partial fulfillment of the requirements for the degree of Doctor of Philosophy, with a major in Chemistry.

Tessa R. Calhoun, Major Professor

We have read this dissertation and recommend its acceptance:

Bin Hu, Sharani Roy, Michael J. Sepaniak

Accepted for the Council:

Dixie L. Thompson

Vice Provost and Dean of the Graduate School

(Original signatures are on file with official student records.)

Probing the Interfaces of Semiconducting Nanoparticles using Sum Frequency Generation:
Instrumentation Development and Design

A Dissertation Presented for the
Doctor of Philosophy
Degree
The University of Tennessee, Knoxville

Brianna Renee Watson
May 2018

Copyright © 2018 by Brianna Renee Watson
All rights reserved.

DEDICATION

"Give her another hundred years, I concluded, reading the last chapter – give her a room of her own and five hundred a year, let her speak her mind and leave out half that he puts in now, and she will write a better book one of these days."

Virginia Woolf, *A Room of One's Own*

To Tom Mori and my parents, Lesle and Gary, for your love and support.

ACKNOWLEDGEMENTS

First acknowledgements go to both Dr. Tessa Calhoun and Dr. Benjamin Doughty for your advisement, guidance, and encouragement through this process. You both have expanded my understanding of science, teaching, writing, collaboration, and diplomacy.

Second acknowledgements are to the friends and colleagues I have gained during my time at the University of Tennessee. Those include the group members and post-doctoral scholars that have leant me advice and wisdom at different points. Special acknowledgement goes to Maggie Lookado, Derek Mull, Graham Collier, Kristina Vailonis, and Lindsey Miller who have been great colleagues and friends to me and without you this would have been a less enjoyable experience.

Final acknowledgements are to the Department of Chemistry at the University of Tennessee for providing teaching assistantships and the UT-ORNL Science Alliance Joint Directed Research and Development Program for providing funding during the completion of this degree.

ABSTRACT

Since the inception and the development of high power lasers, nonlinear spectroscopy and microscopy have been pushing the boundaries for optical techniques. These techniques have changed how we understand emerging materials and revolutionized imaging capabilities. Herein is presented work which aimed to produce electronic sum frequency generation (eSFG) using a photonic crystal fiber (PCF) and Ti:Sapphire femtosecond laser as the light sources while using objective-based total internal reflectance within a microscope apparatus. The large aim of this work was to apply this instrument to study the surfaces of cadmium selenide (CdSe) quantum dots (QDs). Quantum dots have emerged as a flexible and useful material for light harvesting and light emitting applications, including television screens, lighting diodes, biomedical imaging probes, catalytic substrates, and solar panel application. Despite the current applications of these QDs, the material still exhibits deleterious flaws mostly due to the lack of control over their surface properties. While there are continuous strides in this field of research, the work here aimed to provide a better understanding of these surfaces in order to incubate further advances. The instrument described above observed electronic structure within the mid-band gap region which has previously proven difficult to study. Since the electronic properties of CdSe QDs are so intricately connected to the ligand or shell attached to the nanocrystal surface, the study the CdSe QD surfaces was furthered by vibrational sum frequency generation spectroscopy (vSFG) to better understand the ordering and presence of ligands at the QD interface. This instrument has not only been applied to CdSe QDs but other light harvesting materials, specifically inorganic-organic lead based perovskite films. A two-photon total internal reflectance based microscopy was able to reveal dipole orientations of the perovskite film and shows sensitivity to the films topography. Together these studies show the flexibility of this instrument to study important electronic properties effecting the application of light sensitive materials.

TABLE OF CONTENTS

LIST OF TABLES

LIST OF FIGURES

CHAPTER 1 ♦ INTRODUCTION

Broader Context

Nanomaterials are a vast and engaging field with seemingly unlimited potential for changing the face of energy harvesting, catalysis, biological imaging, and medical treatment.[1-4] As such materials continue to emerge and current ones evolve, there is a ubiquitous need to also advance techniques to further characterize nanomaterials. The surface properties and interfacial interactions of these nanomaterials are critical to their characterization considering the inherent size of the materials. In connection with this is the need to also understand the electronic structure at these interfaces since some of the most captivating properties of nanomaterials for chemical use includes light emission and electron transfer. Current techniques struggle to address these questions because such properties tend to be obscured in bulk, ensemble measurements due to a broad range of sites, chemical environments, and surface dissimilarities.

Nonlinear Optical Techniques

The progress of this dissertation has been dependent on the understanding and implementation of nonlinear optical processes thus it is appropriate to introduce each of the optical techniques utilized in this work. Those include one-photon fluorescence (OPF), two-photon fluorescence (TPF), second harmonic generation (SHG), and sum frequency generation (SFG). For reference, all techniques discussed in this introduction are shown in the energy diagram (Figure 1.1).

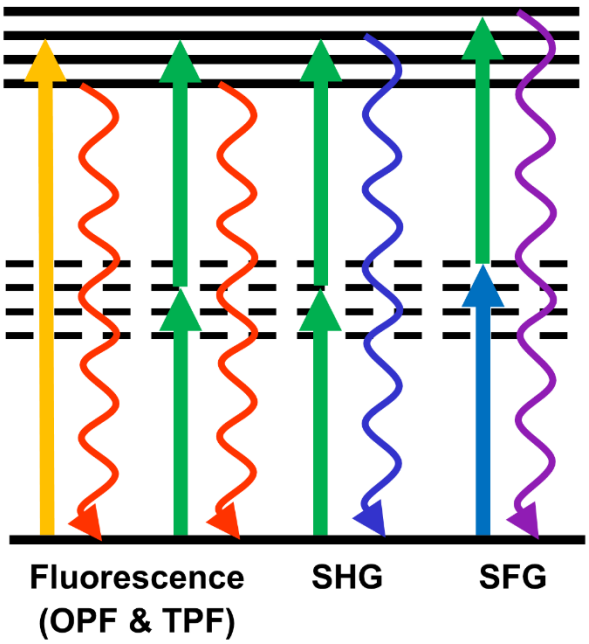

Figure 1.1 Jablonski diagram for nonlinear optical processes

Two-Photon Fluorescence

Fluorescence is the red-shifted emission associated with the absorption of light to an excited state. In two-photon fluorescence, two photons are needed to reach the same excited state. Two-photon fluorescence thus results in an emission wavelength shorter than the excitation wavelength. For example, two excitation pulses of 800 nm can produce an emitted wavelength of 600 nm. In Figure 1.1, one-photon fluorescence (OPF) and two-photon fluorescence (TPF) are illustrated to represent these differences. The phenomenon of two-photon absorption was first predicted by Maria Goeppert-Mayer from her doctoral dissertation work in 1931.[5] It would take decades and the development of laser technology to prove her doctoral work correct. Two-photon absorption relies on high energy fluence in order to achieve it. This is typically achieved with pulsed laser systems which produced pulsed light with a higher peak power than average power. Most commonly these pulsed laser system are femtosecond Ti:Sapphire laser; however, it has been shown that nanosecond, picosecond or even high power CW laser can induced two-photon absorption.[6] Two-photon fluorescence has become a popular technique for the biomedical fields and brought improvements to the microscopy community including decreased focal volume and increased resolution.[5-6]

Sum Frequency Generation

Sum frequency generation (SFG) is a coherent, nonlinear technique based on two incident photons at frequencies, ω_1 and ω_2, combining to produce a photon of summed frequency ($\omega_1 + \omega_2$), as illustrated on the right in Figure 1.1. When those incident frequencies are the same frequency the process is commonly referred to as second harmonic generation (SHG). The interaction of the two frequencies and material induces a polarization within the material which can be described by equation 1, where $\chi^{(1)}$ and $\chi^{(2)}$ are the first and second order susceptibility tensor, respectively, and E represent an electric field.[7] The second order term of equation 1 is responsible for the sum frequency generation while the first term is linear absorption and similar order light matter interactions. The equation can extend to higher order terms which represent higher order processes as well.

$$P = \chi^{(1)}E^1 + \chi^{(2)}E^2 \tag{1}$$

As shown below in equation 2, the intensity of the SFG signal is based on the nonsusceptibility tensor, χ, and the electric fields present at the sample, E.

$$I_{SFG}(\omega) \propto \left(\chi^{(2)}E_1E_2\right)^2 \tag{2}$$

Due to the dependence of sum frequency generation on the input electric fields, like TPF, high energies are necessary. For SFG, picosecond or femtosecond systems are typically utilized. The femtosecond systems produce peak powers between megawatts and gigawatts depending on the repetition rate and pulse width of the laser system.[8] SFG differs from two-photon fluorescence in two important features. It is a parametric process and thus does not result in shifts in the emission wavelength and the process is coherent producing specific phase matching conditions which effect signal interference and the

signal propagation. SFG, therefore SHG, is only achievable in noncentrosymmetric systems (structures with no inversion symmetry) thus restricting the number of materials that will produce signal. This can be proven mathematically for the nonsusceptibility tensor, shown in equation 2, which cancels when inversion symmetry is present.[9] Additionally, the bulk nonlinear susceptibility tensor can be related to molecular properties through equation 3.[7, 10] Equation 3 shows how the bulk nonsusceptibility tensor, $\chi^{(2)}$, relates to the density of molecules and the orientational average, as indicated by the brackets, of the hyperpolarizability of the individual molecules, β.

$$\chi^{(2)} = N_s\langle\beta\rangle \tag{3}$$

From equation 3 it can be understood that harmonophores, molecules which produce SHG or SFG, must have a permanent dipole moment and must be orientated so to maintain noncentrosymmetry in the system.

Despite the symmetry conditions SFG and SHG have been performed in many experimental setups and applied to a number of systems including both biological and material. The symmetry restrains of this optical process makes the technique sensitive to surfaces, due to the immediate break in symmetry occurring at a surface boundary, and is considered a surface selective technique for this reason and is commonly implemented in this matter. The most common type of SFG spectroscopy utilized is vibrational sum frequency generation (vSFG) which has one of the incident frequencies on resonance with a vibrational transition of interest. For electron sum frequency spectroscopy (eSFG) one of the incident frequencies or both of the incident frequencies is in resonance with an electronic transition. As shown in equation 4 for vSFG, the intensity of the SFG signal at certain IR frequencies is also dependent on both nonresonant signal (A_{NR}) and resonant signal which is related the frequency of the transition j.[11]

$$I_{SFG}(\omega_{IR}) \propto \left| A_{NR}e^{i\varphi} + \sum_{j=1}^{N} \frac{A_j}{(\omega_{IR}-\omega_j)+\Gamma_j} \right|^2 \tag{4}$$

When the input frequencies are resonant with a state, signal enhancement occurs. Of the two versions of the technique vibrational sum frequency has been further explored providing more prolific literature on the topic.[11-15] Electronic sum frequency has been performed less commonly but there are examples in the literature.[16-20]

Research Outcomes

The work presented in this dissertation aimed to develop a new technique to characterize the surface states of CdSe quantum dots. In order to achieve this, a microscope apparatus was designed for both epi-direction imaging and through direction microspectroscopy. The development of this instrument was centered on the nonlinear processes occurring in an objective based total internal reflectance excitation field. The nonlinear processes capable for this instrument include two-photon fluorescence, second harmonic generation, and sum frequency generation.

Chapter one of this work details the design and implementation of the eSFG instrument. This chapter emphasizes on design elements, calibration, and data analysis used for producing eSFG spectra. Chapter two addresses the microscopy capabilities of the instrument as applied to lead-based perovskite films by utilizing two-photon fluorescence. Work in this chapter highlights the total internal reflection illumination geometry sensitivity to dipole moment as well as topography of the sample. Chapter three concerns the eSFG signal from CdSe QDs. From this chapter, it is observed that eSFG is capable of providing important information about the electronic states present in CdSe QDs. The eSFG spectra identified the mid-band gap states not seen in UV-Vis measurements and observe an increase in these mid-band gap states with air exposure. Chapter four addresses studying the ligand at the surface of CdSe QDs with vSFG. By using the vibrational equivalent process to study these quantum dots, it was shown that sum frequency can be applied to not only understand electronic structure but also the arrangement of ligands at the surface. Thus, these techniques can provide insight to the surface of the materials as a whole.

References

1. Kim, J. Y.; Voznyy, O.; Zhitomirsky, D.; Sargent, E. H., 25th Anniversary Article: Colloidal Quantum Dot Materials and Devices: A Quarter-Century of Advances. *Advanced Materials* **2015**, *27*, 3849-3849.
2. Gross, E.; LiuJack, H.-C.; Toste, F. D.; Somorjai, G. A., Control of Selectivity in Heterogeneous Catalysis by Tuning Nanoparticle Properties and Reactor Residence Time. *Nat Chem* **2012**, *4*, 947-952.
3. Green, M.; Howes, P.; Berry, C.; Argyros, O.; Thanou, M., Simple Conjugated Polymer Nanoparticles as Biological Labels. *Proceedings of the Royal Society of London A: Mathematical, Physical and Engineering Sciences* **2009**, *465*, 2751-2759.
4. Dreaden, E. C.; Alkilany, A. M.; Huang, X.; Murphy, C. J.; El-Sayed, M. A., The Golden Age: Gold Nanoparticles for Biomedicine. *Chemical Society Reviews* **2012**, *41*, 2740-2779.
5. Masters, B. R.; So, P. T. C., *Handbook of Biomedical Nonlinear Optical Microscopy*; Oxford Univerity Press, 2008.
6. So, P. T. C., Two-Photon Fluorescence Light Microscopy. In *Els*, John Wiley & Sons, Ltd: 2001.
7. Chen, X.; Nadiarynkh, O.; Plotnikov, S.; Campagnola, P. J., Second Harmonic Generation Microscopy for Quantitative Analysis of Collagen Fibrillar Structure. *Nature Protocols* **2012**, *7*, 654.
8. Rulliere, C., *Femtosecond Laser Pulses*, 2nd ed.; Springer, 2005.
9. Boyd, R. W., *Nonlinear Optics*; Academic Press, 2002.
10. Moad, A. J.; Simpson, G. J., A Unified Treatment of Selection Rules and Symmetry Relations for Sum-Frequency and Second Harmonic Spectroscopies. *The Journal of Physical Chemistry B* **2004**, *108*, 3548-3562.
11. Bordenyuk, A. N.; Weeraman, C.; Yatawara, A.; Jayathilake, H. D.; Stiopkin, I.; Liu, Y.; Benderskii, A. V., Vibrational Sum Frequency Generation Spectroscopy of Dodecanethiol on Metal Nanoparticles. *The Journal of Physical Chemistry C* **2007**, *111*, 8925-8933.
12. Allhusen, J. S.; Kimball, D. R.; Conboy, J. C., Structural Origins of Cholesterol Accelerated Lipid Flip-Flop Studied by Sum-Frequency Vibrational Spectroscopy. *The Journal of Physical Chemistry B* **2016**, *120*, 3157-3168.
13. Baldelli, S.; Eppler, A. S.; Anderson, E.; Shen, Y.-R.; Somorjai, G. A., Surface Enhanced Sum Frequency Generation of Carbon Monoxide Adsorbed on Platinum Nanoparticle Arrays. *The Journal of Chemical Physics* **2000**, *113*, 5432-5438.
14. Barrett, A.; Petersen, P. B., Order of Dry and Wet Mixed-Length Self-Assembled Monolayers. *The Journal of Physical Chemistry C* **2015**, *119*, 23943-23950.
15. Frederick, M. T.; Achtyl, J. L.; Knowles, K. E.; Weiss, E. A.; Geiger, F. M., Surface-Amplified Ligand Disorder in Cdse Quantum Dots Determined by Electron and Coherent Vibrational Spectroscopies. *Journal of the American Chemical Society* **2011**, *133*, 7476-7481.
16. Moon, A. P.; Pandey, R.; Bender, J. A.; Cotton, D. E.; Renard, B. A.; Roberts, S. T., Using Heterodyne-Detected Electronic Sum Frequency Generation to Probe the

Electronic Structure of Buried Interfaces. *The Journal of Physical Chemistry C* **2017**, *121*, 18653-18664.
17. Pandey, R.; Moon, A. P.; Bender, J. A.; Roberts, S. T., Extracting the Density of States of Copper Phthalocyanine at the Sio2 Interface with Electronic Sum Frequency Generation. *The Journal of Physical Chemistry Letters* **2016**, *7*, 1060-1066.
18. Sen, P.; Yamaguchi, S.; Tahara, T., Ultrafast Dynamics of Malachite Green at the Air/Water Interface Studied by Femtosecond Time-Resolved Electronic Sum Frequency Generation (Tr-Esfg): An Indicator for Local Viscosity. *Faraday Discussions* **2010**, *145*, 411-428.
19. Yamaguchi, S.; Tahara, T., Development of Electronic Sum Frequency Generation Spectroscopies and Their Application to Liquid Interfaces. *The Journal of Physical Chemistry C* **2015**, *119*, 14815-14828.
20. Raschke, M. B.; Hayashi, M.; Lin, S. H.; Shen, Y. R., Doubly-Resonant Sum-Frequency Generation Spectroscopy for Surface Studies. *Chemical Physics Letters* **2002**, *359*, 367-372.

CHAPTER 2 ♦ SHEDDING LIGHT ON SURFACE EFFECTS: NONLINEAR PROBE OF COMPLEX MATERIALS

A version of this chapter was submitted as proceeding manuscript for SPIE Defense and Commercial Sensing conference from April 15-19th, 2018 in Orlando, Florida.

Brianna R. Watson, Benjamin Doughty, Tessa R. Calhoun, "Shedding Light on Surface Effects: Nonlinear Probe of Complex Materials," Proc. SPIE 10638, Ultrafast Bandgap Photonics III, 10638-22

This chapter describes instrument design, data collection, and data analysis performed by Brianna R. Watson. Benjamin Doughty, and Tessa R. Calhoun advised this work through the entire process.

Abstract

The refinement of materials to facilitate their use in a broad range of applications is dependent on a detailed characterization and understanding of their interaction with light. This is especially true for the properties of materials' surfaces and interfacial regions where deviations from the bulk structure significantly impact the flow of energy. Adding to the complexity of this problem is the fact that these regions contain an overall small number of reporters resulting in undetectable signal buried under the massive bulk response. To directly overcome these challenges, electronic sum frequency generation (eSFG) can selectively probe interfacial species, defects, and ordering. The sensitivity of this technique arises from the requirement that second order nonlinear signals originate from noncentrosymmetry that is inherent at surfaces and interfaces. Further, the enhancement of eSFG signal due to resonance of material transitions with any one of the three electric fields involved generates a spectrum analogous to linear absorption but originating solely from these regions of interest. Here we present our instrumental implementation of this technique which centers around the use of supercontinuum from a photonic crystal fiber for broadband spectral analysis and a microscopic apparatus to limit, and eventually probe, sample heterogeneity. Finally, our application of this instrument to multiple crystalline materials provides new information to inform future design directions.

Approach

Electronic sum frequency generation (eSFG) is a nonlinear optical technique uniquely sensitive to the electronic structure of noncentrosymmetric samples, including interfaces. In these measurements, two ultrafast laser pulses are incident on a sample of interest. One pulse is often resonant with electronic transitions of the sample in the visible spectral range while the second pulse is set off resonance to upconvert the desired signal. When these two pulses are overlapped in space and time, new light at the sum of the two pulses is generated. Due to the symmetry of the field interactions, no signal in centrosymmetric and isotropic bulk media can be obtained, but where symmetry is broken, such as at interfaces or defects, appreciable signal is observed. While powerful, only a handful of groups have demonstrated this capability,[1-4] but these measurements were made over an ensemble average of interfacial species thereby blurring out information on potential differences in local particle/interfacial chemistry. To limit this

heterogeneity, we have built a widefield eSFG microscope capable of broadband eSFG detection for the study of complex interfaces. These features are achieved using an ultrafast oscillator pumping a photonic crystal fiber (PCF), and the high fields needed to generate appreciable eSFG signal are accomplished through a total internal reflectance excitation geometry using a high NA objective. Current signal collection allows for spectra resolution through a UV objective, appropriate filters, and a spectrograph.

The instrumentation designed for this work is shown in Figure 2.1. The output of a Spectra Physics Tsunami is split into two beams using a waveplate-polarizer combination and a polarizing beam splitter. One beam is routed through a prism compression line directed to a motion controlled stage and then dichroic optic. The second beam is also compressed with a pair of prisms before being focused into a PCF (FemtoWHITE, Newport) to generate a supercontinuum spanning from wavelengths in the visible into the near-IR (Figure 2.2). The supercontinuum is subsequently compressed with a pair of SF10 prims to remove the second order dispersion, although significant third order contributions remain as is evident below. The supercontinuum beam is combined with the 800 nm beam through a dichroic mirror for collinear propagation, and both beams are routed through achromatic polarization and beam expansion optics before entering the microscope. Total internal reflectance was achieved within a high NA (Nikon, 1.49 NA TIRF) microscope objective by focusing and offsetting the input light onto the back focal plane with an achromatic lens.[5] The incident radiation allows for multiple spectroscopic processes and signal collection in both the through and epi-directions depending on the probe of interest. The epi-direction is capable of acquiring one and two-photon fluorescence as well as second harmonic generation (SHG) images. Optical filters, both in the microscope filter cube and in a filter wheel before the camera, are used to distinguish the different signals. The signal in the transmitted direction (above the sample) is collected with a 0.5 NA UV objective (Thorlabs) and is coupled to a spectrograph (Acton and Pixis, Princeton Instruments) with a fiber optic cable and appropriate optical filters for spectrally resolving the radiated eSFG signals. If epi-imaging is desired then a dichroic is used to direct the incident light into the objective while for through direction measurements a silver mirror is utilized.

The light sources used in this setup are essential to producing the eSFG signal. The 50 fs near IR pulse produces the peak powers necessary to induce nonlinear optical events in both the sample and the PCF fiber. The PCF fiber produces the secondary frequencies which are necessary for broadband SFG spectra to be obtained. The supercontinuum produced by the PCF is strongly dependent on the power of the input beam, and as shown in in Figure 2.2, as the input power increases the blue edge of the supercontinuum moves to higher energies. The output of the PCF fiber dictates what spectral regions can be probed, and in the case of the supercontinuum used in our measurements, it was found that a spectral region between 500-750 (eSFG around 310-390 nm) was accessible.

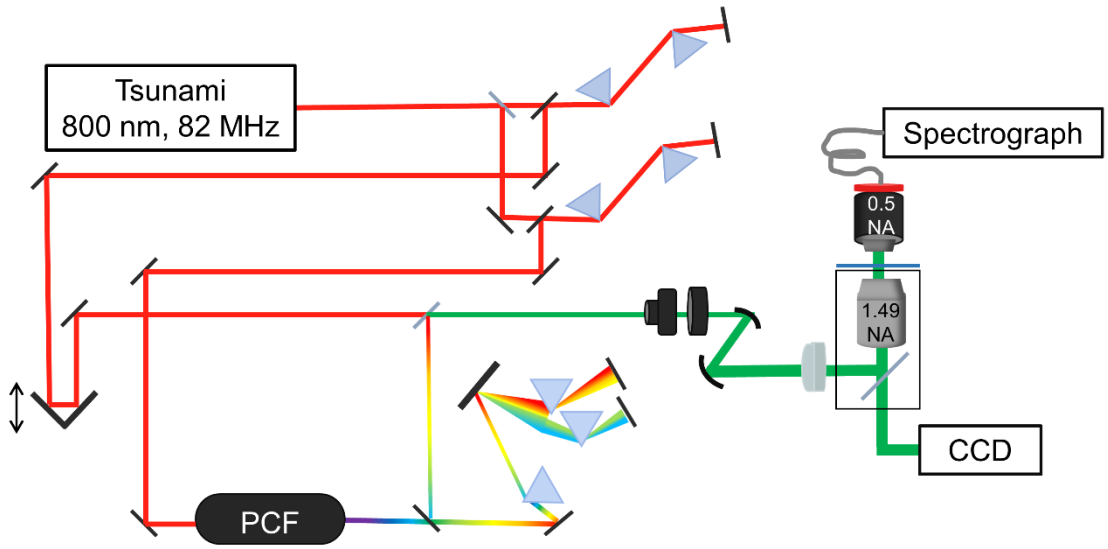

Figure 2.1 Instrument schematic. A beam from the Tsunami is split into to two beams, both of which are compressed, to act as the either the near IR source or produce visible supercontinuum in the PCF. The near IR and supercontinuum are combine together in a collinear geometry before the microscope body. The beams are incident on the sample in a total internal reflectance geometry within the microscope body and signal is collected for either epi-direction imaging on the CCD camera or transmitted to the spectragraph for spectral resolution

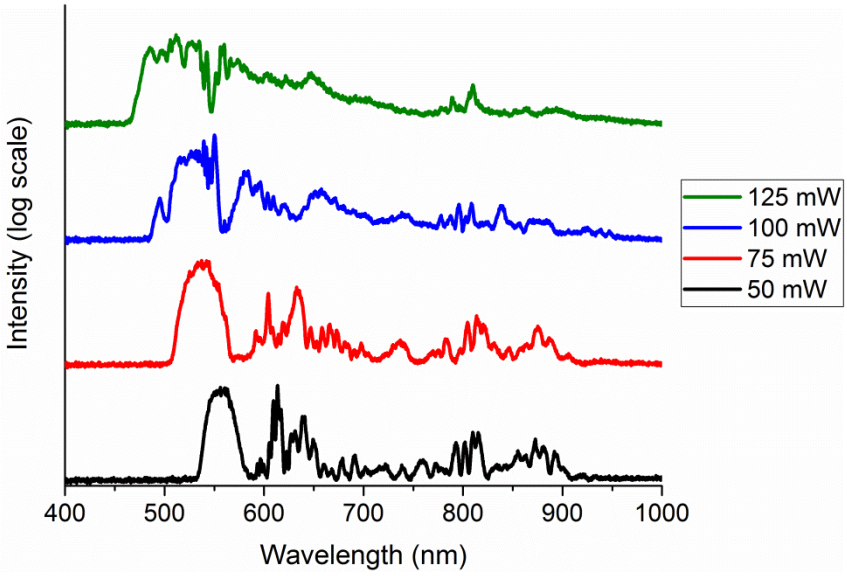

Figure 2.2 PCF fiber output spectrum dependence on input power

The measurements described below aim to provide a detailed look at the capabilities and characterization of this instrument. As such, a model sample, namely potassium dihydrogen phosphate (KDP), was chosen as it is a readily available noncentrosymmetric crystalline material which is known to produce high SHG signals and no fluorescence. SHG is a specific type of SFG in which the two input fields are degenerate but usually have narrow bandwidth. In order to collect the full, broadband eSFG spectra of KDP, the NIR pulses were temporally scanned across the supercontinuum pulses with a retroreflector attached to a motion controlled stage, and the resulting signal at each step was spectrally resolved on the spectrograph (Figure 2.3). Each step has an exposure time of 500 ms and selects a different frequency of the supercontinuum based on the residual uncorrected chirp from the PCF. The scanning creates a data set correlating wavelength, signal intensity, and time delay. The spectra in Figure 2.3 also show that different input polarizations change the intensity of the eSFG signal with p-polarized input producing more signal than s-polarized input. Removing the time delay dependence from the data shown above, results in the eSFG spectra in Figure 2.4. As there are no electronic transitions in this material that are resonant with any of the three electric fields involved in the eSFG signal generation, the broad spectral structure observed between 310-380 nm arises from the structure within our supercontinuum. The black and blue traces in Figure 2.4 further show that the signal from the KDP crystals are sensitive to the polarization of the input light. This behavior arises from both the polarization dependence of the total internal reflection process and the orientation of the KDP crystal. The difference in p-pol and s-pol input can also be seen in Figure 2.5 through SHG imaging. In Figure 2.5, the left image shows the brightfield of the crystalline KDP sample while the center and right images show SHG images collected in the epi-direction with p-pol and s-pol input, respectively. These images also demonstrate the multimodal capabilities of the instrument.

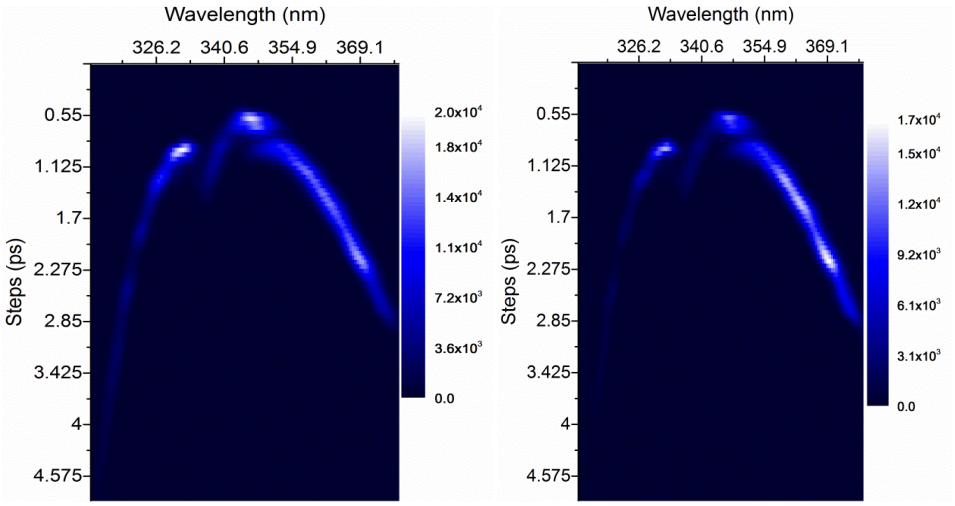

Figure 2.3 eSFG scans for p-polarized (left) and (right) illumination geometries

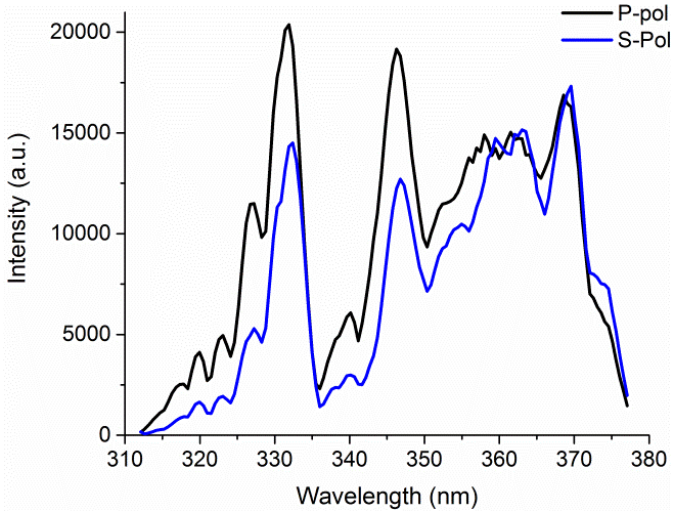

Figure 2.4 eSFG spectra of KDP in total internal reflectance illumination for both p-pol and s-pol input

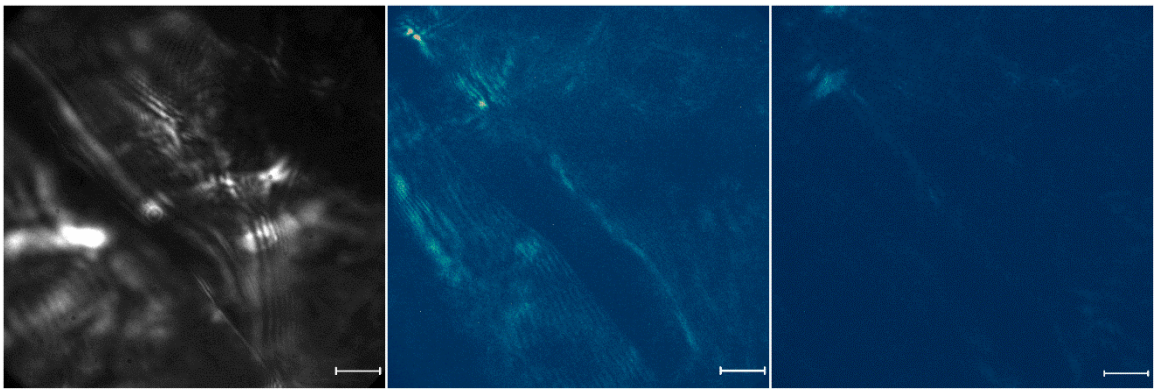

Figure 2.5 Bright field (left) and SHG (p-pol, center and s-pol, right) images of KDP in epi-direction with total internal reflection illumination. All scale bars are 10 μm

Calibration

In order to confirm that the excitation illumination was input at the critical angle necessary for total internal reflectance, fluorescence imaging was also collected in the epi-direction. Total internal reflectance results in an evanescent field which illuminates a wide field with an exponentially decaying amplitude in the z-dimension.[6] The compression of the field in the z-dimension is necessary to achieve sufficient excitation power necessary for nonlinear excitation over such a large area. The wide field nature of the illumination can be seen in both Figures 2.6 and 2.7 where entire images are captured in a single exposure. For these studies a single exposure consists of 0.5 second for brightfield or fluorescence images or 120 seconds for SHG images. The size of the field of illumination was determined by using 1 µm polystyrene beads containing Nile red dye (FluoSpheres, ThermoFisher). The emission from the Nile red microspheres was optically filtered with a 725 short pass (Edmund). The field of illumination was shown to be around 80 µm x 80 µm, as seen in the Figure 2.6 below, with a total image size of 88 µm x 88 µm.

The signal collected was confirmed to be two-photon fluorescence based on the nonlinear relationship of the measured intensity as a function of the input laser power, as shown in Figure 2.6. Similar results were seen when performing SHG imaging in the epi-direction; Figure 2.7 shows the brightfield image of single KDP microcrystal (*left*) and the SHG signal generated from this same crystal from total internal reflection illumination with the 800 nm light (*middle*). The SHG image was optically filtered using a 20 nm bandpass centered at 405 nm (Omega Optics). The corresponding power study is also shown in Figure 2.7 to the right.

The polarization optics prior to the beam expander as described in Figure 2.1 were also calibrated to ensure accurate and known polarization inputs. The polarizer was calibrated by measuring the power throughput on the rotation of the polarizer, which was done to purify the incident polarizations. It was found to have maximum power, as can be seen in Figure 2.8, around 94º and 274º while a minimum was seen around 184º corresponding to horizontal (p-polarized relative to the sample) and vertical (s-polarized relative to the sample) orientations, respectively. After the calibration, the polarizer was set to a position of maximum power and a half waveplate was inserted to rotate the polarization for experiments. In order to calibrate the waveplate, the waveplate was rotated and signal of SHG signal from KDP was monitored on the camera in the epi-direction. As shown in Figure 2.8, the waveplate maximum was observed at ~90º with the minimum at ~45 º. The rotation at 90º was found to be p-polarized and the rotation at 45º was s-polarized. This was confirmed using crossed polarizers in a separate setup. The polarizer and waveplate both show separation of 90º and 45º rotation between maximum and minimum signal, respectively, as expected for each of these optics.

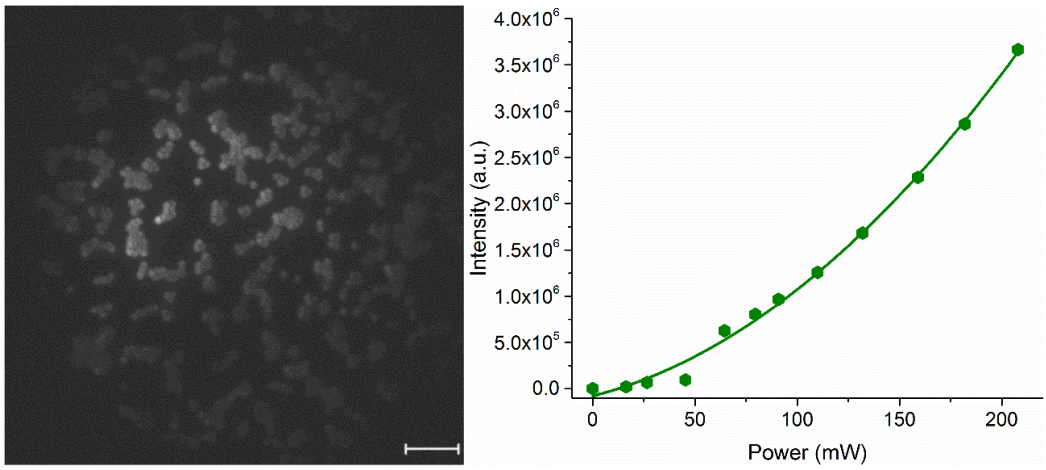

Figure 2.6 Fluorescence image of 1 µm Nile red microspheres in total internal reflectance (left). The scale bar is 10 µm. A power law study was also performed to ensure the fluorescence was two-photon (right)

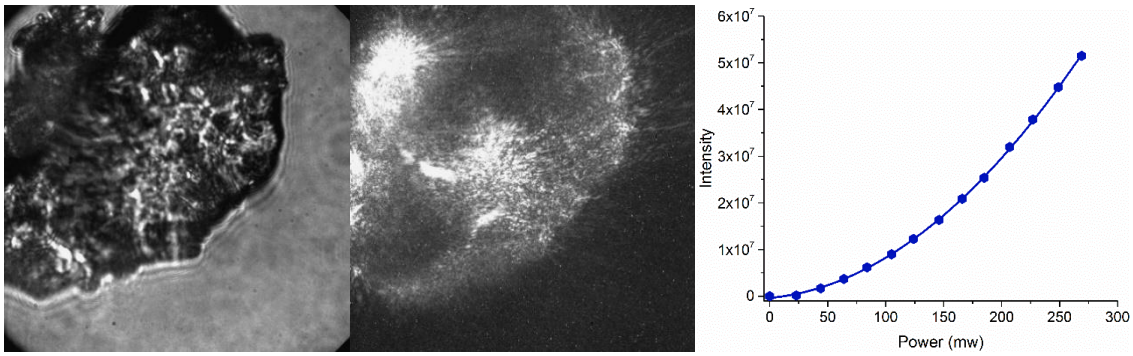

Figure 2.7 Brightfield (left) and SHG (center) image of KDP crystal and the corresponding power law (right) for the sample illuminated at different powers. All scale bars are 10 µm

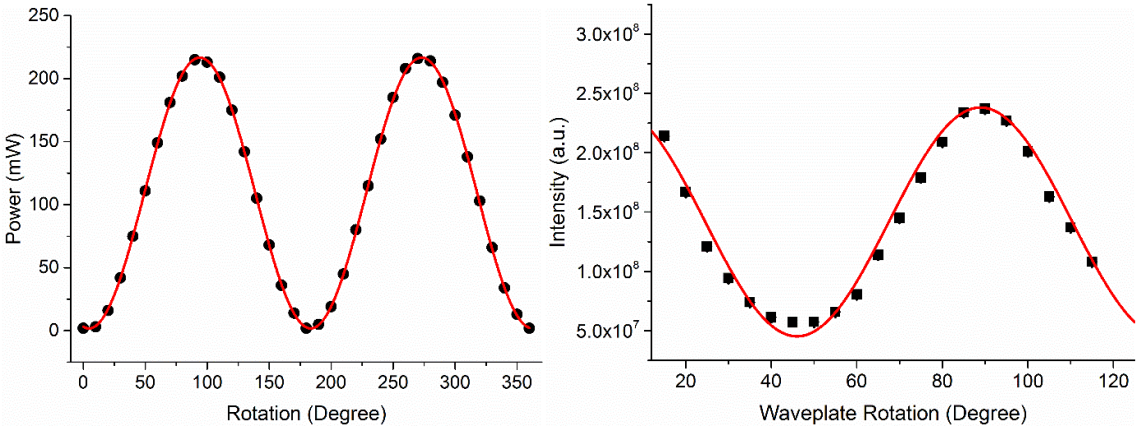

Figure 2.8 Input polarization calibration for polarizer (left) and waveplate (right)

Data Analysis

Custom Python scripts were written to process the raw data from the instrument. The processed data went through four steps: (1) removal of hot pixels, (2) removal of any camera charge from the initial steps of collection, (3) a background subtraction, and (4) a collapse from a 2-D array to a 1-D spectrum. Figure 2.9 illustrates the step wise processing of the collected eSFG signal. Figure 2.9A shows the raw data, which is a spectrum for each time delay measured. This signal notably contains stray light background signal as well as hot pixels/cosmic rays from the CCD camera. The stray light background was removed by averaging a few scans without eSFG signal and subtracting this background spectrum from each eSFG spectrum. Hot pixels/cosmic rays were detected using a script which identified these sharp and instantaneous peaks via thresholding and replaced those pixels with an average of the intensities around it. The processed data in part B of Figure 2.9 and shows the spectra for all the collected time delays with the hot pixels and background removed. In order to condense the 2-D data set into a 1-D spectral array, the maximum intensity of each spectrum corresponding to a wavelength was extracted. The resulting 1-D array is plotted against wavelength as shown in part C of Figure 2.9 and provides a simplified spectrum for interpretation.

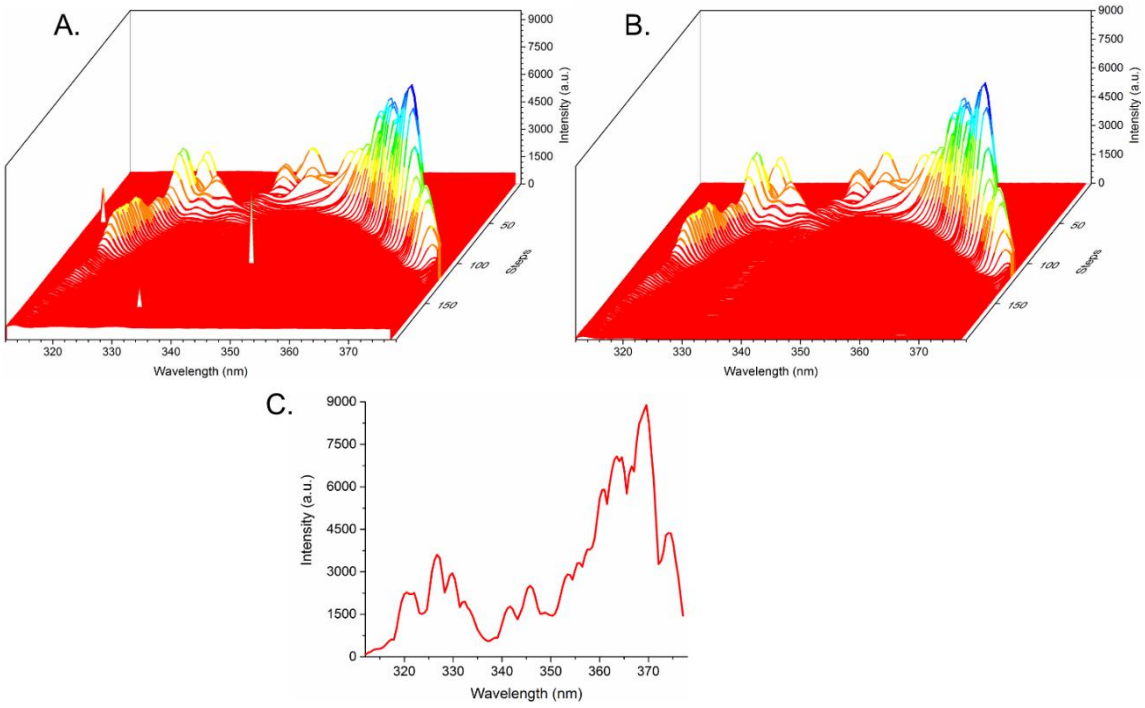

Figure 2.9 Images depicting the data processing for eSFG of KDP. (A) raw data set, (B) data set after the removal of hot pixels and background, (C) condensed 1-D spectrum

Conclusion

The work outlined here demonstrates the design and practical aspects for employing electronic sum frequency generation in a microscope apparatus. We make use of the near IR output from an ultrafast laser oscillator and the visible output from a PCF fiber to produce eSFG signal from single microcrystals in a total internal reflection, collinear excitation geometry. The collection and processing route of the resulting eSFG data from a model KDP sample is shown in detail. The multimodal capabilities of the instrument are also demonstrated with two-photon fluorescence and second harmonic generation images presented. Overall, this microscope is capable of studying the electronic structure of complex material systems and future work is focused on its application to surface alterations.

References

1. Pandey, R.; Moon, A. P.; Bender, J. A.; Roberts, S. T., Extracting the Density of States of Copper Phthalocyanine at the Sio2 Interface with Electronic Sum Frequency Generation. *The Journal of Physical Chemistry Letters* **2016**, *7*, 1060-1066.
2. Sen, P.; Yamaguchi, S.; Tahara, T., Ultrafast Dynamics of Malachite Green at the Air/Water Interface Studied by Femtosecond Time-Resolved Electronic Sum Frequency Generation (Tr-Esfg): An Indicator for Local Viscosity. *Faraday Discussions* **2010**, *145*, 411-428.
3. Yamaguchi, S.; Tahara, T., Development of Electronic Sum Frequency Generation Spectroscopies and Their Application to Liquid Interfaces. *The Journal of Physical Chemistry C* **2015**, *119*, 14815-14828.
4. Moon, A. P.; Pandey, R.; Bender, J. A.; Cotton, D. E.; Renard, B. A.; Roberts, S. T., Using Heterodyne-Detected Electronic Sum Frequency Generation to Probe the Electronic Structure of Buried Interfaces. *The Journal of Physical Chemistry C* **2017**, *121*, 18653-18664.
5. Axelrod, D., Total Internal Reflection Fluorescence Microscopy in Cell Biology. *Traffic* **2001**, *2*, 764-774.
6. Martin, O.; Florian, S., Non-Linear Evanescent-Field Imaging. *Journal of Physics D: Applied Physics* **2005**, *38*, R185.

CHAPTER 3 ♦ ELUCIDATION OF PEROVSKITE FILM MICRO-ORIENTATIONS USING TWO-PHOTON TOTAL INTERAL REFLECTANCE FLUORESCENCE MICROSCOPY

A version of this chapter was originally published by as listed below and is reproduced with permission from American Chemical Society:

Watson, B.R., et. al. "Elucidation of Perovskite Film Micro-Orientations Using Two-Photon Total Internal Reflectance Fluorescence Microscopy." *Journal of Physical Chemistry Letters* **2015**, *6*, 3283-3288

This chapter describes work done by myself. Samples were received from Bin Yang and Kai Xiao. Ying-Zhong Ma, Benjamin Doughty, and Tessa R. Calhoun advised this work

Abstract

The emergence of efficient hybrid organic-inorganic perovskite photovoltaic materials has brought about the rapid development of a variety of preparation and processing techniques designed to maximize their performance. As processing methods continue to emerge, it is important to understand how the optical properties of these materials are affected on a microscopic scale. Here polarization resolved two-photon total internal reflectance microscopy (TIRFM) was used to probe changes in transition dipole moment orientation as a function of thermal annealing time in hybrid organic-inorganic lead iodide based perovskite ($CH_3NH_3PbI_3$) thin films on glass. These results show that as thermal annealing time is increased the distribution of transition moments pointing out-of-plane decreases in favor of forming areas with increased in-plane orientations. It was also shown through the axial sensitivity of TIRFM that the surface topography is manifested in the signal intensity and can be used to survey aspects of morphology in coincidence with the optical properties of these films.

Introduction

Organic-inorganic hybrid perovskites are promising photoactive materials for next generation low-cost photovoltaics. With the highest power conversion efficiency (PCE) of perovskite-based solar cells reported at around 20% and continuous efforts to increase this number as this relatively new system is explored, perovskites are rapidly approaching their silicon counterparts, which hold the lion's share of the solar cell market.[1-4] The enticing performance of perovskite materials originates from the long charge carrier lifetimes and low recombination rates it exhibits, allowing for excellent charge mobility, exceptionally long carrier diffusion length, and reduced recombination losses of charge-carriers.[5-9] Despite the advances in understanding the charge carrier properties within the materials, the effects of preparation on the photophysical properties, as they relate to crystallinity and morphology, especially grains and grain boundaries, are still in need of investigation.[10] Limited knowledge or even methodologies to investigate such questions, has led to a wide range of efforts to increase the PCE in these systems including synthesis of superior precursors, development of new fabrication and processing routes, or post-processing treatments with emphasis on controllable growth of perovskite grains, passivation of defects and grain boundaries, and rational device design. [11-21] In order to tailor perovskite materials for future improvements, it is imperative that the processing of these materials be correlated with their microscopic optical properties.

One area of specific interest is the role of thermal annealing on the perovskite films. It is known that annealing fosters an increase in grain size of the film that contributes to increased efficiency in photovoltaic applications.[21-22] However, there has been minimal exploration of the relationship between the microscopic optical variations and morphological changes despite this being the corner stone of efficient photovoltaics. It is therefore still unclear how the thermal annealing of the film would affect the microscopic optical properties of the crystalline grains and their alignment within the films. Fluorescence imaging is an advantageous tool that can spatially relate physical material properties, such as grain size and morphology, and optical properties, that are important for light harvesting applications of perovskite thin films, as has been shown by Wen, *et. al*. and deQuillettes, *et. al.* who were able to correlate changes in photoluminescence lifetimes with the addition of transport layers and at grain boundaries, respectively.[23-24] Thus far, fluorescence methods have been used to measure lifetimes, the influence of trap states, and to predict the efficiency of these solar cells.[23-29] Fluorescence measurements can also be applied to probe the orientation of electronic transition moments in these materials, which is integral to the absorption and transport of charge carriers in functional devices, but to date not reported. In fact, probing the orientation of domains in complex materials is quickly becoming an area of interest with previous experimental studies being focused on increased efficiency of organic semiconductors, bulk heterojunction photovoltaic systems, as well as computational studies concerning perovskite interfaces.[30-32] To help address these key questions, the role of annealing on optical film properties, such as transition dipole moment orientation, as they relate to known morphological changes, and emission intensity distributions, is at the focus of the present report. By extending fluorescence imaging in a total internal reflection geometry to orientational studies of these samples, perovskite processing methods can be examined in a new light with novel implications.

Results and Discussion

In this report, changes in the orientation of transition moments on the nanometer to micrometer length scales are probed as a function of annealing time for hybrid methylammonium lead tri-iodide (CH3NH3PbI3) perovskite thin films, using polarization resolved two-photon total internal reflection fluorescence microscopy (TIRFM). Here the two photon excitation prepares excited states near 400 nm, that relax through intraband transitions ultimately reaching the band edge, from which the excited states can radiatively recombine.[23, 26-27, 33-34] TIRFM is utilized here to probe both the fluorescence emission intensities and the orientations of contributing electronic dipole moments within the thin films. TIRFM is a surface sensitive technique with its excitation field typically extending only about 100 nm into the sample, thus making it particularly applicable to studying thin film materials.[35] Additionally the technique, as will be shown below, is sensitive to surface topography, due to the differing height of surface features. As illustrated in Figure 3.1, TIRFM is sensitive to the polarization state of the input light and can be used to probe the in- and out-of-plane electronic dipole moment orientation for the sample under study, thus providing a convenient way to map orientation in complex materials.

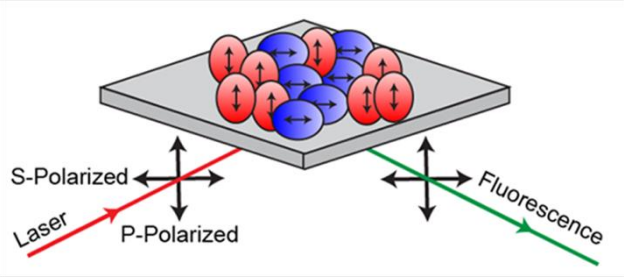

Figure 3.1 Schematic illustrating the preferential absorption of polarized light by species with distinct electronic transition dipole moments. Light parallel (p-polarized) to the scattering plane of the sample will preferentially excite and probe species with dipole moments pointing out of plane (red) while light perpendicular (s-polarized) to the sample scattering plane will preferentially excite and probe those with in-plane dipole moments

Application of two-photon TIRFM has been shown to yield images with increased signal-to-background, improved lateral resolution, and enhanced sensitivity to orientation via multiphoton interactions as compared to single photon methods.[36-38] Additionally, since this method does not rely on scanning of either the sample or the excitation laser beam position, entire images are collected in a single acquisition (<1 second) with diffraction-limited spatial resolution, making this a high throughput method.[39]

Details of the sample preparation and TIRFM microscope are given in the experimental methods section. Briefly, laser pulses from a Ti:Sapphire oscillator centered at 800 nm were used as the two-photon excitation source; fluorescence emission from an nonannealed thin film sample and two other samples subject to one and two hours of annealing, respectively, were spectrally filtered and imaged on a CCD camera in the epi-direction. The fluorescence intensities from different samples were measured to map preferential absorption of linearly polarized light (p- or s-polarized) by different spatial regions in the sample. We found no preferred emission polarization (Supplemental Information Figure A.1), meaning that the fluorescence emission polarization is independent of the input excitation polarization. These results indicate that the emission originates from species other than the initially photoexcited ones, perhaps because of the occurrence of multiple excitation/charge carrier transport steps prior to fluorescence emission such that memory about the initial excitation polarization state has been lost. This is consistent with previous measurements of carrier lifetimes and diffusion lengths.[6-9] Consequently, measurements of the fluorescence signal dependence on the excitation polarization enables the orientation of the absorption transition dipole moments of distinct spatial regions within the film to be mapped.

Representative brightfield and two-photon fluorescence data collected for three different samples with different thermal annealing times are shown in Figure 3.2. For a given sample, the bright-field and fluorescence images were collected at the same spatial position. The fluorescence images show clear heterogeneities in the emission intensities across the thin film plane, which remain visible even in annealed films. In contrast, the bright-field images exhibit significantly less variation across the thin film plane for any given sample. Similar heterogeneity is also seen in SEM images for perovskite thin films prepared in the same manner (Appendix A, Figure A.2). Clearly, the two-photon fluorescence images can provide additional information about the film heterogeneity compared to the bright-field images. The most prominent observation from the two-photon fluorescence images acquired with both p- and s-polarized input light in Figure 3.2 (d,e,f and g,h,i) is that the relative difference between bright and dim spots of fluorescence emission change with annealing time. Bright spots with intense emission relative to the dark regions on the same image and larger feature size are observed in the nonannealed sample (d and g); however, for the two hour annealed sample the bright spots are less prominent and also are smaller in size (f and i). It should be noted that the fluorescence images shown in Figure 3.2 have been scaled to highlight emission features of each sample; thus, absolute intensities of the observed features may be compared for an individual sample but not between different samples due to the use of different scale factors. In addition, the dark areas in the fluorescence images do not necessarily indicate the absence of fluorescence but simply represent weaker signal. In fact, for both the dark and bright areas, our measurements under different excitation intensities showed that the fluorescence emission intensity scaled quadratically with the incident laser intensity, and this expected power law dependence confirms that two-photon emission is the dominant signal seen in these fluorescence images (Appendix A, Figure A.3).

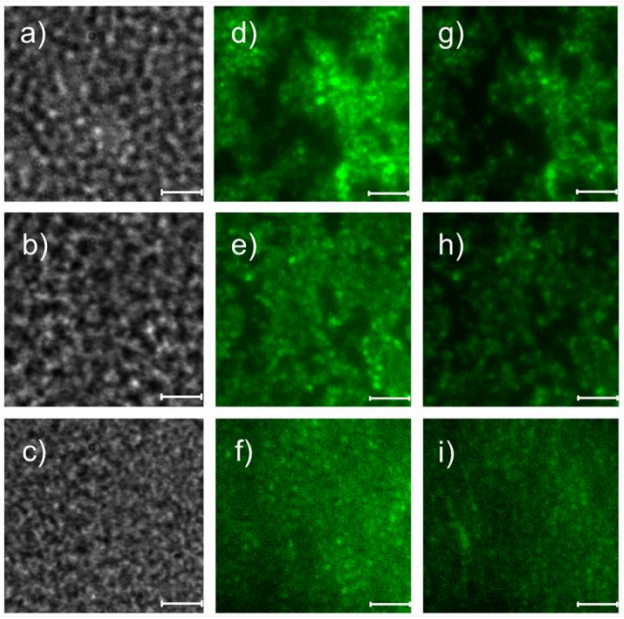

Figure 3.2 Brightfield (a-c) and two-photon fluorescence images (d-f and g-i) acquired for three different samples: nonannealed (top) and annealed for one and two hours at 100 °C (middle and bottom). The fluorescence images shown in d-f and g-i panels were measured with p-polarized and s-polarized excitation light, respectively. All scale bars are 5 μm. The color scale for the p- and s-polarized two-photon fluorescence images were normalized to the same value for each individual sample with the lightest and the darkest color indicating the highest and lowest intensities, respectively. Fluorescence images provide additional information about the film heterogeneity compared to the bright-field images and show changes in the fluorescence emission heterogeneity from the zero hour annealed sample to the two hour sample

In order to better quantify the visible heterogeneity of the fluorescence images, the distribution of highest and lowest fluorescence emission intensities (which will be referred to as sub-populations) were determined and plotted in Figure 3.3. Specifically, these plots were produced by sorting the emission intensities from the fluorescence images in Figure 3.2 into subpopulations of the highest and lowest five percent of the overall normalized intensity. The normalized emission intensity is defined as the pixel intensity divided by the mean intensity of the corresponding image which serves to remove possible inconsistencies associated with comparing absolute fluorescence intensities observed experimentally from different samples. Thus, Figure 3.3 offers a straightforward way to characterize the heterogeneity in the distribution of fluorescence intensity. The larger the spread, represented by the height of the bar, and the greater the differences between the high and low subpopulations corresponds to greater distribution of intensity across the images (*i.e.*, a larger spread of fluorescence intensities) indicating greater heterogeneity. The five data point clusters obtained for each sample represents replicate measurements taken in succession to ensure that the samples were not damaged during the measurements. As can be seen from Figure 3.3, thermal annealing of these perovskite samples results in the overall decrease in difference between the subpopulation averages and the dispersion within each data set, which confirms that the emission intensity becomes more homogeneous as a result of the thermal annealing, in agreement with previous experimental reports.[11-12]

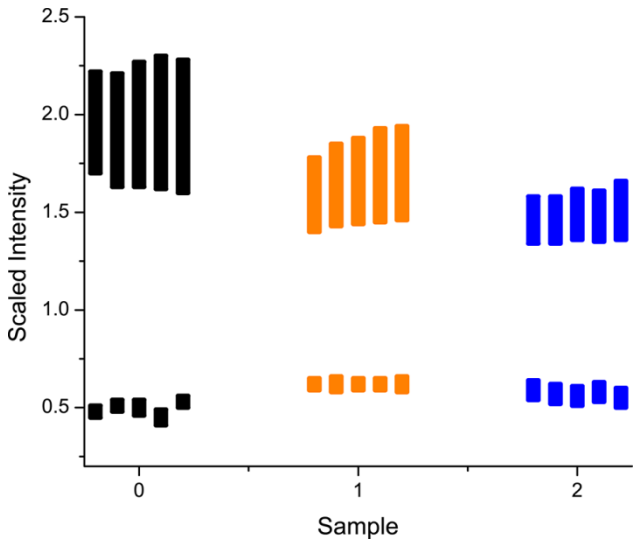

Figure 3.3 Plot of normalized fluorescence intensity subpopulations describing the highest and lowest five percent fluorescence intensities from the p-polarized images in Figure 3.2 (analysis of the s-polarized images displays the same trend, data not shown). The black, orange, and blue sets of points refer to replicate measurements of samples annealed for 0, 1, and 2 hours at 100 °C, respectively. The decreasing difference between the top and bottom intensities show that fluorescence intensity distribution becomes more homogeneous as annealing time increased

A more detailed explanation for the observed changes in heterogeneity of the fluorescence images is two-fold: TIRFM is extremely sensitive to the film height, and the presence of trap states within the crystals could lead to fluorescence quenching. In the first case, the observed variable emission intensities across the film plane could arise from different morphological features, specifically differing sample height, formed during crystal growth and spin coating. It has been demonstrated by Schlipf, *et. al.*, in a comparable film fabrication process, that thin film crystal domains become laterally restricted during crystalline grain formation, and thus the grains are forced to grow in the vertical, out-of-plane, direction. [15] Such growth would produce grains with differing heights at the surface of the film and thus a thin film surface of peaks and valleys. This has been observed in reports using AFM based measurements where the height differences were found to be on the order of tens to hundreds of nanometers.[14] The evanescent excitation field intensity in two-photon TIRFM measurements decays exponentially in the out-of-plane (z-direction), which can be described by $e^{\frac{-2z}{d}}$, where *z* is the interaction depth with the material and *d* is the evanescent field penetration depth.[35-36, 40] As such, the fluorescence intensity would be strongly dependent on the heights of the morphological features.[36] A thin film sample composed of a rough surface with differing feature heights will produce variable fluorescence intensities in the fluorescence images, because absorption within the decaying evanescent field should be remarkably different for distinct regions with different height. As described in the experimental section, the thin film samples used in this work are encased on to a coverslip and therefore the highest features in the film would be closest to the coverslip, which would have strong light absorption and intense fluorescence emission. In contrast, the lower features would be further from the coverslip, leading to weaker absorption and therefore would generate less intense fluorescence signal. As the annealing time is lengthened, the heterogeneity of the fluorescence decreases, as can be seen from both Figure 3.2 and 3.3. This is expected due to increased grain size and a smoothing of the film surface. Such observations demonstrate that TIRFM is inherently sensitive to the topography of the thin film samples in addition to the optical properties. Alternatively, the observed decrease in fluorescence emission could result from the presence of electronic trap states. Such trap states will induce additional non-radiative recombination pathways and consequently lower the efficiency of fluorescence. Previous studies have shown evidence for the presence of trap states in organic-inorganic hybrid lead perovskite materials, correlation between the presence of trap states in the crystals and low fluorescence yield, as well as trap state concentration sensitivity to thermal annealing.[19-20, 24, 33] Based on the considerations above, we believe that the low fluorescence intensity regions seen in the present TIRFM images are likely due both to the presence of trap states and decreased thin film surface height; however, using this singular method the intensity cannot be definitely attributed to either height or trap states.

Beyond the fluorescence intensity images, which provided salient information about the quality of these films, the input excitation polarization used in these measurements can offer key information about the orientation of distinct crystalline domains in the thin films. By analyzing the fluorescence intensity images using

polarization, as described in equation 1, the orientation of contributing electronic transition dipole moments can be obtained.[41]

$$P = \frac{I_{\parallel} - I_{\perp}}{I_{\parallel} + I_{\perp}} \quad (1)$$

Within equation 1, $I_{/\!/}$ and $I_{\perp}$ are the fluorescence intensity measured with parallel (p-polarized) and perpendicular (s-polarized) excitation, respectively, as defined by convention.[40] In this microscope system, preferential absorption by p-polarized light means the absorption dipole is in the vertical, or out-of-plane, direction, while preferential absorption of the s-polarized light occurs in the horizontal direction, as illustrated in Figure 3.1. Total internal reflectance methods thus provide the advantage of resolving both the out-of-plane and in-plane dipole moments, which is unachievable with confocal microscopies, due to the propagation of the light in the axial, or out-of-plane, direction.[40]

The calculated polarization maps derived from equation 1 using the fluorescence intensities from the images in Figure 3.2 are displayed in Figure 3.4. By comparing these polarization maps, one will immediately notice that thermal annealing of the perovskite thin films has profound influences on the orientation of the contributing transition moments within the films. The most strinking finding from the poalrization maps shown in Figure 3.4 is that thermal annealing leads to pronounced in-plane electronic transition dipole moment orientation. This is clearly evident by the increased blue colored regions with negative polarization in the right panel, which arises from dipole moments orientated more parallel to the glass substrate (see Figure 3.1). The red colored regions with positive polarization indicate a preferential absorption of p-polarized light and thus correspond to an out-of-plane pointing dipole moment for the contributing crystalline species. It is not clear if the intermediate polarizations (white and pale red) are larger crystals grains with intermediate orientations or areas of disorder composed of small crystalline domains with a variety of orientations below the optical resolution of our microscope. The change in orientation is more quantitatively shown in Figure 3.5, which plots histograms of the polarization images produced from equation 1 corresponding to each image of Figure 3.4.

The distribution of polarization values shown in Figure 3.5 further reveals the effect of the thermal annealing on altering the orientation of the transition dipole moments. The broadening of the polarization distribution and its peak shift towards more negative polarization values indicates an enhanced contribution from in-plane transitions moments. The potential advantages and disadvantages of preferentially orientated domains warrant further research concerning efficiency in perovskite solar applications. We extend several possibilities including: a relationship between an increased absorption from an unpolarized light source and a variety of transition dipole orientations; improved charge transport with aligned donor and acceptor materials relative to the transition moments; and optimized charge carrier movement with better understanding of the interfaces.[30-32]

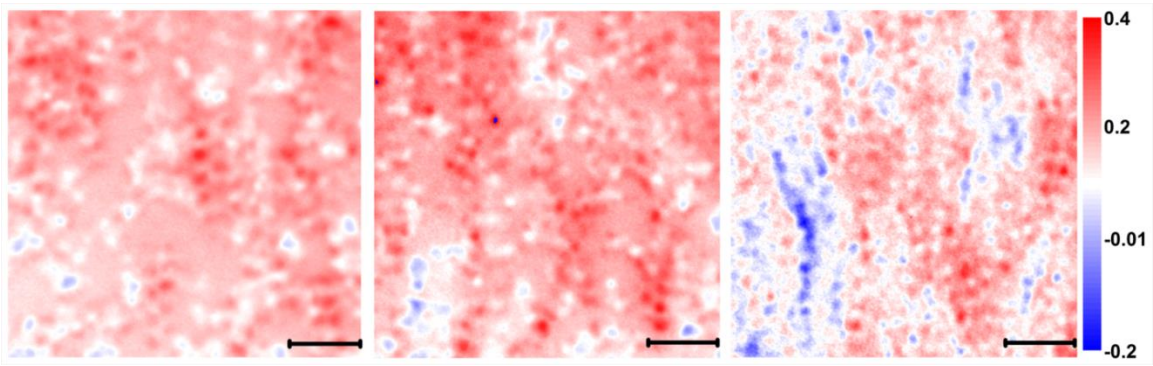

Figure 3.4 Polarization ratio maps of perovskite films annealed for zero, one, and two hours (left to right) are given here. The figures contrast regions of preferred absorption with p-polarized (red) and s-polarized (blue) input light, as schematically shown in Figure 3.1, which were calculated from equation 1 using the fluorescence images from Figure 3.2. Scale bar is 5 μm. Annealing increases the instance of in plane orientation

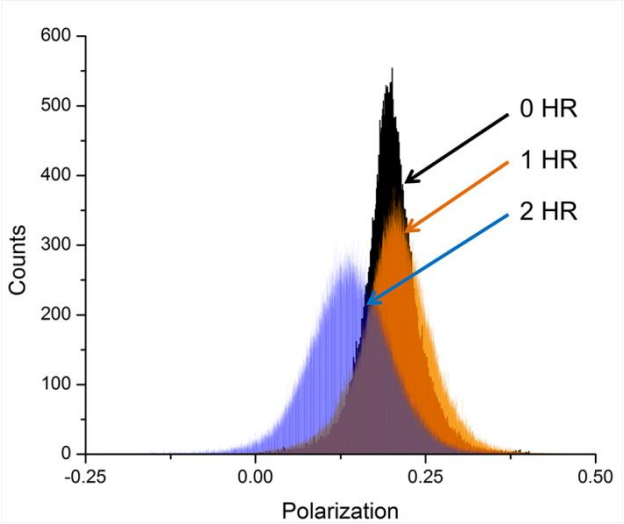

Figure 3.5 Distribution of polarization values, extracted from Figure 3.4, in the nonannealed sample (black) and samples subject to one (orange) and two hours (blue) of annealing at 100 °C. The broadening and shifting of the center of the distribution shows the annealing induced orientation changes of the electronic transition dipole moments

Experimental Methods

A two-step spin-coating technique was used to prepare $CH_3NH_3PbI_3$ perovskite films with typical 1-2 micrometer sized grains and a thickness of ~200 nm.[42] A lead iodide solution (dissolved in dimethylformamide, 300 mg/mL) was spun on to a pre-cleaned glass substrate, followed by an additional spinning of a methylammonium iodide solution (dissolved in isopropanol, 40 mg/mL). The dual spin-coated thin film samples were kept in ambient air for 60 minutes prior to thermal annealing. Thermal annealing was performed on a hotplate at 100 ^oC for 60 and 120 minutes in a nitrogen glovebox. The nonannealed and annealed samples were then attached to microscope coverslips by encasing the sample with a UV epoxy while in the nitrogen filled glovebox. Extensive characterization of the hybrid organic-inorganic perovskite thin films for this preparation method can be found in the work by Yang, *et. al.* and additional SEM images can be found the Supplemental Information.[42] Sample stability was confirmed through separate measurements taken over the course of several hours that showed no signs of degradation. Fluorescence images were collected using a home-built two-photon TIRF microscope. The excitation light source was a femtosecond mode-locked Ti:Sapphire laser (Tsunami, Spectra Physics) producing excitation pulses centered at 800 nm with a pulse width of ~80 fs at a repetition rate of 82 MHz. The microscope consists of a Nikon Eclipse TE300 body outfitted with a beam expander and focusing optics to focus on the back focal plane of the objective, which was a TIRF 1.49 NA, 100x oil-immersion objective (Nikon). Emitted fluorescence light is directed onto a micro-channel plate (MCP) coupled CCD camera (Princeton Instruments) for detection in the epi-direction. The fluorescence emission was doubly filtered with 725 nm shortpass filters (Edmund Optics) and as well as a 750 short pass dichroic mirror (Semrock). The input optical polarization was purified with a Glan-Taylor polarizer and rotated with a half-waveplate prior to the beam expansion. The fluorescence emission signal was polarization resolved using a polarizing beam splitting cube (Edmund Optics) mounted in front of the CCD camera that was set to resolve linearly parallel (p-polarized) output light unless otherwise stated. The setting was chosen based on careful verification that the emission polarization is independent of the excitation polarization (see Appendix A, Figure A.1). Both the two-photon fluorescence and brightfield optical images were analyzed using custom LabVIEW code and plotted in Origin.

Conclusion

In conclusion, our polarization resolved TIRFM measurements on three different thin film $CH_3NH_3PbI_3$ perovskite samples reveal that thermal annealing affects not only the grain size and quality of the thin films, as seen in previous publications[11-12, 16, 21], but also the orientation of the transition moments within the film. These findings raise additional questions about the processing effects on the orientation of transition moments in perovskite thin films and its importance to improving efficiency. TIRFM proves to be another important tool for understanding the structure, not only in regards to orientation, but also the surface topography of perovskite films. Future work will be focused on extending the two-photon fluorescence imaging to composite perovskite films formed with commonly used electron and hole transport layer materials. Efforts in this direction

should enable us to gain deeper insights about the relationships between fluorescence intensity, dipole moment orientation, power conversion efficiency, and thin film fabrication and processing conditions. It is expected that through complete microscopic characterization of these films as they are grown a more detailed picture underlying their incredible performance will emerge.

References

1. Zhou, H.; Chen, Q.; Li, G.; Luo, S.; Song, T.-b.; Duan, H.-S.; Hong, Z.; You, J.; Liu, Y.; Yang, Y. Interface engineering of highly efficient perovskite solar cells. *Science* **2014,** *345*, 542-546.
2. Jeon, N. J.; Noh, J. H.; Yang, W. S.; Kim, Y. C.; Ryu, S.; Seo, J.; Seok, S. I. Compositional engineering of perovskite materials for high-performance solar cells. *Nature* **2015,** *517*, 476-480.
3. National Renewable Energy Laboratory. Best research-cell efficiencies. http://www.nrel.gov/ncpv/images/efficiency_chart.jpg (accessed July 24, 2015).
4. Green, M. A.; Bein, T. Photovoltaics: Perovskite cells charge forward. *Nat. Mater.* **2015,** *14*, 559-561.
5. Chilvery, A. K.; Batra, A. K.; Yang, B.; Xiao, K.; Guggilla, P.; Aggarwal, M. D.; Surabhi, R.; Lal, R. B.; Currie, J. R.; Penn, B. G. Perovskites: transforming photovoltaics, a mini-review. *Journal of Photonics for Energy* **2015,** *5*, 057420-1.
6. Wehrenfenning, C.; Eperon, G. E.; Johnston, M. B.; Snaith, H. J.; Herz, L. M. High charge carrier mobilities and lifetimes in organolead trihalide perovskites. *Adv. Mater.* **2014,** *26*, 1584-1589.
7. Deschler, F.; Price, M.; Pathak, S.; Klintberg, L. E.; Jarausch, D.-D.; Higler, R.; Hüttner, S.; Leijtens, T.; Stranks, S. D.; Snaith, H. J., *et al.* High photoluminescence efficiency and optically pumped lasing in solution-processes mixed halide perovskite semiconductors. *J. Phys. Chem. Lett.* **2014,** *5*, 1421-1426.
8. Stranks, S. D.; Eperon, G. E.; Grancini, G.; Menelaou, C.; Alcocer, M. J. P.; Leijtens, T.; Herz, L. M.; Petrozza, A.; Snaith, H. J. Electron-hole diffusion lengths exceeding 1 micrometer in an organometal trihalide perovskite absorber. *Science* **2013,** *342*, 341-344
9. Xing, G. C.; Mathews, N.; Sun, S. Y.; Lim, S. S.; Lam, Y. M.; Grätzel, M.; Mhaisalkar, S.; Sum, T. C. Long-range balanced electron- and hole-transport lengths in organic-inorganic $CH_3NH_3PbI_3$. *Science* **2013,** *342*, 344-347.
10. Egger, D. A.; Edri, E.; Cahen, D.; Hodes, G. Perovskite Solar Cells: Do We Know What We Do Not Know? *J. Phys. Chem. Lett.* **2015,** *6*, 279-282.
11. Dualeh, A.; Tétreault, N.; Moehl, T.; Gao, P.; Nazeeruddin, M. K.; Grätzel, M. Effect of Annealing Temperature on Film Morphology of Organic–Inorganic Hybrid Pervoskite Solid-State Solar Cells. *Adv. Funct. Mater.* **2014,** *24*, 3250-3258.
12. Eperon, G. E.; Burlakov, V. M.; Docampo, P.; Goriely, A.; Snaith, H. J. Morphological Control for High Performance, Solution-Processed Planar Heterojunction Perovskite Solar Cells. *Adv. Funct. Mater.* **2014,** *24*, 151-157.
13. Zhao, Y.; Zhu, K. Solution Chemistry Engineering toward High-Efficiency Perovskite Solar Cells. *J. Phys. Chem. Lett.* **2014,** *5*, 4175-4186.
14. Zhang, W.; Saliba, M.; Moore, D. T.; Pathak, S. K.; Horantner, M. T.; Stergiopoulos, T.; Stranks, S. D.; Eperon, G. E.; Alexander-Webber, J. A.; Abate, A., *et al.* Ultrasmooth organic-inorganic perovskite thin-film formation and crystallization for efficient planar heterojunction solar cells. *Nat. Comm.* **2015,** *6*, 6142.
15. Schlipf, J. D., P.; Schaffer, C.J.; Korstgens, V.; Biebmann, L.; Hanusch, F.; Giesbrecht, N.; Bernstorff, S.; Bein, T.; Muller-Buschbaum, P. A Closer Look into Two-

Step Perovskite Conversion with X-ray Scattering. *J. Phys. Chem. Lett.* **2015,** *6*, 1265-1269.
16. Moore, D. T.; Sai, H.; Wee Tan, K.; Estroff, L. A.; Wiesner, U. Impact of the organic halide salt on final perovskite composition for photovoltaic applications. *APL Mater.* **2014,** *2*, 081802.
17. Yang, S.; Zheng, Y. C.; Hou, Y.; Chen, X.; Chen, Y.; Wang, Y.; Zhao, H.; Yang, H. G. Formation Mechanism of Freestanding $CH_3NH_3PbI_3$ Functional Crystals: In Situ Transformation vs Dissolution–Crystallization. *Chem. Mater.* **2014,** *26*, 6705-6710.
18. Pathak, S.; Sepe, A.; Sadhanala, A.; Deschler, F.; Haghighirad, A.; Sakai, N.; Goedel, K. C.; Stranks, S. D.; Noel, N.; Price, M., *et al.* Atmospheric Influence upon Crystallization and Electronic Disorder and Its Impact on the Photophysical Properties of Organic–Inorganic Perovskite Solar Cells. *ACS Nano* **2015,** *9*, 2311-2320.
19. Ren, Z.; Ng, A.; Shen, Q.; Gokkaya, H. C.; Wang, J.; Yang, L.; Yiu, W.-K.; Bai, G.; Djurišić, A. B.; Leung, W. W.-f., *et al.* Thermal Assisted Oxygen Annealing for High Efficiency Planar $CH_3NH_3PbI_3$ Perovskite Solar Cells. *Sci. Rep.* **2014,** *4*, 6752.
20. Shao, Y.; Xiao, Z.; Bi, C.; Yuan, Y.; Huang, J. Origin and elimination of photocurrent hysteresis by fullerene passivation in $CH_3NH_3PbI_3$ planar heterojunction solar cells. *Nat. Comm.* **2014,** *5*, 5784.
21. Nie, W.; Tsai, H.; Asadpour, R.; Blancon, J.-C.; Neukirch, A. J.; Gupta, G.; Crochet, J. J.; Chhowalla, M.; Tretiak, S.; Alam, M. A., *et al.* High-efficiency solution-processed perovskite solar cells with millimeter-scale grains. *Science* **2015,** *347*, 522-525.
22. Shi, D.; Adinolfi, V.; Comin, R.; Yuan, M.; Alarousu, E.; Buin, A.; Chen, Y.; Hoogland, S.; Rothenberger, A.; Katsiev, K., *et al.* Low trap-state density and long carrier diffusion in organolead trihalide perovskite single crystals. *Science* **2015,** *347*, 519-522.
23. Wen, X. M.; Sheng, R.; Ho-Baillie, A. W. Y.; Benda, A.; Woo, S.; Ma, Q. S.; Huang, S. J.; Green, M. A. Morphology and Carrier Extraction Study of Organic-Inorganic Metal Halide Perovskite by One- and Two-Photon Fluorescence Microscopy *J. Phys. Chem. Lett.* **2014,** *5*, 3849-3853
24. deQuilettes, D. W.; Vorpahl, S. M.; Stranks, S. D.; Nagaoka, H.; Eperon, G. E.; Ziffer, M. E.; Snaith, H. J.; Ginger, D. S. Impact of microstructure on local carrier lifetime in perovskite solar cells. *Science* **2015**, *348*, 683-686.
25. Miller, O. D.; Yablonovitch, E.; Kurtz, S. R. Strong Internal and External Luminescence as Solar Cells Approach the Shockley-Queisser Limit. *IEEE Photovoltaics* **2012,** *2*, 303-311.
26. Stranks, S. D.; Snaith, H. J. Metal-halide perovskites for photovoltaic and light-emitting devices. *Nat. Nanotechnol.* **2015,** *10*, 391-402.
27. Tress, W.; Marinova, N.; Inganäs, O.; Nazeeruddin, M. K.; Zakeeruddin, S. M.; Graetzel, M. Predicting the Open-Circuit Voltage of $CH_3NH_3PbI_3$ Perovskite Solar Cells Using Electroluminescence and Photovoltaic Quantum Efficiency Spectra: the Role of Radiative and Non-Radiative Recombination. *Adv. Energy Mater.* **2015,** *5*,.
28. Tvingstedt, K.; Malinkiewicz, O.; Baumann, A.; Deibel, C.; Snaith, H. J.; Dyakonov, V.; Bolink, H. J. Radiative efficiency of lead iodide based perovskite solar cells. *Sci. Rep.* **2014,** *4*.

29. Tian, Y.; Merdasa, A.; Peter, M.; Abdellah, M.; Zheng, K.; Ponseca, C. S.; Pullerits, T.; Yartsev, A.; Sundström, V.; Scheblykin, I. G. Giant Photoluminescence Blinking of Perovskite Nanocrystals Reveals Single-Trap Control of Luminescence. *Nano Lett.* **2015,** *15*, 1603-1608.
30. Yin, J.; Cortecchia, D.; Krishna, A.; Chen, S.; Mathews, N.; Grimsdale, A. C.; Soci, C. Interfacial Charge Transfer Anisotropy in Polycrystalline Lead Iodide Perovskite Films. *J. Phys. Chem. Lett.* **2015,** *6*, 1396-1402.
31. Dalal, S. S.; Walters, D. M.; Lyubimov, I.; de Pablo, J. J.; Ediger, M. D. Tunable molecular orientation and elevated thermal stability of vapor-deposited organic semiconductors. *Proc. Natl. Acad. Sci. U.S.A.* **2015,** *112*, 4227-4232.
32. Takacs, C. J.; Collins, S. D.; Love, J. A.; Mikhailovsky, A. A.; Wynands, D.; Bazan, G. C.; Nguyen, T.-Q.; Heeger, A. J. Mapping Orientational Order in a Bulk Heterojunction Solar Cell with Polarization-Dependent Photoconductive Atomic Force Microscopy. *ACS Nano* **2014,** *8*, 8141-8151.
33. Wu, X.; Trinh, M. T.; Niesner, D.; Zhu, H.; Norman, Z.; Owen, J. S.; Yaffe, O.; Kudisch, B. J.; Zhu, X. Y. Trap States in Lead Iodide Perovskites. *J. Am. Chem. Soc.* **2015,** *137*, 2089-2096.
34. Manser, J. S.; Kamat, P. V. Band filling with free charge carriers in organometal halide perovskites. *Nat. Photonics* **2014,** *8*, 737-743.
35. Total Internal Reflection Fluorescence Microscopy. In *Optical Imaging and Microscopy*, Springer Berlin Heidelberg: 2007; Vol. 87, pp 195-236.
36. Martin, O.; Florian, S. Non-linear evanescent-field imaging. *J. Phys. D: Appl. Phys.* **2005,** *38*, R185.
37. Gryczynski, I.; Gryczynski, Z.; Lakowicz, J. R. Two-Photon Excitation by the Evanescent Wave from Total Internal Reflection. *Anal. Biochem.* **1997,** *247*, 69-76.
38. Multiphoton Excitation and Microscopy. In *Principles of Fluorescence Spectroscopy*, Lakowicz, J., Ed. Springer US: 2006; pp 607-621.
39. Masters, B. R.; So, P. T. C. *Handbook of Biomedical Nonlinear Optical Microscopy*. Oxford University Press, USA: 2008.
40. Sund, S. E. S., J.A.; Axelrod, D. Cell Membrane Orientation Visualized by Polarized Total Internal Reflection Fluorescence. *Biophys. J.* **1999,** *77*, 2266-2283.
41. Fluorescence Anisotropy. In *Principles of Fluorescence Spectroscopy*, Lakowicz, J., Ed. Springer US: 2006; pp 353-382.
42. Yang, B.; Dyck, O.; Poplawsky, J.; Keum, J.; Puretzky, A.; Das, S.; Ivanov, I.; Rouleau, C.; Duscher, G.; Geohegan, D., *et al.* Perovskite Solar Cells with Near 100% Internal Quantum Efficiency Based on Large Single Crystalline Grains and Vertical Bulk Heterojunctions. *J. Am. Chem. Soc.* **2015**, DOI: 10.1021/jacs.5b03144..

CHAPTER 4 ♦ ELECTRONIC SUM FREQUENCY TO STUDY SURFACE STATES OF CADMIUN SELENIDE QUANTUM DOTS

A version of this chapter, at time of dissertation submission, was prepared for journal submission.

The work, including sample preparation, data collection, and data analysis, was completed by Brianna R. Watson. Tessa R. Calhoun and Benjamin Doughty advised the and guided many aspects of the work.

Abstract

The widespread success of nanomaterials in many practical devices and applications has been inhibited by the poor understanding and complexity of their surfaces. To address these challenges, a flexible and low cost microspectroscopy platform based on broadband electronic sum frequency generation (eSFG) is described here for studies of nanomaterials and their interfaces. We have applied this technique to cadmium selenide (CdSe) quantum dots (QDs) to demonstrate its capability in characterizing the electronic structure, and specifically surface trap states, of nanomaterial systems. These trap states interfere with efficient light emission and charge transfer processes and are commonly invoked in the literature; however, their energetic locations and characteristics have been the subject of dissent and have eluded direct optical characterization. Our eSFG studies show transitions above the band gap, which correlate to allowed optical transitions of the CdSe core, as well as states below the bandgap that are attributed to surface traps. A wide distribution of these below gap states are observed indicating the coexistence of both shallow and deep trapping sites via a direct spectroscopic measurement. We further show that chemical modification of the surfaces via atmospheric oxidation results in the increase of signal from the surface states. This work demonstrates the feasibility and utility of our broadband eSFG microspectroscopy platform for studies of interfaces with wide applicability to other nanomaterial systems.

Introduction

The control of nanomaterial optical properties via surface modification is essential for continued development of clean energy, efficient lighting, and catalysis applications. Of interest here are semiconducting quantum dots that through a tunable electronic structure have proven to be useful for both light absorbing and light emitting applications.[1-3] The spectral tunability of their absorption and emission of visible light arises from the size of the particles, due to confinement effects and are thus considered *core* electronic properties.[4-13] Other optical properties, specifically including the quantum yield, are heavily influenced by *surface* factors which are greatly exacerbated in these systems due to their high surface-to-volume ratio. In fact, defects at the surfaces of QDs can introduce "surface trap states",[14] which contribute to decreased quantum yields and inefficiencies in charge transfer by providing alternative routes for relaxation or recombination.[15-19] The atomistic origins of trap states are still an active field of research and those that have been elucidated show a large diversity in sources depending on the nanoparticle's composition, crystal structure, surface passivation, and growth conditions.[20] This results in trap state assignments with wildly ranging energies and mechanisms of action. As such, understanding the nature of these states, specifically the

chemical origin and energies of they appear at below the band edge, represents a critical aspect to the continued development of new technologies based on these materials.

Most characterization of trap states relies predominantly on the application of linear optical spectroscopies, most notably photoluminescence (PL). PL, however, is inherently limited as it can only monitor emissive radiative pathways and the resulting changes to those pathways that might emerge on chemical tuning. While this can still yield useful information, we have recently shown that measuring the PL spectra alone does not represent a comprehensive description of the surface defects, the number of these defects, the ligand ordering, or other environmental factors (Chapter 5). Further, in order to properly account for trap states that result in nonemissive states, full quantum yield measurements are required which are not possible for all sample conditions. As such nonlinear spectroscopy, conductance spectroscopy, and scanning tunneling microscopy have been applied to this problem in order to provide more detail into the energetics and dynamics of surface states.[21-23] This suite of tools, however, is still insufficient as there remains ambiguities in the literature regarding the energies of these states with proposed "shallow" and "deep" traps claimed to lie anywhere between 10 meV and 300 meV below the band edge, respectively.[24] Clearly, a new method capable of measuring the surface electronic structure of nanomaterials under a wide variety of different experimental conditions is essential to elucidate the energies of these fundamental states.

To address this challenge, we have integrated broadband electronic sum frequency generation (eSFG) onto a microscopic platform that is capable of directly probing the electronic structure of a small ensemble of CdSe QDs, including their surface states. eSFG is a spectroscopic technique commonly considered to be a surface specific technique that leverages symmetry breaking at interfaces to coherently produce new frequencies of light at the sum of two driving laser frequencies, as shown in Figure 4.1.

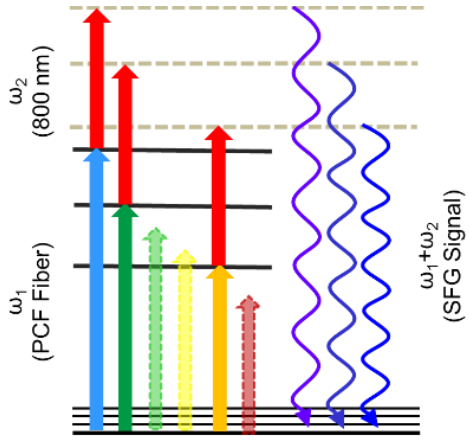

Figure 4.1 Energy level diagram for eSFG

SFG signal is enhanced when one or both of the incident frequencies are on resonance with an optical transition in the material (Figure 4.1). For the case of eSFG, the frequencies are chosen to be on resonance with electronic transitions in the QDs as our goal is to detect the energies of the trap states by monitoring their resonant enhancement. There are limited examples of eSFG being utilized even at model interfaces. Instead, more common SFG techniques are vibrational SFG which can provide information about the ligands but not the QD surface states[25-27], and second harmonic generation (SHG)[28-30] which is restricted in the spectral regions it can probe due to its reliance on degenerate incident frequencies. The previous studies that have used eSFG have measured interfaces of either dyes at water surfaces or materials at substrate interfaces.[31-34] Of the available eSFG studies, none have investigated the electronic structure of QDs. In addition, these previous studies have relied on expensive amplified laser systems with low repetition rates and high peak powers to generate supercontinuum. This broadband light is essential for acquiring a more complete picture of the electronic structure by probing a large spectral region. As an alternative, our instrument requires only an ultrafast oscillator and generates supercontinuum in a photonic crystal fiber to maintain the large spectral window and allow us to probe both bandgap and midgap states. Finally, previous eSFG studies have used more traditional spectroscopy arrangements which results in substantial ensemble averaging in comparison to the microscope apparatus we describe here. Overall, we have advanced the application of eSFG for the study of QDs by developing a new, relatively low-cost femtosecond oscillator-based microscope with the capability of producing broadband spectra. We demonstrate the capabilities of this instrument on multiple sizes of CdSe QDs under two different surface conditions to illustrate the power of directly probing the interfacial species in a microspectroscopic context.

Results and Discussion

The microspectroscopy setup used for these measurements is shown in Figure 4.2. Electronic sum frequency was achieved by combining the 800 nm output of our femtosecond laser oscillator (Spectra-Physics, Tsunami) with supercontinuum spanning 500 – 750 nm that was produced from a FemtoWHITE photonic crystal fiber (PCF, Newport SCG-800). These two light sources were combined in a dichroic mirror, expanded, and focused on the back aperture of a 1.49 NA (Nikon) oil immersion objective in a total internal reflection geometry. Radiated eSFG signal was collected with a 0.5 NA, UV objective above the sample (Thorlabs, LMU-40X-UVB) and directed through a fiber optic attached to an Acton SP-2300i spectrograph equipped with a Pixis CCD camera. SFG signal was filtered from incident light with a bandpass filter. The spectrometer (using a 1200 line/mm grating) was centered at 345 or 355 nm depending on size of the QDs in order to optimize detection of both mid-band gap and bang gap transitions.

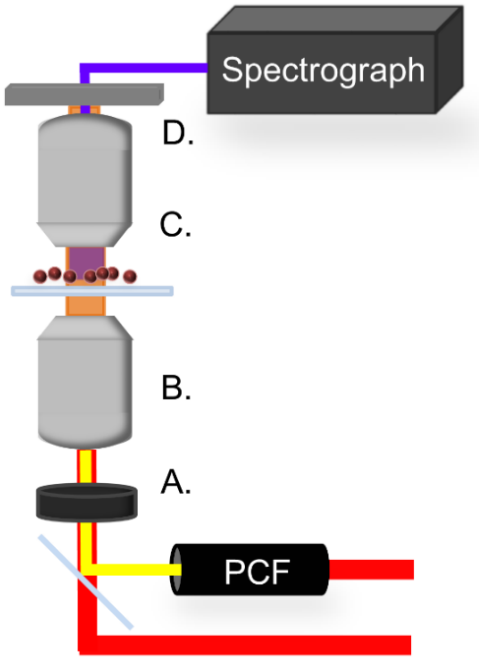

Figure 4.2 Instrument schematic. Excitation light is routed through polarization optics (A) and a 1.49 NA objective (B). The signal is collected with a 0.5 NA objective (C) and optical filter (D) in order to be resolved with a spectrograph

The tunability and broadband spectral range of the fiber output is shown in the supplementary information (Figure B.1). The pulse width of the supercontinuum was found to be about 3.5 ps after rough compression with a pair of SF10 prisms. In order to acquire the eSFG spectra shown below, the delay between the two arms, was controlled with a retroreflector mounted to a linear delay stage and an eSFG spectra for each temporal overlap position between the 800 nm pulse and the different spectral ranges of the supercontinuum was collected. Single spectra were obtained using only a 15 second exposure time, illustrating the speed in which spectra can be collected. From the raw data in Figure B.2, it is clear that third order dispersion is a significant source of the supercontinuum pulse duration. Previous work, however, has demonstrated that PCF supercontinuum can be more optimally compressed[35] which would allow the eSFG spectra to be collected in a single measurement without the need to scan a temporal delay between the incident pulses. In this work, the presented, one-dimensional eSFG spectra are produced from the two-dimensional raw data (Figure B.2) as previously described in Chapter 2.

In order to aid in the assignment of many features observed in the eSFG spectra at or above the bandgap, the UV-Vis spectra of each of the QDs in solution were taken, as shown in Figure 4.3. These spectra reveal optical absorptions which are expected and characteristic to the different sizes of commercial CdSe QDs showing a strong first

exciton and then an almost continuous absorption at lower wavelengths where further peaks can be faintly observed. The first exciton peak appears at the appropriate wavelengths for each of the sizes.[36-37] Drying the sample on a quartz substrate as was done these eSFG measurements, has a negligible effect on the peak positions (Figure B.3); therefore, peak assignments were made with QDs in solution where better signal-to-noise spectra could be obtained. The UV-Vis spectra were fit with Gaussians to extract the peak positions (fits in Figure B.4, B.5, B.6). Based on previous works, these features can be assigned to optical transitions to $1S_{3/2}$, $2S_{3/2}$, $1P_{3/2}$, and $2S_{1/2}$ states depending on the particular particle as indicated in Table 4.1.[38-41] The $1S_{1/2}$ state is considered a weak optical transition and doesn't appear in the UV-Vis; however, it is expected energetically in between the $2S_{3/2}$ and $1P_{3/2}$ states based on photoluminescence excitation spectroscopy of similar sized quantum dots from Norris and Bawendi.[38] It should be noted that for the 4.6 nm size CdSe QD that the $1P_{3/2}$ is also a weak optical transition. The PCF supercontinuum used was broad enough to encompass much of the optical transitions above the bandgap as shown by the highlighted regions in Figure 4.3. For these studies, the largest intensity signals are expected for states that are resonant with the frequency components in the supercontinuum; however, due to the characteristic absorption of these QDs far above the band edge, each spectrum should have included in it a two-photon resonance enhancement.[42-43]

Comparisons of the eSFG spectra to the UV-Vis spectra are shown in Figure 4.4. eSFG peaks appear directly at or closely to the solid lines which mark the fitted peak positions from the linear absorption. Specifically, each QD size has a peak at the first exciton peak, marked by the first (lowest energy) solid line as seen in Figure 4.4 at 595, 622, and 641 nm for 4.6, 5.6, and 6.9 nm QDs, respectively. The next excited state is the $2S_{3/2}$ state as indicated in Table 4.1. While, the peak corresponding to this state is less defined at 617 nm for the 6.9 nm QDs, the 4.6 and 5.6 nm do show peaks around 565 and 596 nm, respectively, in Figure 4.4. The highest energy transition that can be correlated between the eSFG spectra and the UV-Vis arises from the $1P_{3/2}$. The expected peak position of this transition is at the edge of spectrum for the 5.6 nm sample making a definitive assignment difficult for that size. However, this transition is within range for the 6.9 nm sample and shows a strong peak where the $1P_{3/2}$ is expected at 525 nm. It should be noted that shifts in the apparent band positions are due to interference with other bands and a nonresonant background. The quantification of exact peak positions would require fitting to a complex function that for the data set presented here, does not result in a unique solution.

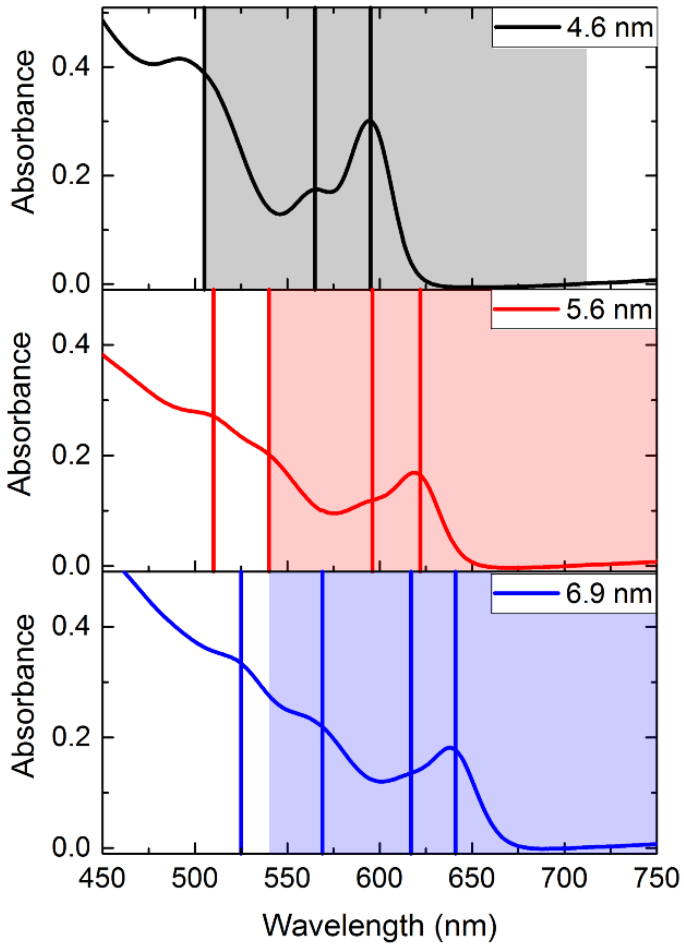

Figure 4.3 UV-Vis of 4.6, 5.6, and 6.9 nm CdSe QDs. Solid lines mark the fitted peak positions indicated in Table 4.1. Highlighted areas indicate regions probed by the broadband eSFG

Table 4.1 Peak assignments from fits to the UV-Vis measurements and expected weak optical transitions from previous work[38] (*italic*)

	QD Size		
Assignment	***4.6 nm***	***5.6 nm***	***6.9 nm***
$1S_{3/2}$-$1S_e$	595	622	641
$2S_{3/2}$-$1S_e$	565	596	617
$1S_{1/2}$-$1S_e$	***537***	***567***	***593***
$1P_{3/2}$-$1P_e$	***525***	540	569
$2S_{1/2}$-$1S_e$	505	510	525

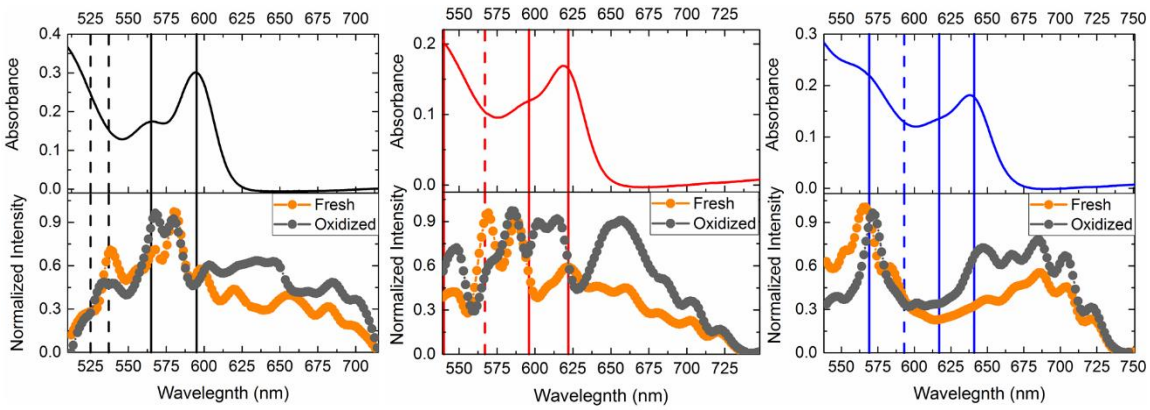

Figure 4.4 eSFG signal from 4.6, 5.6, and 6.9 nm QDs both fresh and oxidized (lower left, center, and right respectively). Thick lines represent peak positions from the fit UV-Vis spectra, dashed lines represent predicted peaks not distinguished in the UV-Vis. The UV-Vis are shown above for clarity.

Experimental Methods

CdSe QDs in toluene with octadecylamine as the ligand were purchased from NN-Labs. Three different sizes of QDs were utilized for the experiments, 4.6, 5.6, and 6.9 nm. The sizes were quoted with an absorbance of 600 nm ± 5, 620 nm ± 10, and 640 nm ± 10, respectively. UV-Vis of solutions of the commercial QDs diluted to appropriate concentrations were taken on a Cary 4E UV-Visible Spectrophotometer, as shown in Figure 4.2. All UV-Vis spectra taken for these commercial QDs support those sizes.[36-37]

Neat aliquots of the QDs solutions, with concentrations of 6.0 µM for 4.6 nm and 5.6 nm diameter QDs or 2.0 µM for the 6.9 nm diameter QDs were drop cast onto quartz coverslips and allowed to dry prior to use. The eSFG spectra of "fresh" samples were collected as soon as the solvent had evaporated. Sample placement was optimized with fluorescence and SHG microscopy before eSFG measurements. The laser source was centered at 800 nm with around 50 fs pulses and a repetition rate of 82 MHz. Average power at the samples was around 25 mW and did not show evidence of photodamage to the sample. All experiments were completed with both input pulses at p-polarization. The QD eSFG spectra are an average of 5 trials that were acquired on the same sample at same illumination positions. The SFG signal from QDs was normalized with SFG signal from potassium dihydrogen phosphate (KDP) to account for changes in the supercontinuum spectral components between experiments. Air exposed samples remained on the microscope for 24 to72 hours and spectra were collected at the same sample position.

Conclusion

As the field of nanoparticle surface science continues to seek new ways to exploit these complex interfaces to tailor and manipulate nanoparticle properties for practical devices

and applications, it is necessary to develop new methodologies to measure and understand how the underlying fundamental optical properties are affected. The novel broadband eSFG microspectroscopy platform presented here is uniquely capable of probing surface electronic structure in model CdSe QDs. The electronic transitions observed in eSFG spectra from three different sizes of CdSe QDs were compared to UV-Vis data, showing that eSFG was not only able to detect linear spectroscopic information, but also produces appreciable signals from optically weak transitions above the bandgap as well as those below the bandgap that are attributed to surface defects. These trap states were chemically modified via air exposure confirming the technique's surface sensitivity to transitions outside of those typically measured in spectroscopy. Electronic sum frequency generation therefore is presented as a technique capable of providing a direct spectroscopic probe of electronic structure at nanomaterial interfaces.

References

1. Kim, J. Y.; Voznyy, O.; Zhitomirsky, D.; Sargent, E. H., 25th Anniversary Article: Colloidal Quantum Dot Materials and Devices: A Quarter-Century of Advances. *Advanced Materials* **2013**, *25*, 4986-5010.
2. Hines, D. A.; Kamat, P. V., Recent Advances in Quantum Dot Surface Chemistry. *ACS Applied Materials & Interfaces* **2014**, *6*, 3041-3057.
3. Frecker, T.; Bailey, D.; Arzeta-Ferrer, X.; McBride, J.; Rosenthal, S. J., Review-Quantum Dots and Their Application in Lighting, Displays, and Biology. *J. Solid State Sci. Technol.* **2016**, *5*, R3019-R3031.
4. Pokrant, S.; Whaley, K. B., Tight-Binding Studies of Surface Effects on Electronic Structure of Cdse Nanocrystals: The Role of Organic Ligands, Surface Reconstruction, and Inorganic Capping Shells. *The European Physical Journal D - Atomic, Molecular, Optical and Plasma Physics* **1999**, *6*, 255-267.
5. Wei, H. H.-Y.; Evans, C. M.; Swartz, B. D.; Neukirch, A. J.; Young, J.; Prezhdo, O. V.; Krauss, T. D., Colloidal Semiconductor Quantum Dots with Tunable Surface Composition. *Nano Letters* **2012**, *12*, 4465-4471.
6. Anderson, N. C.; Hendricks, M. P.; Choi, J. J.; Owen, J. S., Ligand Exchange and the Stoichiometry of Metal Chalcogenide Nanocrystals: Spectroscopic Observation of Facile Metal-Carboxylate Displacement and Binding. *Journal of the American Chemical Society* **2013**, *135*, 18536-18548.
7. La Croix, A. D.; O'Hara, A.; Reid, K. R.; Orfield, N. J.; Pantelides, S. T.; Rosenthal, S. J.; Macdonald, J. E., Design of a Hole Trapping Ligand. *Nano Letters* **2017**, *17*, 909-914.
8. Guyot-Sionnest, P.; Wehrenberg, B.; Yu, D., Intraband Relaxation in Cdse Nanocrystals and the Strong Influence of the Surface Ligands. *The Journal of Chemical Physics* **2005**, *123*, 074709.
9. Lifshitz, E., Evidence in Support of Exciton to Ligand Vibrational Coupling in Colloidal Quantum Dots. *The Journal of Physical Chemistry Letters* **2015**, *6*, 4336-4347.
10. Bullen, C.; Mulvaney, P., The Effects of Chemisorption on the Luminescence of Cdse Quantum Dots. *Langmuir* **2006**, *22*, 3007-3013.
11. Chen, P. E.; Anderson, N. C.; Norman, Z. M.; Owen, J. S., Tight Binding of Carboxylate, Phosphonate, and Carbamate Anions to Stoichiometric Cdse Nanocrystals. *Journal of the American Chemical Society* **2017**, *139*, 3227-3236.
12. Kalyuzhny, G.; Murray, R. W., Ligand Effects on Optical Properties of Cdse Nanocrystals. *The Journal of Physical Chemistry B* **2005**, *109*, 7012-7021.
13. Lee, J. R. I., et al., Ligand-Mediated Modification of the Electronic Structure of Cdse Quantum Dots. *Nano Letters* **2012**, *12*, 2763-2767.
14. Giansante, C.; Infante, I., Surface Traps in Colloidal Quantum Dots: A Combined Experimental and Theoretical Perspective. *The Journal of Physical Chemistry Letters* **2017**, *8*, 5209-5215.
15. Kim, W. D., et al., Role of Surface States in Photocatalysis: Study of Chlorine-Passivated Cdse Nanocrystals for Photocatalytic Hydrogen Generation. *Chemistry of Materials* **2016**, *28*, 962-968.

16. Nagpal, P.; Klimov, V. I., Role of Mid-Gap States in Charge Transport and Photoconductivity in Semiconductor Nanocrystal Films. *Nature Communications* **2011**, *2*, 486.
17. Almeida, A. J.; Sahu, A.; Riedinger, A.; Norris, D. J.; Brandt, M. S.; Stutzmann, M.; Pereira, R. N., Charge Trapping Defects in Cdse Nanocrystal Quantum Dots. *The Journal of Physical Chemistry C* **2016**, *120*, 13763-13770.
18. Gao, Y.; Peng, X., Photogenerated Excitons in Plain Core Cdse Nanocrystals with Unity Radiative Decay in Single Channel: The Effects of Surface and Ligands. *Journal of the American Chemical Society* **2015**, *137*, 4230-4235.
19. Mack, T. G.; Jethi, L.; Krause, M. M.; Kambhampati, P. In *Investigating the Influence of Ligands on the Surface-State Emission of Colloidal Cdse Quantum Dots*, SPIE OPTO, SPIE: 2017; p 8.
20. Houtepen, A. J.; Hens, Z.; Owen, J. S.; Infante, I., On the Origin of Surface Traps in Colloidal Ii–Vi Semiconductor Nanocrystals. *Chemistry of Materials* **2017**, *29*, 752-761.
21. Alperson, B.; Rubinstein, I.; Hodes, G., Identification of Surface States on Individual Cdse Quantum Dots by Room-Temperature Conductance Spectroscopy. *Physical Review B* **2001**, *63*, 081303.
22. Hummon, M. R.; Stollenwerk, A. J.; Narayanamurti, V.; Anikeeva, P. O.; Panzer, M. J.; Wood, V.; Bulović, V., Measuring Charge Trap Occupation and Energy Level in Cdse/Zns Quantum Dots Using a Scanning Tunneling Microscope. *Physical Review B* **2010**, *81*, 115439.
23. Doughty, B.; Ma, Y.-Z.; Shaw, R. W., Probing Interfacial Electronic States in Cdse Quantum Dots Using Second Harmonic Generation Spectroscopy. *The Journal of Physical Chemistry C* **2015**, *119*, 2752-2760.
24. Mooney, J.; Krause, M. M.; Saari, J. I.; Kambhampati, P., Challenge to the Deep-Trap Model of the Surface in Semiconductor Nanocrystals. *Physical Review B* **2013**, *87*, 081201.
25. Bordenyuk, A. N.; Weeraman, C.; Yatawara, A.; Jayathilake, H. D.; Stiopkin, I.; Liu, Y.; Benderskii, A. V., Vibrational Sum Frequency Generation Spectroscopy of Dodecanethiol on Metal Nanoparticles. *The Journal of Physical Chemistry C* **2007**, *111*, 8925-8933.
26. Frederick, M. T.; Achtyl, J. L.; Knowles, K. E.; Weiss, E. A.; Geiger, F. M., Surface-Amplified Ligand Disorder in Cdse Quantum Dots Determined by Electron and Coherent Vibrational Spectroscopies. *Journal of the American Chemical Society* **2011**, *133*, 7476-7481.
27. Weeraman, C.; Yatawara, A. K.; Bordenyuk, A. N.; Benderskii, A. V., Effect of Nanoscale Geometry on Molecular Conformation: Vibrational Sum-Frequency Generation of Alkanethiols on Gold Nanoparticles. *Journal of the American Chemical Society* **2006**, *128*, 14244-14245.
28. Zielinski, M.; Oron, D.; Chauvat, D.; Zyss, J., Second-Harmonic Generation from a Single Core/Shell Quantum Dot. *Small* **2009**, *5*, 2835-2840.

29. Winter, S.; Zielinski, M.; Chauvat, D.; Zyss, J.; Oron, D., The Second Order Nonlinear Susceptibility of Quantum Confined Semiconductors—a Single Dot Study. *The Journal of Physical Chemistry C* **2011**, *115*, 4558-4563.
30. Zielinski, M.; Winter, S.; Kolkowski, R.; Nogues, C.; Oron, D.; Zyss, J.; Chauvat, D., Nanoengineering the Second Order Susceptibility in Semiconductor Quantum Dot Heterostructures. *Opt. Express* **2011**, *19*, 6657-6670.
31. Yamaguchi, S.; Tahara, T., Development of Electronic Sum Frequency Generation Spectroscopies and Their Application to Liquid Interfaces. *The Journal of Physical Chemistry C* **2015**, *119*, 14815-14828.
32. Pandey, R.; Moon, A. P.; Bender, J. A.; Roberts, S. T., Extracting the Density of States of Copper Phthalocyanine at the Sio2 Interface with Electronic Sum Frequency Generation. *The Journal of Physical Chemistry Letters* **2016**, *7*, 1060-1066.
33. Sen, P.; Yamaguchi, S.; Tahara, T., Ultrafast Dynamics of Malachite Green at the Air/Water Interface Studied by Femtosecond Time-Resolved Electronic Sum Frequency Generation (Tr-Esfg): An Indicator for Local Viscosity. *Faraday Discussions* **2010**, *145*, 411-428.
34. Moon, A. P.; Pandey, R.; Bender, J. A.; Cotton, D. E.; Renard, B. A.; Roberts, S. T., Using Heterodyne-Detected Electronic Sum Frequency Generation to Probe the Electronic Structure of Buried Interfaces. *The Journal of Physical Chemistry C* **2017**, *121*, 18653-18664.
35. Higgins, K.; Calhoun, T. R., Compressed Supercontinuum Probe for Transient Absorption Microscopy. *Opt. Lett.* **2018**, *43*, 1750-1753.
36. Yu, W. W.; Qu, L.; Guo, W.; Peng, X., Experimental Determination of the Extinction Coefficient of Cdte, Cdse, and Cds Nanocrystals. *Chemistry of Materials* **2003**, *15*, 2854-2860.
37. Jasieniak, J.; Smith, L.; van Embden, J.; Mulvaney, P.; Califano, M., Re-Examination of the Size-Dependent Absorption Properties of Cdse Quantum Dots. *The Journal of Physical Chemistry C* **2009**, *113*, 19468-19474.
38. Norris, D. J.; Bawendi, M. G., Measurement and Assignment of the Size-Dependent Optical Spectrum in Cdse Quantum Dots. *Physical Review B* **1996**, *53*, 16338-16346.
39. Ekimov, A. I.; Hache, F.; Schanne-Klein, M. C.; Ricard, D.; Flytzanis, C.; Kudryavtsev, I. A.; Yazeva, T. V.; Rodina, A. V.; Efros, A. L., Absorption and Intensity-Dependent Photoluminescence Measurements on Cdse Quantum Dots: Assignment of the First Electronic Transitions. *J. Opt. Soc. Am. B* **1993**, *10*, 100-107.
40. Wolf, M.; Berezovsky, J., Homogeneous and Inhomogeneous Sources of Optical Transition Broadening in Room Temperature Cdse/Zns Nanocrystal Quantum Dots. *Applied Physics Letters* **2014**, *105*, 143105.
41. and, A. L. E.; Rosen, M., The Electronic Structure of Semiconductor Nanocrystals. *Annual Review of Materials Science* **2000**, *30*, 475-521.
42. Moad, A. J.; Simpson, G. J., A Unified Treatment of Selection Rules and Symmetry Relations for Sum-Frequency and Second Harmonic Spectroscopies. *The Journal of Physical Chemistry B* **2004**, *108*, 3548-3562.

43. Lin, C.-K.; Lei, J.; Lin, Y.-D.; Lin, S. H., Electronic Sum-Frequency Generation (Esfg) Spectroscopy: Theoretical Formulation of Resonances with Symmetry-Allowed and Symmetry-Forbidden Electronic Excited States. *Molecular Physics* **2017**, *115*, 1803-1812.
44. Peng, P.; Milliron, D. J.; Hughes, S. M.; Johnson, J. C.; Alivisatos, A. P.; Saykally, R. J., Femtosecond Spectroscopy of Carrier Relaxation Dynamics in Type Ii Cdse/Cdte Tetrapod Heteronanostructures. *Nano Letters* **2005**, *5*, 1809-1813.
45. Cordero, S. R.; Carson, P. J.; Estabrook, R. A.; Strouse, G. F.; Buratto, S. K., Photo-Activated Luminescence of Cdse Quantum Dot Monolayers. *The Journal of Physical Chemistry B* **2000**, *104*, 12137-12142.
46. Hines, D. A.; Becker, M. A.; Kamat, P. V., Photoinduced Surface Oxidation and Its Effect on the Exciton Dynamics of Cdse Quantum Dots. *The Journal of Physical Chemistry C* **2012**, *116*, 13452-13457.
47. Sykora, M.; Koposov, A. Y.; McGuire, J. A.; Schulze, R. K.; Tretiak, O.; Pietryga, J. M.; Klimov, V. I., Effect of Air Exposure on Surface Properties, Electronic Structure, and Carrier Relaxation in Pbse Nanocrystals. *ACS Nano* **2010**, *4*, 2021-2034.

CHAPTER 5 ♦ PROBING LIGAND REMOVAL AND ORDERING AT CDSE QUANTUM DOT SURFACES USING VIBRATIONAL SUM FREQUENCY GENERATION SPECTROSCOPY

A version of this chapter was submitted for publication.

This chapter describes work done by Brianna R. Watson. Ying-Zhong Ma assisted in collection of photoluminescence spectra and advised the work. John F. Cahill performed mass spectrometry measurements. Benjamin Doughty, and Tessa R. Calhoun advised the experimental design, analysis, and manuscript preparation.

Abstract

The development and design of nanoparticle technologies continues to highlight the necessity to understand and control the surfaces of nanomaterials. Despite the importance of these surfaces, challenges arise for techniques to characterize their structure and local environments directly given the relatively low number of species present. Of particular interest here are surface bound ligands that can be removed, exchanged and otherwise modified to alter an assortment of properties. Vibrational sum frequency spectroscopy (vSFG) provides a direct avenue to understand and correlate how ligand ordering and coverage impact the electronic structure and dynamics of the nanocrystal. By measuring the ratio of methylene to methyl stretches in the alkyl chain of octadecylamine (ODA) ligands, we characterized the removal and ordering of the ligands from the CdSe quantum dots. By relating this information to photoluminescence (PL) measurements made in parallel, we show that the decrease in PL intensity is impacted more by the introduction of surface defects than the adsorption of quenching nonsolvent molecules. Vibrational SFG was more sensitive to subtle changes in ligand disorder over multiple precipitation-resuspension washes when compared to PL highlighting the surface utility of directly probing the ligands at the surface of quantum dots.

Introduction

The improvement of nano-synthetic methods has advanced the size consistency, shape, and optical performance of nanoparticle materials.[1] A large portion of the literature concerning the optimization of quantum dots (QDs) is dedicated to tailoring the interfacial layer on their exterior surfaces.[2] The choice of surface modification is integral to their performance because it dictates the solubility, electronic properties, and even the crystal structure of nanomaterials.[3-5] As examples, surface modification impacts a wide range of areas including: compatibility and toxicity in biological imaging and biosensing, optimization of the quantum dots surfaces for improved quantum efficiency, whitelight emission, and light harvesting applications.[6-10]

Synthetic routes for the chemical modification of CdSe quantum dot surfaces are well documented and typically consist of either coating the core semiconducting material with a shell of a different semiconductor material or introducing ligands that bind to the atoms on the exterior surface.[1-2] The ligands can be characterized according to their interactions with the atoms at the surface of the nanoparticle and are described as L-type, X-type, or Z-type.[3, 11-12] The presence and type of ligands on the surface can be varied either during synthesis or after via ligand exchange methods.[13-16] In recent years, there has been increased attention into how common synthetic routes of nanocrystalline

materials can alter their surface characteristics.[17-19] Along these lines, precipitation and resuspension is often a primary step in isolating and separating the quantum dots from the starting materials[20-23], but it has been reported that the type of ligand and the nonsolvent used in the precipitation affects the removal and modification to the surface.[17-19] These works show that L-type ligands were removed in the initial purification steps whereas the removal of X-type ligands were impacted by the choice of nonsolvent, specifically if the solvent was polar protic or aprotic. As L, X, and Z-type ligands exhibit different binding strengths to the nanoparticles, it is important to characterize how standard synthetic steps affect them individually.

Information about the effects of ligand modification on the particle is typically extracted from changes in photoluminescence (PL).[24-26] The removal of ligands from the quantum dots surface results in the formation of dangling bonds and corresponding surface trap states and thus nonradiative pathways for excited state relaxation, thereby reducing the PL intensity. While PL is often used as a metric of surface quality, it only reports on the surface indirectly as the signal originates from the particle itself. Much more information regarding disorder and heterogeneity in speciation is available by probing the surface species themselves.[27] As such, there has been efforts to directly probe surface moieties at nanoparticle surfaces using methods such as: scintillation counting,[28] NMR,[18] FT-IR,[29] Raman,[30] electronic absorption spectroscopy,[31] X-ray spectroscopies,[27] and thermogravimetric analysis.[32] In order to explore surface ligand population and accompanying changes in ligand ordering on chemically modified QDs, we apply vibrational sum frequency generation (vSFG) to probe vibrational transitions of the ligands. It has been well established that the methyl- and methylene stretches are SFG active and are an indication of the disorder of alkyl- chains at the surfaces of materials,[33-38] thus providing a direct avenue to evaluate the structural changes that accompany ligand exchange and removal. By correlating vSFG measurements of the ligand ordering with methods capable of probing changes to the core material properties, such as PL, we are able to gain a better understanding about the impact of ligand exchange/removal on interfacial chemistry, structure, and electronic properties of well-defined nanocrystals.

Experimental Methods

Sample Preparation

CdSe QDs of three different diameter sizes (4.6, 5.6, and 6.9 nm) suspended in hexanes were purchased from NN-labs. These nanoparticles are covered by octadecylamine with a coverage of around 20%, have a Cd:Se ratio of 1:1, and a size distribution within 10% of the quoted size based on the expected absorption ranges of (600 ± 10, 620 ± 10, and 640 ± 10 nm, respectively).[39] These surface ligands mediate solubility as well as optical and electronic properties, as described above and in the literature.[24, 40] Ligands were removed from the quantum dots through a common precipitation and resuspension process.[20, 22, 41-42] A 1:1 ratio of a polar nonsolvent (either acetone or methanol as aprotic and protic solvent, respectively) was added to a 500 µL aliquot of the commercial quantum dots solution. The addition of the nonsolvent caused a

precipitation of the QDs and the solutions were centrifuged at 6000 rpm for 10 min to facilitate full separation. The supernatant was removed and the QDs were resuspended in fresh hexane to return the QDs to the original volume. A single iteration of this process was considered one wash and samples were washed one, two, three, or four times. This produced a sample set for each size and nonsolvent, including an unwashed stock solution and the four washed solutions, and resulted in a total of nine QD samples per size.

These samples were diluted by a factor of nine in hexane to a final volume of 4000 µL for characterization with vSFG, UV-Vis absorption, and photoluminescence. The final concentrations of these dilute solutions varied due to loss of QDs through the washing process but were in the range of $10^{13} – 10^{15}$ particles/mL as calculated from the UV-Vis spectra (see Figures 5.1, C.1, and Table C.1) and are consistent with previous studies. [34-35]

Sample Characterization

UV-Vis spectra were collected on a Cary 4E UV-Visible Spectrophotometer with a 1 cm path length and was used to measure QD concentration as well as changes to the QDs core size. The first exciton peak amplitude was used to determine the concentration while the peak position was used to detect any changes to the core size.[17, 19, 39, 43-44]

PL measurements were taken on the dilute samples to measure the effects of ligand removal on the QD PL intensity and were performed on a Fluorolog (Jobin Yvon). All samples were excited at 400 nm with a 2 nm excitation slit width. Emission spectra were corrected for the changes in solution concentration as determined from UV-Vis measurements. The resulting PL intensity at a given wavelength was then divided by the corresponding intensity of the unwashed sample to determine a normalized change in PL (Tables C.2, C.3, C.4).

Both NMR and mass spectrometry were performed to ensure ligands removal. Proton NMR were taken of the unwashed and washed CdSe QD solutions and performed on a Bruker Avance 400 MHz. Mass spectrometry was performed on the supernatant. Further details about these experiments can be found in Appendix C.

Sum Frequency Generation Spectroscopy

The vSFG technique uses two pulses of light, one in the near infrared (NIR) and the other in the infrared (IR). The broadband IR pulse induces a polarization in the sample that is upconverted by a temporally overlapped narrowband near infrared pulse to create a coherent second order polarization that oscillates and therefore radiates at the sum of the two incident laser frequencies. When the IR spectral components are resonant with vibrational transitions in the sample, there is an enhancement of signal thus mapping the vibrational spectrum of the sample. The details of the optical setup and signal processing have been explained previously elsewhere.[45-48] Briefly, the output from a 1kHz femtosecond regenerative amplifier (Spectra Physics Spitfire Pro) centered at 800

nm was split into two paths. A portion of this light was sent to a 4*f*-pulse shaper to produce ~1 ps pulses for use as the up-conversion light. A majority of the amplifier output was routed to an optical parametric amplifier and difference frequency mixer (TOPAS-Prime) to produce the broadband IR pulses. The IR pulses were centered around 3450 nm (~2900 cm^{-1}) with a spectral bandwidth of about 300 cm^{-1} to probe the CH stretching region. The NIR and IR beams were brought together in typical reflectance geometry with the beams focused on the sample at a 48˚ and 66˚ angle relative to the surface normal, respectively. All spectra were taken with the SSP polarization combination, where the SFG radiation was measured at S-polarized, the input NIR at S-polarized, and the input IR at P-polarized, in accordance with previous studies.[33-34, 49-50] Raw SFG spectra were background subtracted with a registered region of interest and scaled by the signal obtained from a gold film to correct for wavelength dependence in the broadband IR spectrum. NIR and IR powers incident on the sample were on the order of 15 and 4 mW, respectively. The dilute samples of CdSe QDs were drop cast onto quartz substrates for the SFG measurements. The quartz substrates were cleaned before each trial with solutions of nanopore water and sodium hydroxide followed by a rinsing with nanopore water and hexane. As expected, the cleaned substrates showed no SFG response in agreement with previous work. A single spectrum had an exposure of 5 minutes and with 3 spectra per trial. Spectra were taken for three to four spatial positions on the quartz and averaged to ensure measurements are a representation of the whole sample and that potential spatial heterogeneities (*e.g.* coffee rings) do not impact the results. No photodegradation was observed over any of the trials or any of the different spatial positions.

Data Analysis

Analysis of the SFG spectra were performed using custom LabVIEW and Python scripts. The analysis consists of fitting each of the SFG spectra with four Lorentzians and a nonresonant contribution and is detailed in the SI.[40-41, 43] From the fitting analysis, the peak amplitude, width, position, and nonresonant contribution were determined and tabulated (Tables C.1, C.2, and C.3).

Results and Discussion

Initial optical absorption measurements were taken to ensure that the only modification to the quantum dots were due to the surface ligand removal and not from etching the metal chalcogenide surface. Figure 5.1 shows the UV-Vis spectra for 4.6 nm particle size and the different wash conditions; UV-Vis spectra for the other size samples can be found in Figure C.1. The peak position of the first exciton band around 600 nm does not change substantially between washes. This matches the expectation that removal of L-type ligands does not induce surface etching.[18] It should be noted, however, that changes in the amplitude of the peaks indicates a decrease in quantum dot concentration due simply to loss during the washing steps. Changes in the baseline indicate aggregation after multiple washing steps (*i.e.* more scattering from larger particles), and are consistent with the loss of ligands that stabilize the particles in solution.

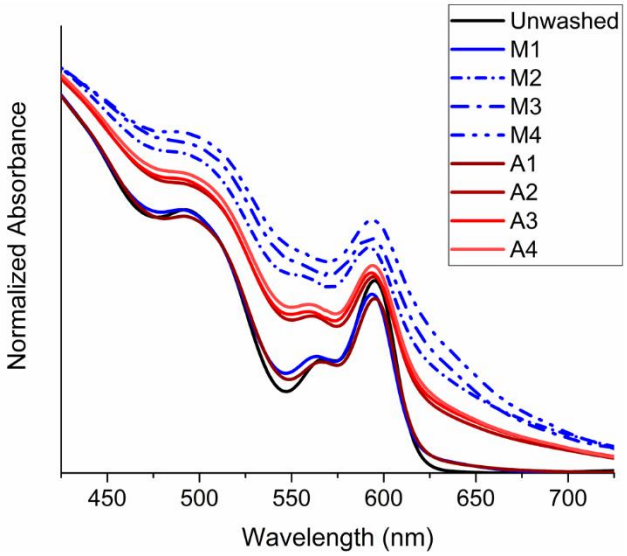

Figure 5.1 UV-Vis spectra for 4.6 nm CdSe series. Spectra are labeled by the nonsolvent ("A" for acetone and "M" for methanol) and the number of washes performed on the sample. Spectra have been normalized around 400 nm

Ligands on the surface, as stated previously, are important regulators of optical properties. Ligands prevent the formation of surface trap states by interacting with unbound electrons and/or holes at the surface. The removal of ligands opens up nonradiative pathways, and, in response, a decrease in PL. This phenomenon has been described extensively in literature.[4, 13, 24-25, 40, 51-55] In order to assess these changes over our washing cycles, PL measurements were made using the same samples employed in the linear absorption and the vSFG measurements described below. Emission peaks were centered at 610, 630, or 650 nm depending on the size of the particle. For all the samples studied, a sharp drop in PL after the first washing was observed, as shown in Figure 5.2, where the PL intensity for each sample was adjusted according to its concentration and then divided by the PL of the unwashed sample (as shown in Table C.2, C.3, and C.4). The complete set of acquired PL data can be found in Appendix C. Based on these PL measurements alone, one cannot differentiate between the observed decrease in PL being due to an increase in the number of surface trap states, adsorption of nonsolvent species to the surface that act as quenching agents, or aggregation effects.[4, 17] In order to assess the role of aggregation, the PL measurements can be compared to the UV-Vis. As the increase in the baseline of the UV-Vis data can be attributed to aggregation of the samples. The increase of the baseline is observed to be more gradual than the changes in the PL and the band positions do not change as a function of wash, which would indicate that aggregation is not largest source of PL loss from washing. To differentiate the impact of ligand removal and nonsolvent adsorption, we turn to the vSFG data presented below. The reliance on additional techniques demonstrates that while PL is a facile method for quantifying optical properties of these materials, it does not have enough chemical fidelity to provide a comprehensive picture of the surface interactions and alterations.

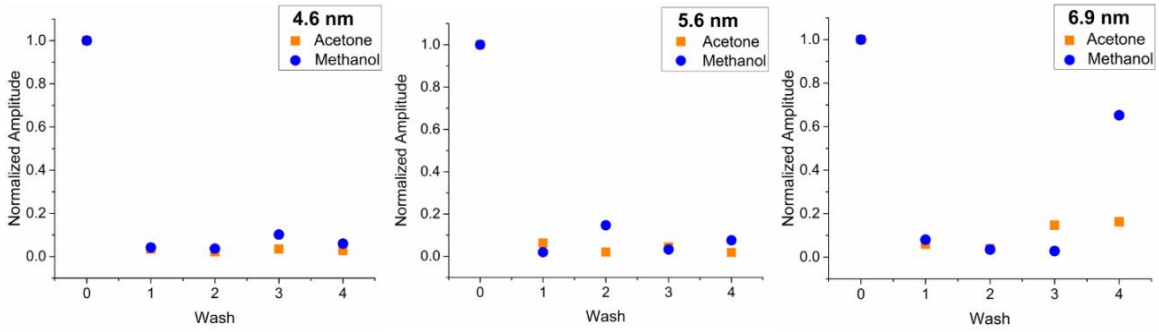

Figure 5.2 Normalized emission intensity of 4.6, 5.6, and 6.9 nm CdSe quantum dots after washing

In addition to PL measurements, mass spectrometry and NMR were completed to confirm ligand removal. The NMR studies were performed on unwashed and washed samples (as can be seen in Figures C.7-18). The NMRs show peaks in the 3.0 to 0.0 ppm region which can be attributed to the octadecylamine ligands on the surface, as well as the hexane solvent. The NMRs show these peaks as atop a broader peak for the unwashed and sample having gone through one wash. This broad peak is attributed to ligand attachment at the surface.[40, 56] Therefore the NMRs confirm removal of the ligands and shows a majority of the ligands are removed by the second wash. This is in agreement with the PL measurements that shows largest changes to ligand coverage after the first wash, but provides evidence for the persistence of ligands on the surface after at least two wash steps. The mass spectrometry data confirms ODA in the supernatant collected from each wash with acetone, as seen in Figure C.15. Again, this is in agreement with the PL, NMR and as will be shown below, SFG measurements. These analytical measurements demonstrate that the ligands are originally attached to the surface, and washing does in fact remove them.

The packing of ligands on the surface of a nanoparticle will primarily be based on the length, number density, and properties of the ligand and size of the nanoparticle. The relationship between nanoparticle size and ligand disorder was shown previously for gold nanoparticles which showed an *increase* in order as the diameter increased.[34-35] In consideration of a nanocrystal, a well passivated nanocrystal will have maximum ligand coverage; however, this coverage will not necessarily be a perfect, well-ordered monolayer because of the packing dependence on particle and ligand size as well as the number of ligands present. Smaller particles (those <4.4 nm) have less efficient packing due to the smaller facets and overall higher curvature of the surface. Above the 4.4 nm size the packing is determined by the chain length to radius ratio. As the three sizes of particles used in these studies are above this threshold, we expect that they have similar packing and observed this, as shown in Figure C.19.[32, 36] In the case of CdSe quantum dots, it has also been shown that the surface Cd:Se ratio will affect ligand ordering with a higher ratio of Cd:Se having more disorder.[36] It is the purpose of these measurements to understand how washing and removing ligands at the interface impacts ligand disorder at the surface. This is information that is not known based on previous measurements, and

as such, the presented SFG measurements below demonstrate how ordering changes on chemical modification of the surface. It is expected that as ligands are removed there will be an increase in the volume available for the alkyl chain of the ligand to rotate into different conformations and angles, as illustrated in Figure 5.3a which proceeds from a highly passivized nanocrystal to a less packed surface due to the removal of ligands and finally to a nanoparticle with suitable volume around ligands such that they can assume gauche configurations.[35] This conformation change intensifies SFG signal from the methylene stretch since the symmetry of the gauche configuration along the alkyl chain is broken, as can be seen in Figure 5.3b.[40-43, 62-63] The stretch from the terminal methyl is present despite configuration of the alkyl chain; thus, by comparing the ratio of methylene to methyl stretch the amount of disorder in the ligands can be evaluated. The number of gauche configurations is dependent on the thermodynamics of the system and at room temperature is expected to produce single gauche transitions with the configuration being at the outer portion of the alkyl chain.[36, 39, 64]

Each SFG spectra shown in Figure 5.4 has four distinct features near 2846, 2868, 2903, and 2929 cm^{-1}. The symmetric methylene peak (-CH_2,*s*) is identified around 2846 cm^{-1} and the symmetric methyl (-CH_3,*s*) peak is around 2868 cm^{-1}, while the asymmetric stretches (-CH_2,*as* and –CH_3,*as*) are tentatively identified at 2903 and 2929 cm^{-1}, respectively. These values closely resemble those reported previously for alkyl chains of similar size.[33-34, 36, 50, 59-60] The exact assignments of the asymmetric bands are not the focus of this work, and due to ambiguities in a precise assignment, we choose not to use these bands in analysis of ligand ordering at the QD interfaces. It should be noted that broadening and shifting of peaks was observed in all sample sets between washes, quantum dot size, and nonsolvent (further information in Appendix C). This broadening is most likely due to changes in the surface chemical environment resulting from both the removal of ligands and drying on the surface of the quartz substrates, which allowed for the evaporation of both the hexanes and nonsolvents. As seen in Figure 5.4, the more washes the quantum dots undergo the smaller the difference in amplitude between the -CH_2,*s* and the -CH_3,*s* peaks. The same trend can be gleaned from the asymmetric region as well; however, this region is more complicated to analyze due to the number of peaks and complicated assignments in this region. Specifically, as mentioned above these assignments include the asymmetric methylene and methyl stretches as well as Fermi resonances from the symmetric stretches.[33-34, 36, 50, 59-61] Therefore, the ratio of methylene to methyl stretches was not characterized for the asymmetric region. There are no obvious signals in the vSFG that can be attributed to methanol (symmetric methyl stretches around 2825 cm^{-1}), as seen in Figure 5.4, or acetone (symmetric methyl stretches between 2920 and 2925 cm^{-1}), as seen in Figure C.24.[50, 62] This indicates weak adsorption or poor ordering of nonsolvents at the surface. An explanation of this behavior arises from the fact that on resuspension of the precipitated nanocrystals the equilibrium of adsorbed nonsolvents at the particle shifts to displace these species in the bulk solution. Overall, this leads to the conclusion that the decrease in PL (Figure 5.2) is largely due to the formation of surface trap states due to dangling bonds from ligand loss as opposed to nonsolvent adsorption.

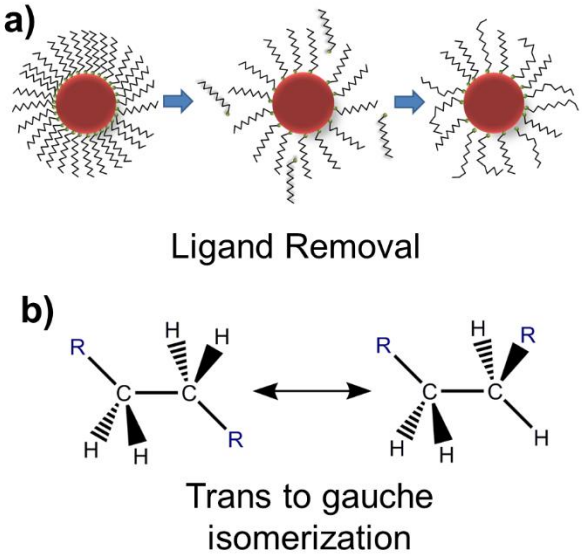

Figure 5.3 Illustration of ligand removal effects on ligand configuration. Ligand removal allows for configuration changes from trans to gauche in the alkyl chain of the octadecylamine (as shown in b)

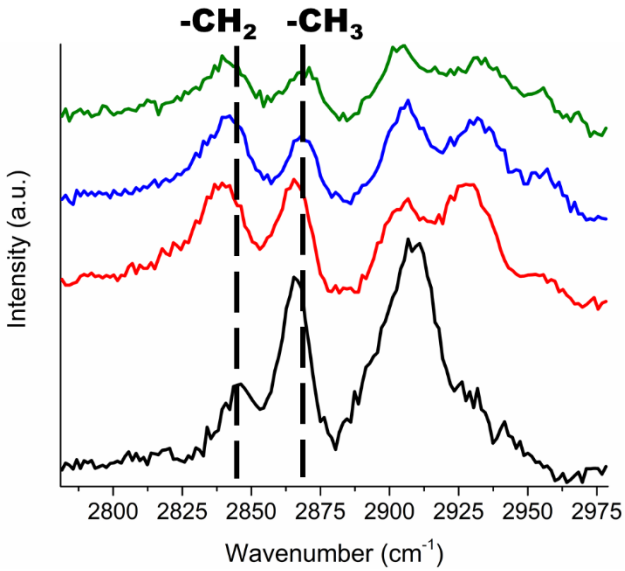

Figure 5.4 Representative vSFG spectra for 4.6 nm CdSe quantum dots washed with methanol. Spectra from bottom to top correspond to zero, one, three, and four washes, respectively. Spectra are separated vertically for clarity. The symmetric stretches used for the analysis shown in Figure 5.5 are highlighted

Following the work of Peterson, et.al., the peak ratio of the methylene to methyl ratio was calculated by using the peak area of the symmetric methylene (-CH_2,*s*) stretch divided by the sum of both the symmetric peak areas (-CH_2,*s* and –CH_3,*s*).[40] Using the peak area instead of the amplitude allows for determination of these ratios with explicit account for peak broadening. These ratios are shown in Figure 5.5 as a function of number of washes. When comparing the peak fraction of -CH_2,*s*, similar trends for both nonsolvents were observed. The change in peak fraction of -CH_2,*s* from the zeroth to the first wash depicts a clear increase in the occurrence of the methylene bands and therefore an increase in ligand disorder (Figures 5.4 and 5.5). This indicates that ligand removal is accompanied by an increase in the rotational volume allowed per ligand.[42] As the number of washes increases there are still subtle changes in the amount of disorder introduced to the ligands as the peak fraction area of -CH_2,*s* levels off, which is not apparent in the PL (Figure 5.2). Since ligand signal is still present through the fourth wash, it is clear that ligands are still present at the QD surface and that the largest change in the ordering occurs during the initial wash. L-type ligands have a weaker dative bond; therefore the removal of these ligands is straightforward, which is supported by previous studies showing strong ligand removal during the precipitation-resuspension of nanocrystals and smaller subsequent removals beyond one wash.[25, 27] For these reasons, the peak fraction ratio is explained by a ligand removal process where the first wash has a significant impact and continued washing has subtle effects and with small changes to the confirmation of the chain of the ligands. Vibrational SFG measurements on mixed monolayers of octadecyltrichlorosilane (C18) and dodecyltrichlorosilane (C12) on silica substrate by Barrett, *et. al.* showed similar sensitivity to disorder.[40] Overall, the fact that vSFG is sensitive to subtle changes in ligand conformation casts it as an optimal technique to study nanoparticle surface chemistry including the impact of other ligand species, such as X- and Z-type ligands with different bonding character.

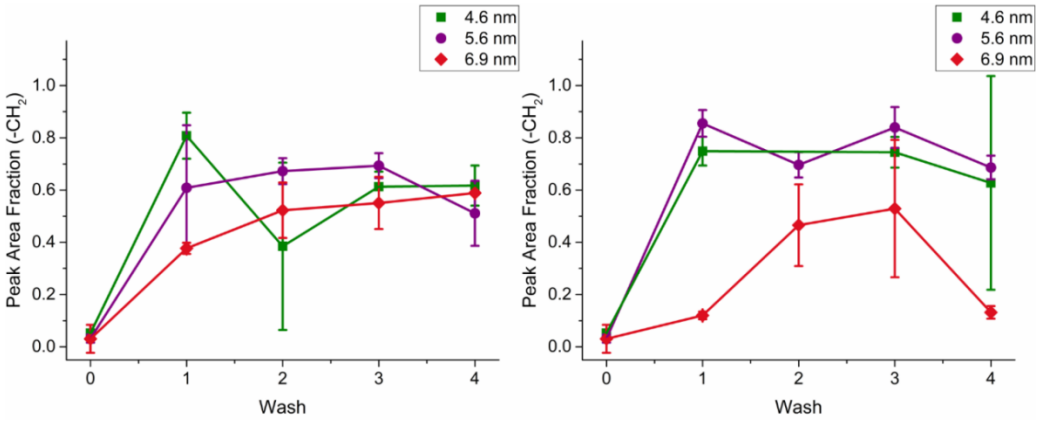

Figure 5.5 Peak area fraction of symmetric methylene stretch to both symmetric stretches determined using acetone (left) and methanol (right) as the nonsolvent, respectively. Error bars represent the standard deviation of the averaged ratio from different spatial positions

Conclusion

Vibrational sum frequency generation spectroscopy is used here to characterize the removal of ligands from the surface of CdSe quantum dots. We find a change in the ratio of methylene to methyl stretch from octadecylamine on the surface of quantum dots as the ligand was removed through a precipitation-resuspension process. The increase of the methylene to methyl stretch is due to an increased presence of gauche configuration along the alkyl chain of the ligand, which appears when the packing of the ligands decreases. The washing process reveals a significant removal of the L-type ligand during the first wash in both the SFG and photoluminescence measurements. However, the SFG measurements displayed a more gradual removal of ligands through the subsequent washes which was not represented in the PL measurements. Future work would be extended to X-type ligands where slower and more controlled removal is expected. Further extension of this technique could include the probing of different stretches specific to other regions of the ligand instead of the alkyl chain in order to better characterize ligand attachment to the surface.

References

1. Kim, J. Y.; Voznyy, O.; Zhitomirsky, D.; Sargent, E. H., 25th Anniversary Article: Colloidal Quantum Dot Materials and Devices: A Quarter-Century of Advances. *Adv. Mater.* **2013**, *25*, 4986-5010.
2. Boles, M. A.; Ling, D.; Hyeon, T.; Talapin, D. V., The Surface Science of Nanocrystals. *Nature Materials* **2016**, *15*, 141.
3. Owen, J., The Coordination Chemistry of Nanocrystal Surfaces. *Science* **2015**, *347*, 615.
4. Kalyuzhny, G.; Murray, R. W., Ligand Effects on Optical Properties of Cdse Nanocrystals. *J. Phys. Chem. B* **2005**, *109*, 7012-7021.
5. Gao, Y.; Peng, X., Crystal Structure Control of Cdse Nanocrystals in Growth and Nucleation: Dominating Effects of Surface Versus Interior Structure. *J. Am. Chem. Soc.* **2014**, *136*, 6724-6732.
6. Hines, D. A.; Kamat, P. V., Recent Advances in Quantum Dot Surface Chemistry. *ACS Appl. Mater. Interfaces* **2014**, *6*, 3041-3057.
7. Kovtun, O.; Arzeta-Ferrer, X.; Rosenthal, S. J., Quantum Dot Approaches for Target-Based Drug Screening and Multiplexed Active Biosensing. *Nanoscale* **2013**, *5*, 12072-12081.
8. Chandramohan, S.; Ryu, B. D.; Kim, H. K.; Hong, C.-H.; Suh, E.-K., Trap-State-Assisted White Light Emission from a Cdse Nanocrystal Integrated Hybrid Light-Emitting Diode. *Opt. Lett.* **2011**, *36*, 802-804.
9. Rosson, T. E.; Claiborne, S. M.; McBride, J. R.; Stratton, B. S.; Rosenthal, S. J., Bright White Light Emission from Ultrasmall Cadmium Selenide Nanocrystals. *J. Am. Chem. Soc.* **2012**, *134*, 8006-8009.
10. Hoffman, J. B.; Choi, H.; Kamat, P. V., Size-Dependent Energy Transfer Pathways in Cdse Quantum Dot–Squaraine Light-Harvesting Assemblies: Förster Versus Dexter. *J. Phys. Chem. C* **2014**, *118*, 18453-18461.
11. Anderson, N. C.; Hendricks, M. P.; Choi, J. J.; Owen, J. S., Ligand Exchange and the Stoichiometry of Metal Chalcogenide Nanocrystals: Spectroscopic Observation of Facile Metal-Carboxylate Displacement and Binding. *J. Am. Chem. Soc.* **2013**, *135*, 18536-18548.
12. Green, M. L. H., A New Approach to the Formal Classification of Covalent Compounds of the Elements. *J. Organomet. Chem.* **1995**, *500*, 127-148.
13. Lawrence, K. N.; Dutta, P.; Nagaraju, M.; Teunis, M. B.; Muhoberac, B. B.; Sardar, R., Dual Role of Electron-Accepting Metal-Carboxylate Ligands: Reversible Expansion of Exciton Delocalization and Passivation of Nonradiative Trap-States in Molecule-Like Cdse Nanocrystals. *J. Am. Chem. Soc.* **2016**, *138*, 12813-12825.
14. Chen, P. E.; Anderson, N. C.; Norman, Z. M.; Owen, J. S., Tight Binding of Carboxylate, Phosphonate, and Carbamate Anions to Stoichiometric Cdse Nanocrystals. *J. Am. Chem. Soc.* **2017**, *139*, 3227-3236.
15. Owen, J. S.; Park, J.; Trudeau, P.-E.; Alivisatos, A. P., Reaction Chemistry and Ligand Exchange at Cadmium−Selenide Nanocrystal Surfaces. *J. Am. Chem. Soc.* **2008**, *130*, 12279-12281.

16. Baker, D. R.; Kamat, P. V., Tuning the Emission of Cdse Quantum Dots by Controlled Trap Enhancement. *Langmuir* **2010**, *26*, 11272-11276.
17. Morris-Cohen, A. J.; Donakowski, M. D.; Knowles, K. E.; Weiss, E. A., The Effect of a Common Purification Procedure on the Chemical Composition of the Surfaces of Cdse Quantum Dots Synthesized with Trioctylphosphine Oxide. *J. Phys. Chem. C* **2010**, *114*, 897-906.
18. Hassinen, A.; Moreels, I.; De Nolf, K.; Smet, P. F.; Martins, J. C.; Hens, Z., Short-Chain Alcohols Strip X-Type Ligands and Quench the Luminescence of Pbse and Cdse Quantum Dots, Acetonitrile Does Not. *J. Am. Chem. Soc.* **2012**, *134*, 20705-20712.
19. Shakeri, B.; Meulenberg, R. W., A Closer Look into the Traditional Purification Process of Cdse Semiconductor Quantum Dots. *Langmuir* **2015**, *31*, 13433-13440.
20. Murray, C. B.; Norris, D. J.; Bawendi, M. G., Synthesis and Characterization of Nearly Monodisperse Cde (E = Sulfur, Selenium, Tellurium) Semiconductor Nanocrystallites. *J. Am. Chem. Soc.* **1993**, *115*, 8706-8715.
21. Qu, L.; Peng, X., Control of Photoluminescence Properties of Cdse Nanocrystals in Growth. *J. Am. Chem. Soc.* **2002**, *124*, 2049-2055.
22. Qu, L.; Peng, Z. A.; Peng, X., Alternative Routes toward High Quality Cdse Nanocrystals. *Nano Lett.* **2001**, *1*, 333-337.
23. Siy, J. T.; Brauser, E. M.; Bartl, M. H., Low-Temperature Synthesis of Cdse Nanocrystal Quantum Dots. *Chem. Commun.* **2011**, *47*, 364-366.
24. Bullen, C.; Mulvaney, P., The Effects of Chemisorption on the Luminescence of Cdse Quantum Dots. *Langmuir* **2006**, *22*, 3007-3013.
25. Munro, A. M.; Jen-La Plante, I.; Ng, M. S.; Ginger, D. S., Quantitative Study of the Effects of Surface Ligand Concentration on Cdse Nanocrystal Photoluminescence. *J. Phys. Chem. C* **2007**, *111*, 6220-6227.
26. Pokrant, S.; Whaley, K. B., Tight-Binding Studies of Surface Effects on Electronic Structure of Cdse Nanocrystals: The Role of Organic Ligands, Surface Reconstruction, and Inorganic Capping Shells. *The European Physical Journal D - Atomic, Molecular, Optical and Plasma Physics* **1999**, *6*, 255-267.
27. Morris-Cohen, A. J.; Malicki, M.; Peterson, M. D.; Slavin, J. W. J.; Weiss, E. A., Chemical, Structural, and Quantitative Analysis of the Ligand Shells of Colloidal Quantum Dots. *Chem. Mater.* **2013**, *25*, 1155-1165.
28. Knittel, F.; Gravel, E.; Cassette, E.; Pons, T.; Pillon, F.; Dubertret, B.; Doris, E., On the Characterization of the Surface Chemistry of Quantum Dots. *Nano Lett.* **2013**, *13*, 5075-5078.
29. Meulenberg, R. W.; Strouse, G. F., Chain Packing Analysis of the Passivating Layer on Nanocrystalline Quantum Dot Surfaces. *J. Phys. Chem. B* **2001**, *105*, 7438-7445.
30. Grenland, J. J.; Lin, C.; Gong, K.; Kelley, D. F.; Kelley, A. M., Resonance Raman Investigation of the Interaction between Aromatic Dithiocarbamate Ligands and Cdse Quantum Dots. *J. Phys. Chem. C* **2017**, *121*, 7056-7061.
31. Frederick, M. T.; Weiss, E. A., Relaxation of Exciton Confinement in Cdse Quantum Dots by Modification with a Conjugated Dithiocarbamate Ligand. *ACS Nano* **2010**, *4*, 3195-3200.

32. Meulenberg, R. W.; Bryan, S.; Yun, C. S.; Strouse, G. F., Effects of Alkylamine Chain Length on the Thermal Behavior of Cdse Quantum Dot Glassy Films. *J. Phys. Chem. B* **2002**, *106*, 7774-7780.
33. Barrett, A.; Petersen, P. B., Order of Dry and Wet Mixed-Length Self-Assembled Monolayers. *J. Phys. Chem. C* **2015**, *119*, 23943-23950.
34. Bordenyuk, A. N.; Weeraman, C.; Yatawara, A.; Jayathilake, H. D.; Stiopkin, I.; Liu, Y.; Benderskii, A. V., Vibrational Sum Frequency Generation Spectroscopy of Dodecanethiol on Metal Nanoparticles. *J. Phys. Chem. C* **2007**, *111*, 8925-8933.
35. Weeraman, C.; Yatawara, A. K.; Bordenyuk, A. N.; Benderskii, A. V., Effect of Nanoscale Geometry on Molecular Conformation: Vibrational Sum-Frequency Generation of Alkanethiols on Gold Nanoparticles. *J. Am. Chem. Soc.* **2006**, *128*, 14244-14245.
36. Frederick, M. T.; Achtyl, J. L.; Knowles, K. E.; Weiss, E. A.; Geiger, F. M., Surface-Amplified Ligand Disorder in Cdse Quantum Dots Determined by Electron and Coherent Vibrational Spectroscopies. *J. Am. Chem. Soc.* **2011**, *133*, 7476-7481.
37. Aliaga, C.; Park, J. Y.; Yamada, Y.; Lee, H. S.; Tsung, C.-K.; Yang, P.; Somorjai, G. A., Sum Frequency Generation and Catalytic Reaction Studies of the Removal of Organic Capping Agents from Pt Nanoparticles by Uv−Ozone Treatment. *J. Phys. Chem. C* **2009**, *113*, 6150-6155.
38. Das, S. K.; Sengupta, S.; Velarde, L., Interfacial Surfactant Ordering in Thin Films of Sds-Encapsulated Single-Walled Carbon Nanotubes. *J. Phys. Chem. Lett.* **2016**, *7*, 320-326.
39. Jasieniak, J.; Smith, L.; van Embden, J.; Mulvaney, P.; Califano, M., Re-Examination of the Size-Dependent Absorption Properties of Cdse Quantum Dots. *J. Phys. Chem. C* **2009**, *113*, 19468-19474.
40. Ji, X.; Copenhaver, D.; Sichmeller, C.; Peng, X., Ligand Bonding and Dynamics on Colloidal Nanocrystals at Room Temperature: The Case of Alkylamines on Cdse Nanocrystals. *J. Am. Chem. Soc.* **2008**, *130*, 5726-5735.
41. Lim, H.; Woo, J. Y.; Lee, D. C.; Lee, J.; Jeong, S.; Kim, D., Continuous Purification of Colloidal Quantum Dots in Large-Scale Using Porous Electrodes in Flow Channel. *Sci. Rep.* **2017**, *7*, 43581.
42. Aldana, J.; Wang, Y. A.; Peng, X., Photochemical Instability of Cdse Nanocrystals Coated by Hydrophilic Thiols. *J. Am. Chem. Soc.* **2001**, *123*, 8844-8850.
43. Sambur, J. B.; Parkinson, B. A., Size Selective Photoetching of Cdse Quantum Dot Sensitizers on Single-Crystal Tio2. *ACS Appl. Mater. Interfaces* **2014**, *6*, 21916-21920.
44. Morris-Cohen, A. J.; Frederick, M. T.; Lilly, G. D.; McArthur, E. A.; Weiss, E. A., Organic Surfactant-Controlled Composition of the Surfaces of Cdse Quantum Dots. *J. Phys. Chem. Lett.* **2010**, *1*, 1078-1081.
45. Doughty, B.; Goverapet Srinivasan, S.; Bryantsev, V. S.; Lee, D.; Lee, H. N.; Ma, Y.-Z.; Lutterman, D. A., Absolute Molecular Orientation of Isopropanol at Ceria (100) Surfaces: Insight into Catalytic Selectivity from the Interfacial Structure. *J. Phys. Chem. C* **2017**, *121*, 14137-14146.

46. Doughty, B.; Yin, P.; Ma, Y.-Z., Adsorption, Ordering, and Local Environments of Surfactant-Encapsulated Polyoxometalate Ions Probed at the Air–Water Interface. *Langmuir* **2016**, *32*, 8116-8122.
47. Voylov, D. N.; Holt, A. P.; Doughty, B.; Bocharova, V.; Meyer, H. M.; Cheng, S.; Martin, H.; Dadmun, M.; Kisliuk, A.; Sokolov, A. P., Unraveling the Molecular Weight Dependence of Interfacial Interactions in Poly(2-Vinylpyridine)/Silica Nanocomposites. *ACS Macro Lett.* **2017**, *6*, 68-72.
48. Tan, S.; Gray, M. B.; Kidder, M. K.; Cheng, Y.; Daemen, L. L.; Lee, D.; Lee, H. N.; Ma, Y.-Z.; Doughty, B.; Lutterman, D. A., Insight into the Selectivity of Isopropanol Conversion at Strontium Titanate (100) Surfaces: A Combination Kinetic and Spectroscopic Study. *ACS Catalysis* **2017**.
49. Lu, R.; Gan, W.; Wu, B.-h.; Chen, H.; Wang, H.-f., Vibrational Polarization Spectroscopy of Ch Stretching Modes of the Methylene Group at the Vapor/Liquid Interfaces with Sum Frequency Generation. *J. Phys. Chem. B* **2004**, *108*, 7297-7306.
50. Lu, R.; Gan, W.; Wu, B.-h.; Zhang, Z.; Guo, Y.; Wang, H.-f., C−H Stretching Vibrations of Methyl, Methylene and Methine Groups at the Vapor/Alcohol (N = 1−8) Interfaces. *J. Phys. Chem. B* **2005**, *109*, 14118-14129.
51. Cohen, R.; Kronik, L.; Shanzer, A.; Cahen, D.; Liu, A.; Rosenwaks, Y.; Lorenz, J. K.; Ellis, A. B., Molecular Control over Semiconductor Surface Electronic Properties: Dicarboxylic Acids on Cdte, Cdse, Gaas, and Inp. *J. Am. Chem. Soc.* **1999**, *121*, 10545-10553.
52. Neu, D. R.; Olson, J. A.; Ellis, A. B., Photoluminescence as a Probe of the Adsorption of Gaseous Boranes onto the Surface of Cadmium Selenide Crystals. *J. Phys. Chem.* **1993**, *97*, 5713-5716.
53. Moreels, I.; Martins, J. C.; Hens, Z., Ligand Adsorption/Desorption on Sterically Stabilized Inp Colloidal Nanocrystals: Observation and Thermodynamic Analysis. *ChemPhysChem* **2006**, *7*, 1028-1031.
54. Talapin, D. V.; Rogach, A. L.; Kornowski, A.; Haase, M.; Weller, H., Highly Luminescent Monodisperse Cdse and Cdse/Zns Nanocrystals Synthesized in a Hexadecylamine−Trioctylphosphine Oxide−Trioctylphospine Mixture. *Nano Lett.* **2001**, *1*, 207-211.
55. de Mello Donegá, C.; Hickey, S. G.; Wuister, S. F.; Vanmaekelbergh, D.; Meijerink, A., Single-Step Synthesis to Control the Photoluminescence Quantum Yield and Size Dispersion of Cdse Nanocrystals. *J. Phys. Chem. B* **2003**, *107*, 489-496.
56. Cooper, J. K.; Franco, A. M.; Gul, S.; Corrado, C.; Zhang, J. Z., Characterization of Primary Amine Capped Cdse, Znse, and Zns Quantum Dots by Ft-Ir: Determination of Surface Bonding Interaction and Identification of Selective Desorption. *Langmuir* **2011**, *27*, 8486-8493.
57. Conboy, J. C.; Messmer, M. C.; Richmond, G. L., Effect of Alkyl Chain Length on the Conformation and Order of Simple Ionic Surfactants Adsorbed at the D2o/Ccl4 Interface as Studied by Sum-Frequency Vibrational Spectroscopy. *Langmuir* **1998**, *14*, 6722-6727.

58. Stanners, C. D.; Du, Q.; Chin, R. P.; Cremer, P.; Somorjai, G. A.; Shen, Y. R., Polar Ordering at the Liquid-Vapor Interface of N-Alcohols (C1-C8). *Chem. Phys. Lett.* **1995**, *232*, 407-413.
59. Gurau, M. C.; Castellana, E. T.; Albertorio, F.; Kataoka, S.; Lim, S.-M.; Yang, R. D.; Cremer, P. S., Thermodynamics of Phase Transitions in Langmuir Monolayers Observed by Vibrational Sum Frequency Spectroscopy. *J. Am. Chem. Soc.* **2003**, *125*, 11166-11167.
60. Allhusen, J. S.; Kimball, D. R.; Conboy, J. C., Structural Origins of Cholesterol Accelerated Lipid Flip-Flop Studied by Sum-Frequency Vibrational Spectroscopy. *J. Phys. Chem. B* **2016**, *120*, 3157-3168.
61. Tang, C. Y.; Allen, H. C., Ionic Binding of Na+ Versus K+ to the Carboxylic Acid Headgroup of Palmitic Acid Monolayers Studied by Vibrational Sum Frequency Generation Spectroscopy. *J. Phys. Chem. A* **2009**, *113*, 7383-7393.
62. Chen, H.; Gan, W.; Wu, B.-h.; Wu, D.; Guo, Y.; Wang, H.-f., Determination of Structure and Energetics for Gibbs Surface Adsorption Layers of Binary Liquid Mixture 1. Acetone + Water. *J. Phys. Chem. B* **2005**, *109*, 8053-8063.

CHAPTER 6 ♦ CONCLUSION AND FUTURE WORKS

Conclusion

The work presented in this dissertation describes the design and implementation of electronic sum frequency in a microscope apparatus. With this instrument studies utilizing two-photon fluorescence, second harmonic generation, and electronic sum frequency have been achieved. The central aspect to this work studied the surfaces of CdSe QDs. As described in chapter three, the eSFG spectra show signal below the band gap. The position of this signal supports the existence of both shallow and deep surface states, which are expected 10 meV and 300 meV from the bandgap, respectively. These surface states were also confirmed by changes in the eSFG spectra due to air exposure which is expected to alter the surface of the particles and produce surface states. Additional studies to understand the interfacial surface of CdSe QDs were completed through the use of vSFG spectroscopy. This provided information about the ligand structure at the interface while eSFG provided electronic structure. The instrument proved to be useful not only for CdSe QDs studies but also for imaging of inorganic organic lead based perovskites. The microscopy performed identified dipole moment orientation in these thin films. The instrument proved to be versatile in studying the electronic properties of a variety of chemical systems.

Future Work

Total Internal Reflectance Enhancement

An important point which was realized during the implementation of this instrument was the enhancement achieved by using the total internal reflection geometry. A common illumination technique in microscopy is to overfill the back focal plane of the objective in order to produce tightly focused light. In comparison total internal reflectance allows for the illumination of a wide area while producing an electric field that exponential decays in the z-axis. When comparing these different illumination techniques, it was observed that the total internal reflection geometry produced higher signal in KDP samples, as is illustrated in Figure 6.1. The reasoning for this enhancement has yet to be determined and is a point of future interest and work. Potential reasons for the signal enhancement include: collection efficiency, field of illuminations, or electric field components. As shown in Figure 6.1 and in chapter one, the area which produced signal in always greater in internal reflection than in a focused geometry thus the increase in signal could be related to increased sample illumination. Collection efficiency is dependent on the ability of the objective above that sample to collect the emitted light. Typically, in SHG microscopy setups the NA of both the excitation and collection objective is matched. This is done to allow for optimal collection since it has been determined that SHG signal follows the angle determined by the excitation NA. Thus, a NA mismatch as great as 0.5 to 1.49 could cause a pronounced decreased in collection efficiency. However, considering the difficulty to find UV optics the collection objective of 0.5 NA is currently the best case for eSFG microscopy. The difference in electric fields for each of the illumination geometries is also closely relates to collection efficiency since it is currently unknown how the illumination geometry effects signal propagation. Despite these questions surrounding the signal enhancement while utilizing total internal reflectance

geometry illumination, it is considering essential to the eSFG spectra collected here since the eSFG spectra of CdSe QDs was weaker than other crystalline materials, such as KDP.

Towards Single Particle Detection

The eSFG spectra produced in this work were focused on large heterogenous samples drop cast onto slides. The eSFG data would become even more useful if individual particle could be detected revealing any heterogeneity in the sample. It is feasible that the separation of some spatial areas could be done by selecting regions from the camera on the spectrograph. As shown in Figure 6.2, spatial regions could be determined by having the grating of the spectrograph as zero (a), then choosing the corresponding region when the grating is turned (b), and then processing the region to produce the spectral data (c). Initial studies were completed with KDP to show that eSFG signal was strong enough to be detected in this matter; however, samples with weaker signal could be an issue and may cause this method to be unfeasible.

Combining eSFG and vSFG

As was shown in both chapter three and four, sum frequency generation is limited to either electronic or vibrational information. While two different instruments were used to collect the data, it remains possible to combine the two techniques. By combing the two technique ligands on the surface as well as the electronic structure and how ligand modification affects electronic structure could be studied simultaneously.

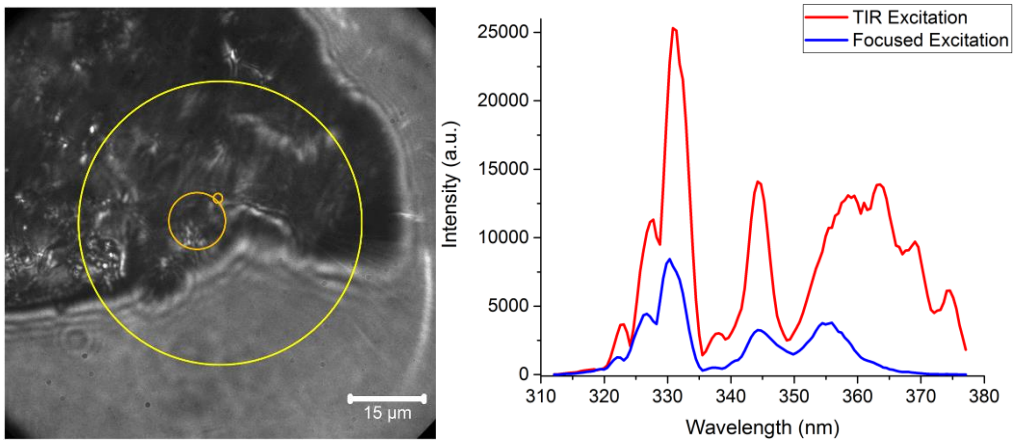

Figure 6.1 Illustrates the signal enhancement from using a total internal reflection illumination geometry compared to the more common focused illumination. Spectra to the right are eSFG signal from KDP in each of the geometries. The image to the left shows the KDP crystal with orange circle highlighting the area of SHG signal in each of the illumination geometries and the yellow circle show the estimated collection field 50 nm from the sample

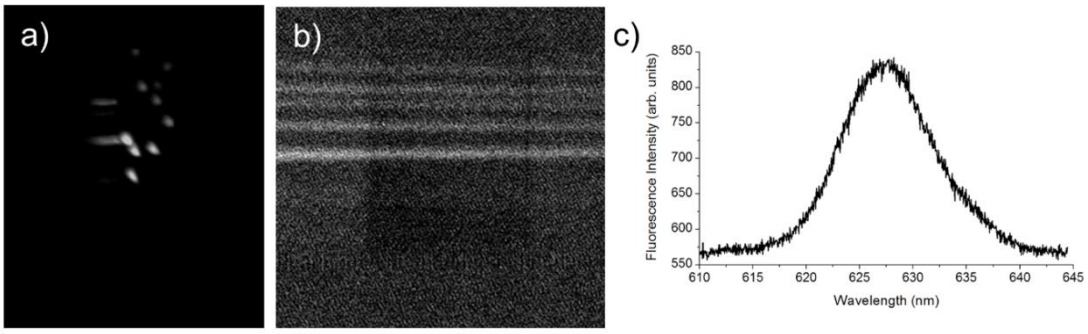

Figure 6.2 Fluorescence of Nile red microspheres in through direction imaging (a) and spectral resolution (b and c)

APPENDICES

Appendix A: Elucidation of Perovskite Film Micro-Orientations Using Two-Photon Total Internal Reflectance Fluorescence Microscopy

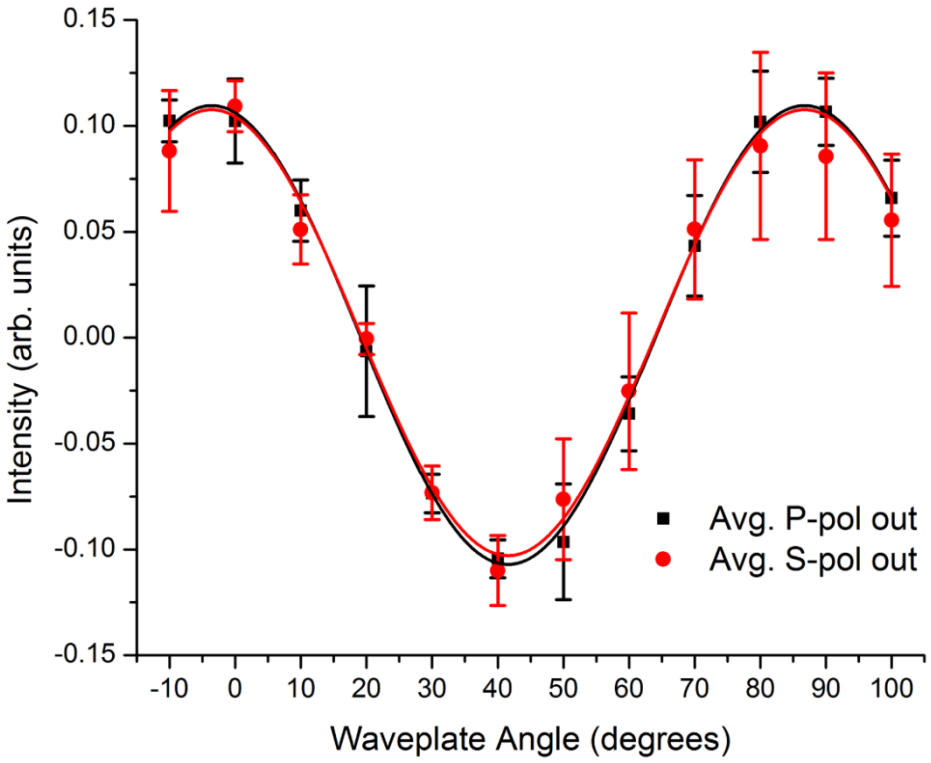

Figure A.1 Normalized emission intensity plotted as the excitation λ/2 waveplate was rotated between -10 and 100 degrees. The data was collected with a resolving polarizer in the p- (black) and s- (red) polarizing positions. Three trials were completed for each emission polarization state. These results show that the emission polarization is not dependent on the input polarization, and that the measured polarization ratio given by equation 1 reflects the orientation of the absorption transition dipole moments in the sample

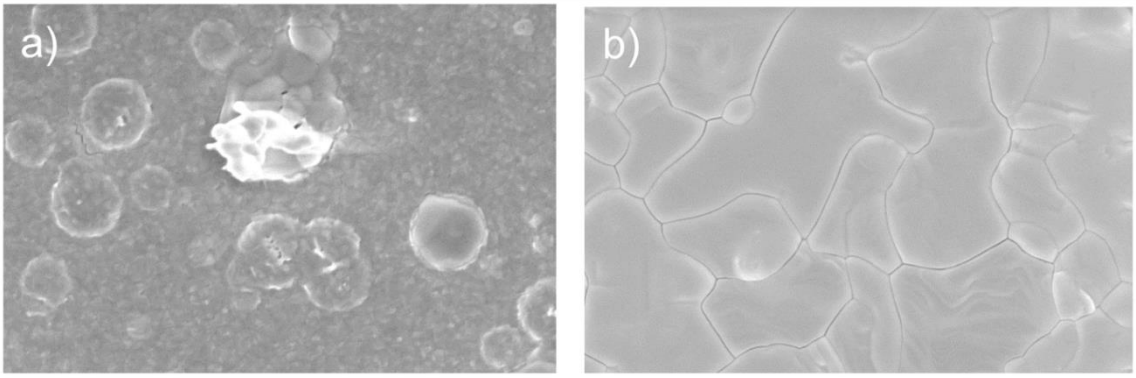

Figure A.2 Scanning electron microscope (SEM) images of perovskite thin films prepared with sequential spin-coating of PbI_2/CH_3NH_3I followed by exposure to ambient air and then thermal annealing a) non-annealed sample b) annealed for 2 hours. Image are after exposure to air

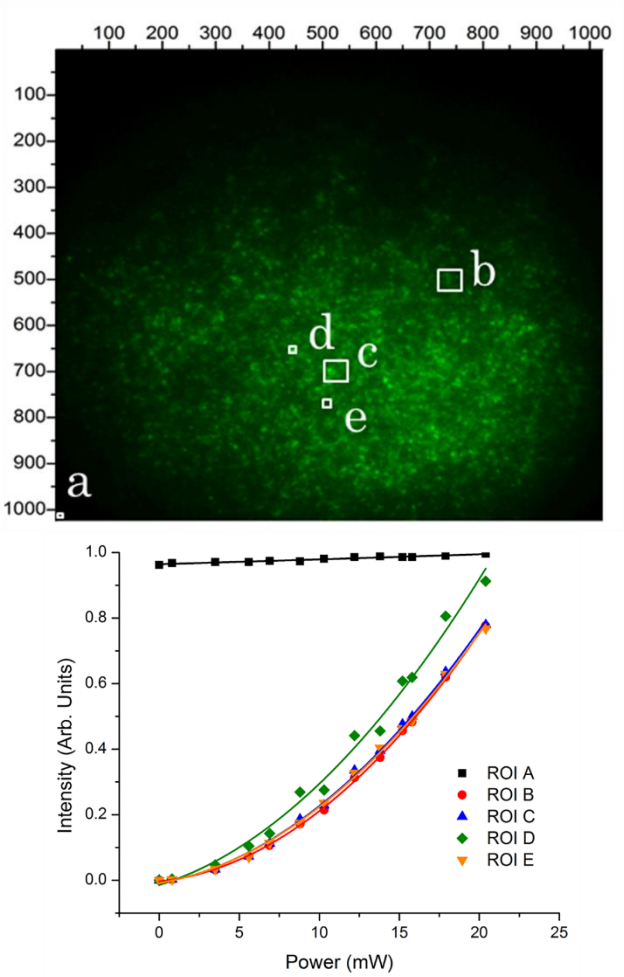

Figure A.3 Power laws are shown here for different regions of interest (ROI). ROI A refers to a non-fluorescent area out of the field of view, to serve as a consistency check. ROI B, C, D, and E were randomly selected regions of differing size, and overall intensity used to ensure there was no systematic bias in generating power laws from the images. The incident power was controlled using a polarizer and scaled using a known ratio between the point of measurement and the intensity at the objective. The entire image is 88 x 88 μm

Appendix B: Electronic Sum Frequency to Study Surfaces States of CdSe Quantum Dots

This appendix details proves complementary details for chapter four of this dissertation, including fitting parameters for UV-Vis, UV-Vis of solution versus dried on quartz, typical whitelight spectra from the PCF fiber, and a comparison of eSFG signal with less than optimal whitelight.

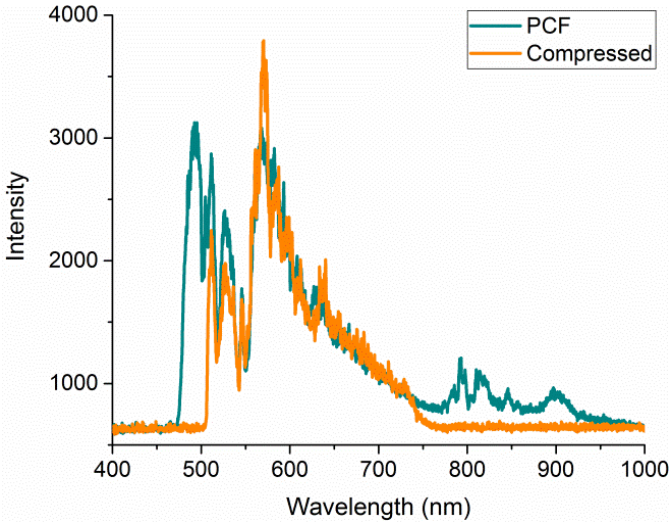

Figure B.1 Typical whitelight spectra directly after the PCF fiber and after prism compression

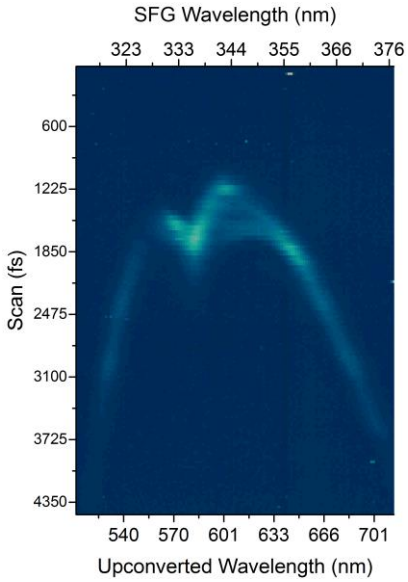

Figure B.2 Example of unprocessed eSFG spectra for CdSe QDs

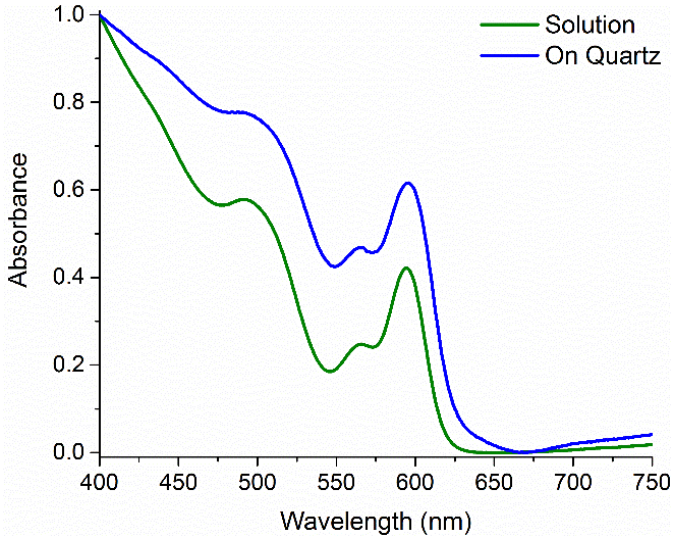

Figure B.3 UV-Vis of 4.6 nm CdSe in toluene solution and drop cast onto quartz slide

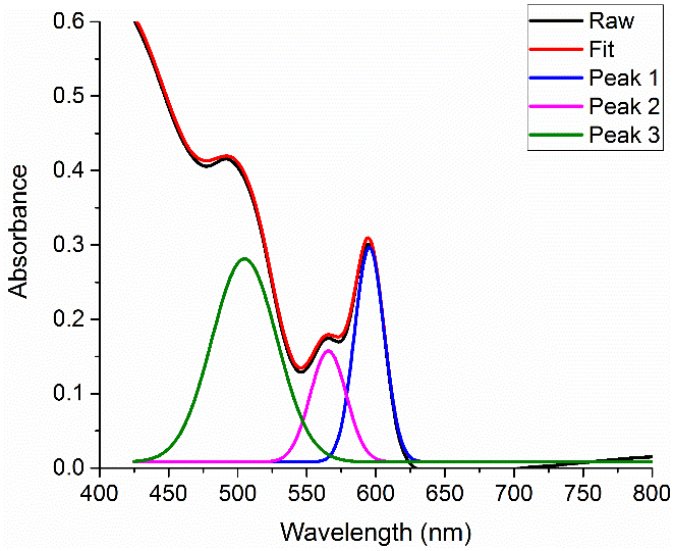

Figure B.4 Fit of UV-Vis for 4.6 nm CdSe QDs

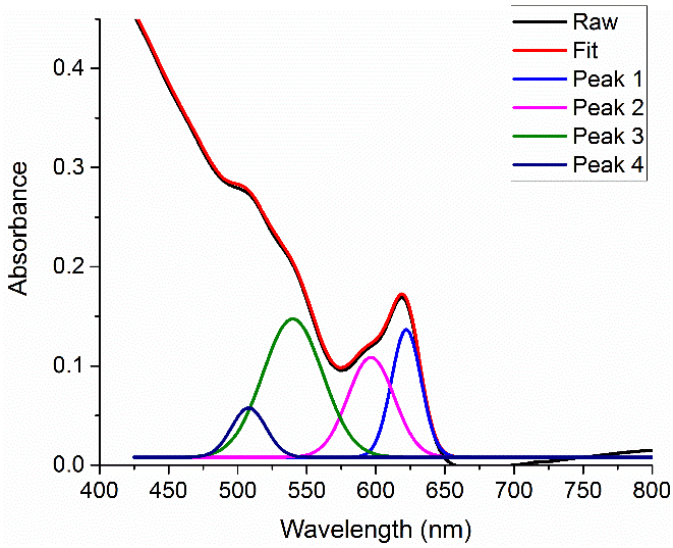

Figure B.5 Fit of UV-Vis for 5.6 nm CdSe QDs

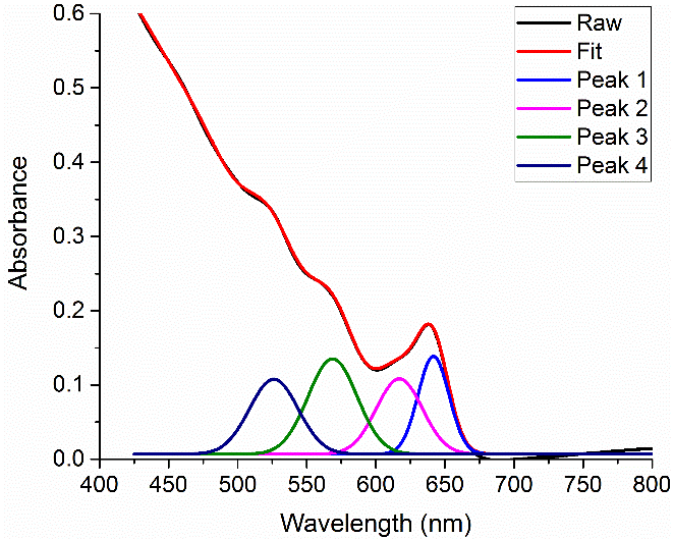

Figure B.6 Fit of UV-Vis for 6.9 nm CdSe QDs

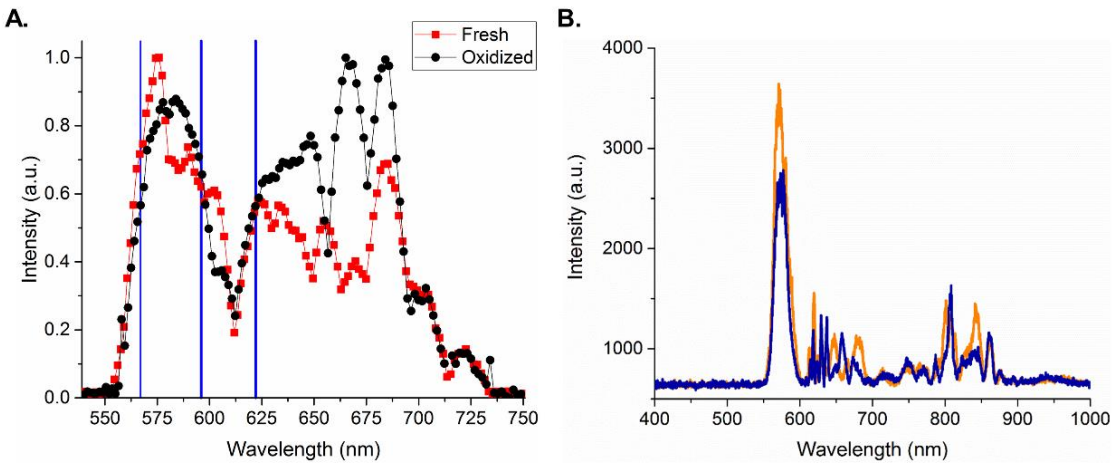

Figure B.7 Example eSFG spectra (A) with less broad whitelight (B). No eSFG signal appears when whitelight is not present in that region

Appendix C: Probing Ligand Removal and Ordering at CdSe Quantum Dot Surfaces Using Vibrational Sum Frequency Spectroscopy

This appendix supplies fitting parameters, plots showing example fitting curves, average peak positions, example spectra with acetone as nonsolvent, plots of peak position shifts, UV-Vis and photoluminescence absorption spectra for 5.6 and 6.9 nm sizes of quantum dots (QDs), proton NMR.

UV-Vis Absorption

Absorption spectra for 5.6 and 6.9 nm CdSe quantum dots are shown below (left and right, respectively). The UV-Vis data again shows that the washing does not affect the quantum dot size but only the ligands at the surface, as the first exciton absorption peak does not show a significant spectral shift. Changes in baseline are attributed to aggregation which is expected due to the loss of stabilizing ligand.

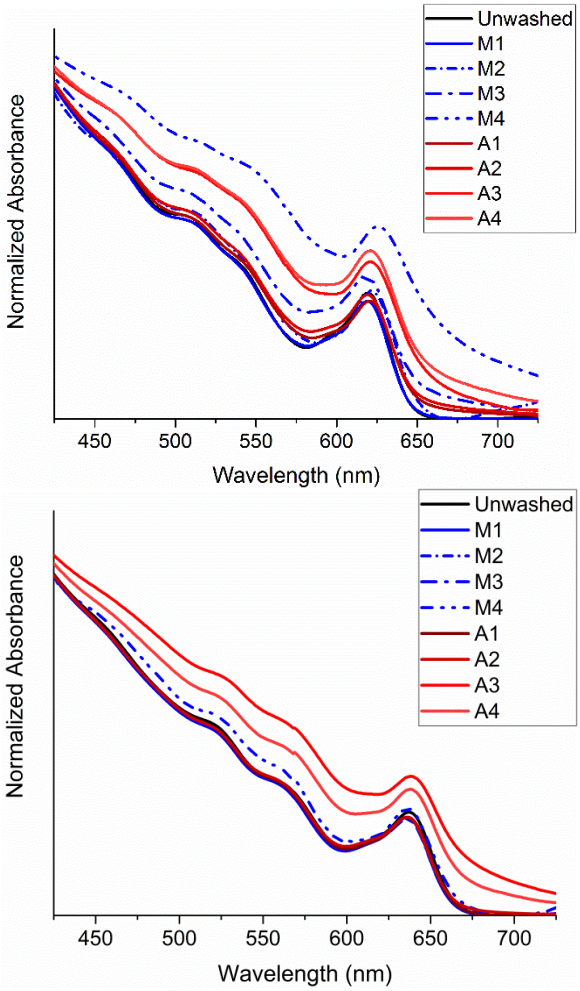

Figure C.1 UV-Vis absorption spectra for 5.6 (right) and 6.9 (left) nm CdSe quantum dots through washing with acetone ("A") and methanol ("M")

Table C.1 Concentration of particle as determined from UV-Vis

Wash	CdSe600		CdSe620		CdSe640	
	Acetone (particles/mL)	*Methanol (particles/mL)*	*Acetone (particles/mL)*	*Methanol (particles/mL)*	*Acetone (particles/mL)*	*Methanol (particles/mL)*
0	4.52E+14	4.52E+14	1.51E+14	1.51E+14	1.51E+14	1.51E+14
1	3.24E+14	2.21E+14	1.16E+14	1.54E+14	1.42E+14	1.42E+14
2	3.63E+14	2.66E+14	1.16E+14	1.66E+13	1.24E+14	1.06E+14
3	2.86E+14	6.78E+13	2.38E+13	7.78E+13	4.01E+13	1.15E+14
4	2.39E+14	5.92E+13	5.27E+13	4.18E+13	3.03E+13	7.96E+12
Order of Mag. Diff.	0.28	0.88	0.46	0.56	0.70	1.28

Photoluminescence Data

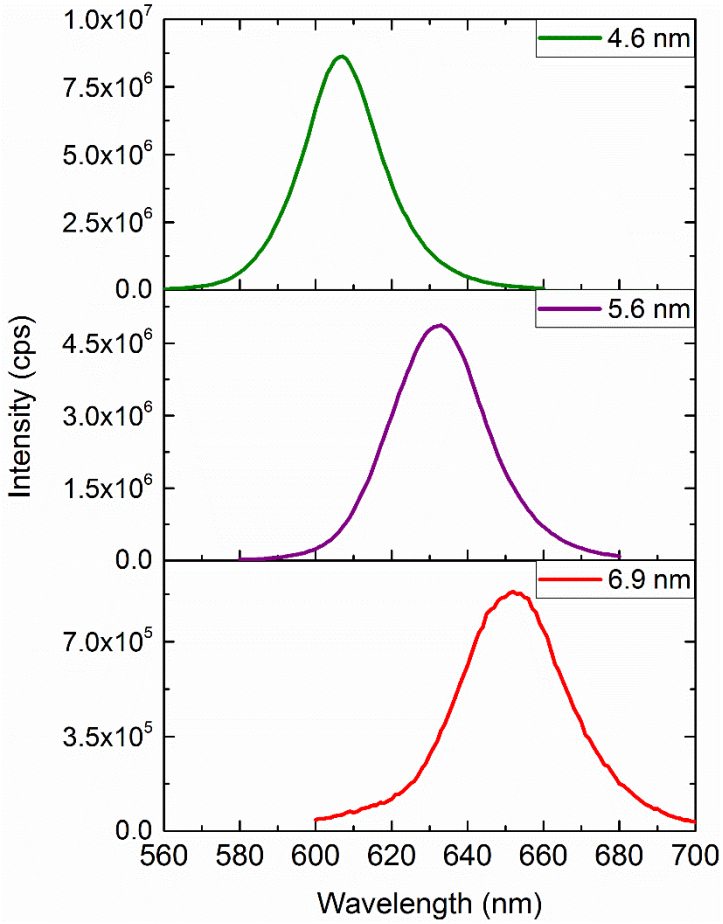

Figure C.2 Photoluminescence emission spectra of unwashed solutions with 400 nm excitation

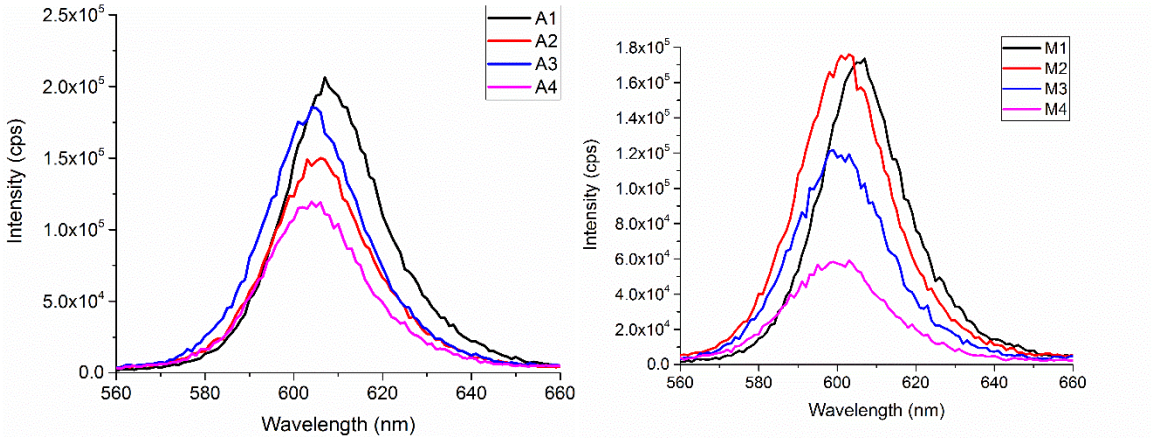

Figure C.3 Photoluminescence spectra for 4.6 nm QDs washed samples, acetone (left) and methanol (right) as nonsolvent

Table C.2 Photoluminescence data for 4.6 nm CdSe QDs including peak center (XC), amplitude (A), and peak width (W)

	UW	M1	M2	M3	M4	A1	A2	A3	A4
XC	607.0	606.5	601.8	600.8	599.9	608.9	605.9	604.6	604.6
A	2.29E8	4.70E6	4.94E6	3.50E6	1.79E6	5.60E6	4.06E6	4.99E6	3.29E6
W	26.3	27.6	28.5	29.2	31.0	27.9	27.7	27.7	28.0
Conc. Scale		*2.04*	*1.70*	*6.66*	*7.64*	*1.39*	*1.25*	*1.58*	*1.89*
Scaled A	2.29E8	9.58E6	8.38E6	2.33E7	1.37E7	7.81E6	5.06E6	7.88E6	6.21E6

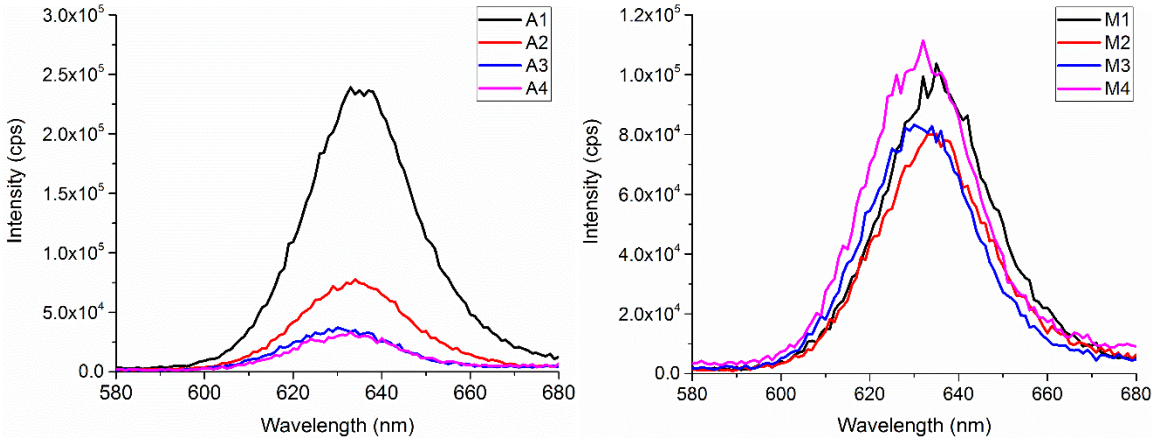

Figure C.4 Photoluminescence spectra for 5.6 nm QDs washed samples, acetone (left) and methanol (right) as nonsolvent

Table C.3 Photoluminescence data for 5.6 nm CdSe QDs including peak center (XC), amplitude (A), and peak width (W)

	UW	M1	M2	M3	M4	A1	A2	A3	A4
XC	632.4	635.4	634.4	631.6	631.8	635.5	634.0	631.1	632.7
A	1.55E8	3.05E6	2.50E6	2.57E6	3.24E6	7.44E6	2.37E6	1.08E6	945563.6
W	30.53	30.80	31.40	30.16	30.11	30.68	30.91	30.07	30.59
Conc. Scale		*0.98*	*9.07*	*1.93*	*3.60*	*1.30*	*1.30*	*6.32*	*2.85*
Scaled A	1.55E8	2.99E6	2.27E7	4.98E6	1.17E7	9.65E6	3.09E6	6.81E6	2.70E6

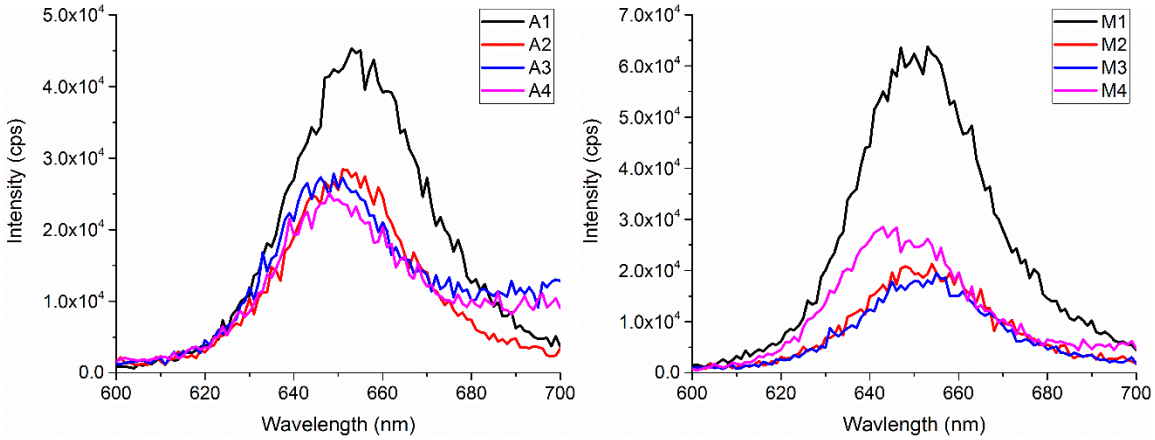

Figure C.5 Photoluminescence for 6.9 nm QDs washed samples, acetone (left) and methanol (right) as nonsolvent

Table C.4 Photoluminescence data for 6.9 nm CdSe QDs including peak center (XC), amplitude (A), and peak width (W)

	UW	M1	M2	M3	M4	A1	A2	A3	A4
XC	651.9	652.0	652.8	653.0	647.7	654.9	652.4	654.1	653.7
A	3.00E7	2.27E6	7.41E5	6.40E5	1.04E6	1.67E6	9.53E5	1.17E6	9.79E5
W	33.80	35.67	36.54	35.97	37.67	37.34	34.91	49.75	46.42
Conc. Scale		*1.06*	*1.42*	*1.31*	*18.91*	*1.06*	*1.22*	*3.75*	*4.98*
Scaled A	3.00E7	2.40E6	1.05E6	8.40E5	1.96E7	1.77E6	1.16E6	4.40E6	4.87E6

Proton NMR

Proton NMR was performed on a Bruker Avance 400 MHz. Chemical shifts were identified for octadecylamine (99%, Stream) at 0.88, 1.26, 2.67, 7.27 ppm, corresponding to methyl, methylene stretches along the backbone, alpha hydrogens, and chloroform (solvent). Experiments were not done in hexane due to overwhelming signal from the solvent prohibiting studies of the ligands.

Washed samples were prepared in the same way as described in the main text expect solutions were resuspended in 698 µL of d-chloroform (Sigma-Aldrich); 2 µL of dibromomethane (99 %, Sigma-Aldrich) was used as an internal standard. Samples were not diluted for NMR experiments and volumes of 600 µL was added to the NMR tube. For unwashed samples, 600 µL was taken neat from the vial and 10 µL of the internal standard was added. For washed QDs samples (sample 2, 3, 4, 5), chemical shifts were identified at 0.86, 1.26, 4.92, and 7.26 ppm for each sample. Depending on the nonsolvent, acetone and methanol peaks were observed at 2.16 and 3.45, respectively Unwashed QDs (sample 1) were taken directly from the commercial source and dibromomethane was added as an internal standard. Sharp peaks at 1.00 and 1.40 were observed for the unwashed samples on top of the broader signal corresponding to ligands attached to the particle surface. The internal standard peak was found at 4.89 ppm. Specifically, the NMR show sharp peaks on top of broader peaks that range from ~2.0 to 0.8 ppm is indicative of ligands attached to the surface.[1-2] For each size QD and each nonsolvent, it is shown that after the first wash the broad underlying peak disappears confirming that a large number of the ligands are removed. The QDs are quoted to have octadecylamine on the surface thus the peaks at 1.0 and 1.40 are most likely due to the octadecylamine however since the original QDs were suspended in hexane this could also contribute signal Generally, quantification of ligand removal is not viable due to overlapping features of the octadecylamine and hexane as detailed above. This does however, provides a qualitative analysis confirms the removal of ligands as seen by SFG, PL, and mass spectrometry measurements (detailed below).

Octadecylamine (ODA)

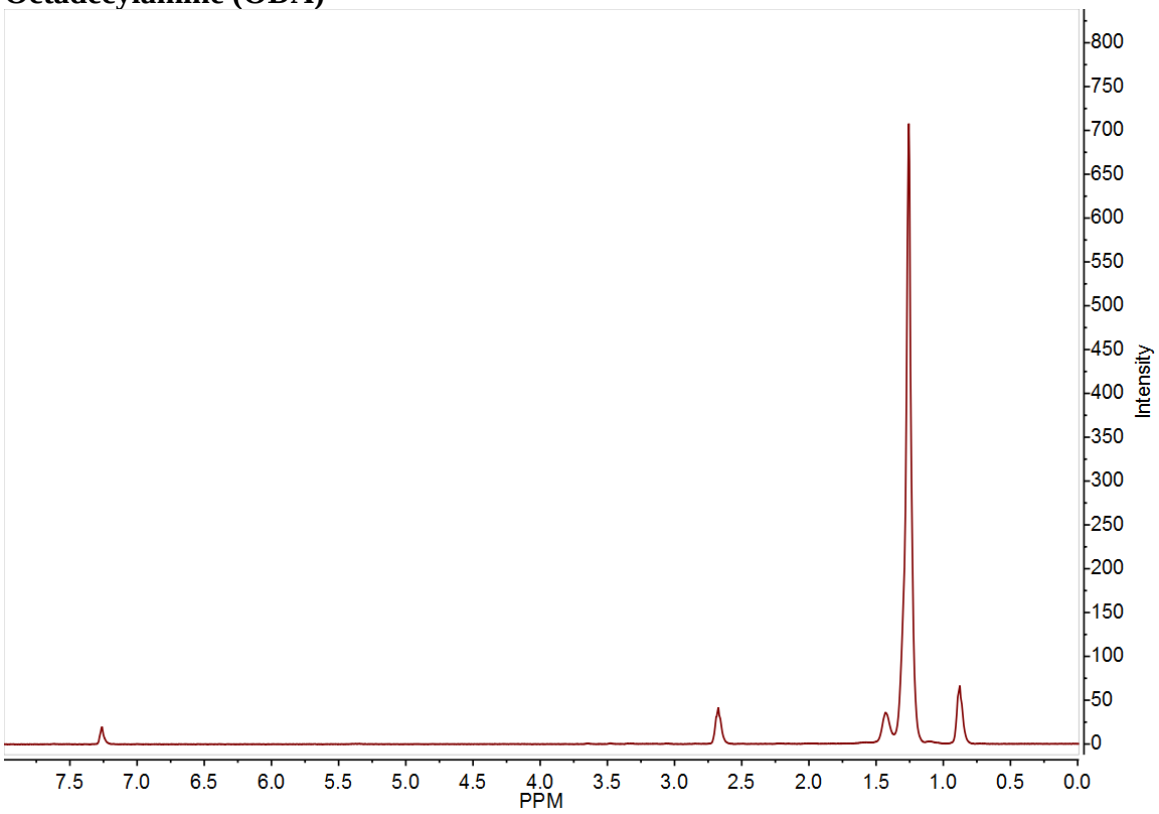

Figure C.6 ^{1}H NMR of octadecylamine in d-chloroform

4.6 nm CdSe QDs Acetone Washes

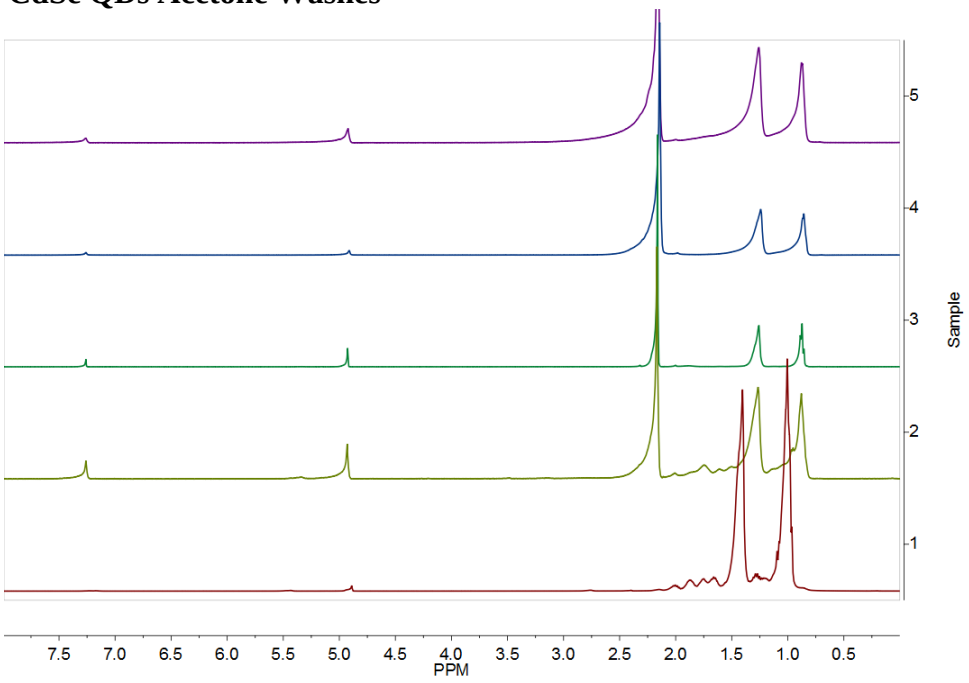

Figure C.7 ^{1}H NMR of 4.6 nm CdSe QDs washed with acetone, 8.0 to 0.0 ppm. Sample 1 refers to unwashed QDs while samples 2-5 are successive washes. Spectra are vertically displaced for clarity

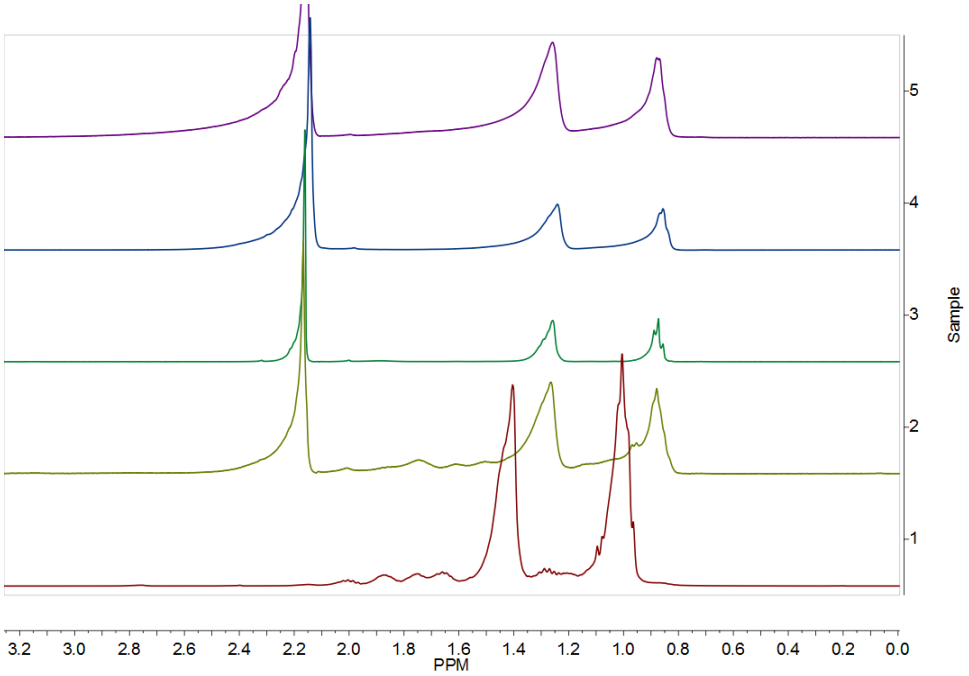

Figure C.8 ^{1}H NMR of 4.6 nm CdSe QDs washed with acetone, 3.25 to 0.0 ppm. Sample 1 refers to unwashed QDs while samples 2-5 are successive washes. Spectra are vertically displaced for clarity.

4.6 nm CdSe QDs Methanol Washes

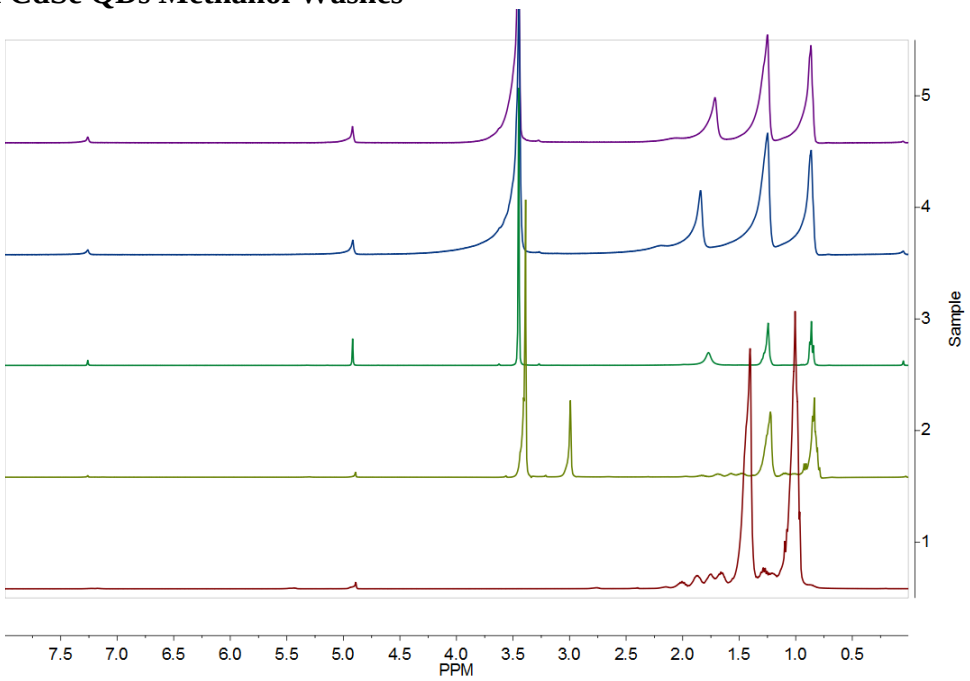

Figure C.9 ^{1}H NMR of 4.6 nm CdSe QDs washed with methanol, 8.0 to 0.0 ppm. Sample 1 refers to unwashed QDs while samples 2-5 are successive washes. Spectra are vertically displaced for clarity

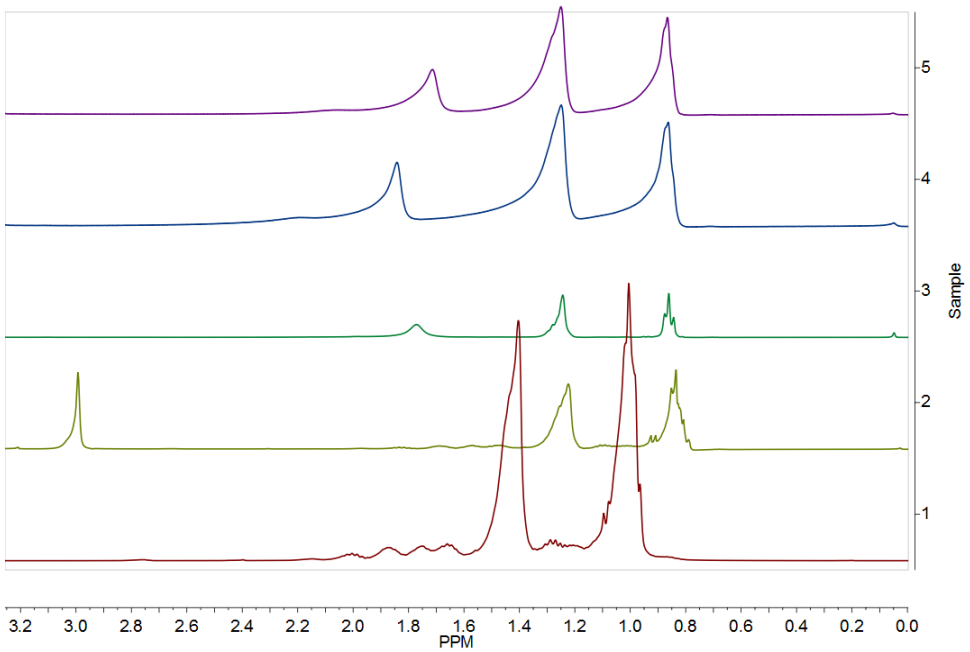

Figure C.10 ^{1}H NMR of 4.6 nm CdSe QDs washed with methanol, 3.25 to 0.0 ppm. Sample 1 refers to unwashed QDs while samples 2-5 are successive washes. Spectra are vertically displaced for clarity

5.6 nm CdSe QDs Acetone Washes

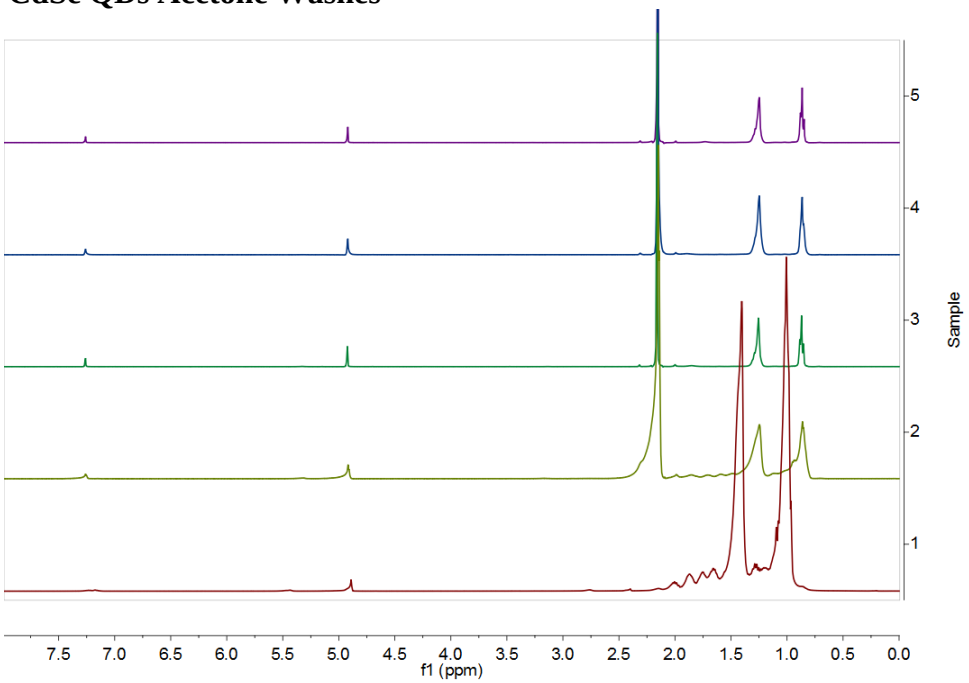

Figure C.11 ^{1}H NMR of 5.6 nm CdSe QDs washed with acetone, 8.0 to 0.0 ppm. Sample 1 refers to unwashed QDs while samples 2-5 are successive washes. Spectra are vertically displaced for clarity

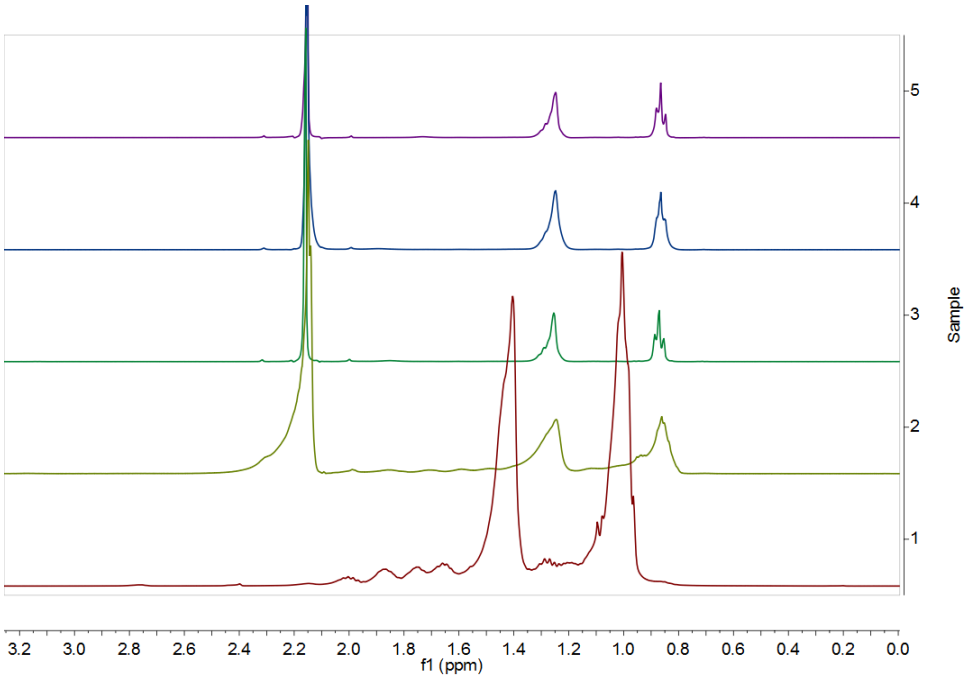

Figure C.12 ^{1}H NMR of 5.6 nm CdSe QDs washed with acetone, 3.25 to 0.0 ppm. Sample 1 refers to unwashed QDs while samples 2-5 are successive washes. Spectra are vertically displaced for clarity

5.6 nm CdSe QDs Methanol Washes

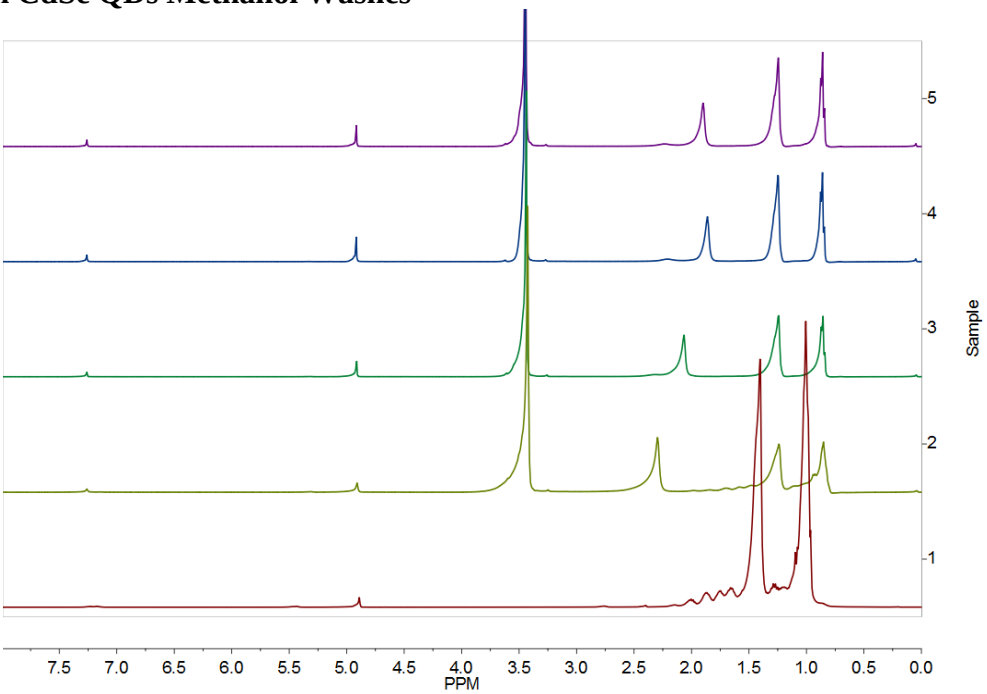

Figure C.13 ^{1}H NMR of 5.6 nm CdSe QDs washed with methanol, 8.0 to 0.0 ppm. Sample 1 refers to unwashed QDs while samples 2-5 are successive washes. Spectra are vertically displaced for clarity

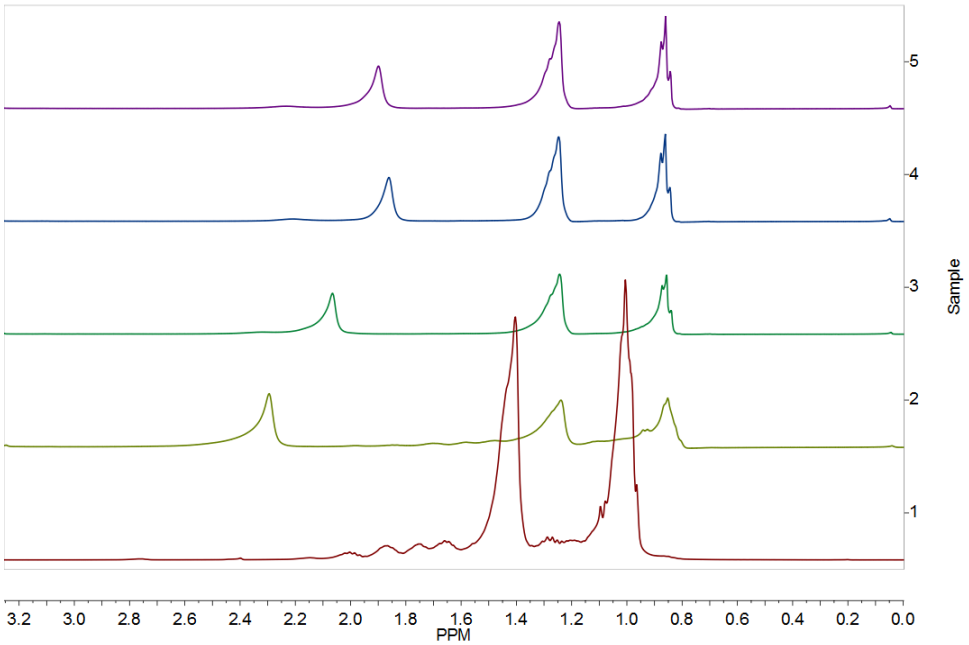

Figure C.14 ^{1}H NMR of 5.6 nm CdSe QDs washed with methanol, 3.25 to 0.0 ppm. Sample 1 refers to unwashed QDs while samples 2-5 are successive washes. Spectra are vertically displaced for clarity

6.9 nm CdSe QDs Acetone Washes

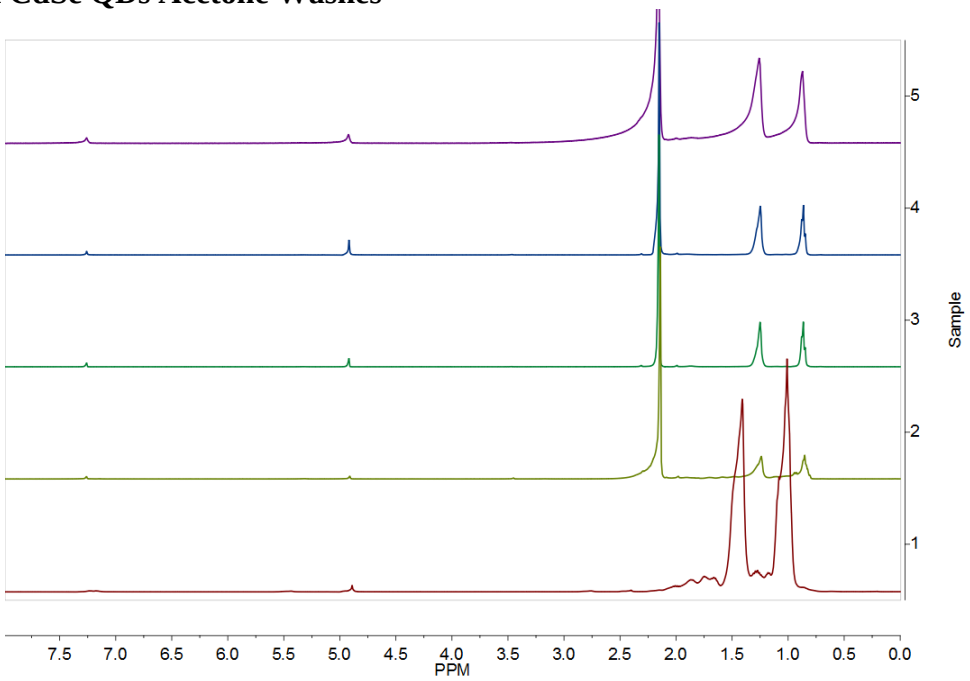

Figure C.15 ^{1}H NMR of 6.9 nm CdSe QDs washed with acetone, 8.0 to 0.0 ppm. Sample 1 refers to unwashed QDs while samples 2-5 are successive washes. Spectra are vertically displaced for clarity

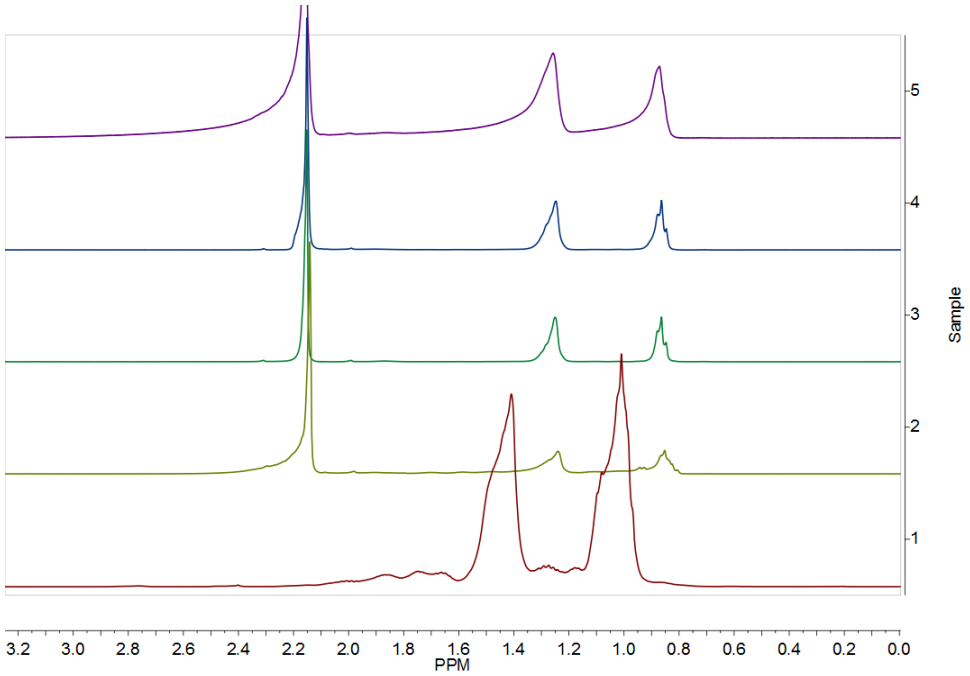

Figure C.16 ^{1}H NMR of 6.9 nm CdSe QDs washed with acetone, 3.25 to 0.0 ppm**.** Sample 1 refers to unwashed QDs while samples 2-5 are successive washes. Spectra are vertically displaced for clarity

6.9 nm CdSe QDs Methanol Washes

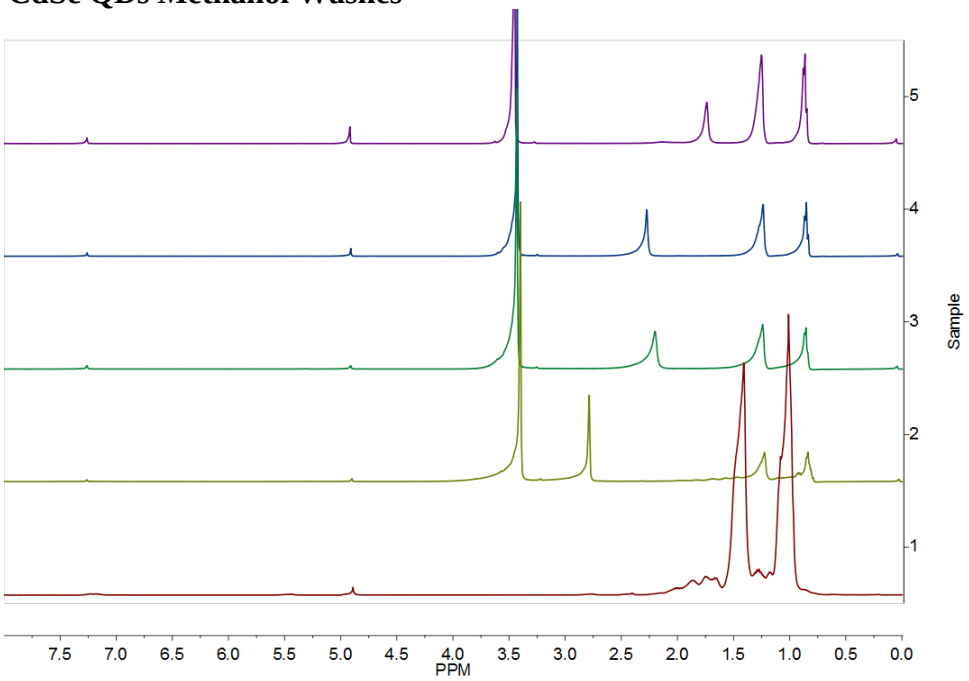

Figure C.17 ^{1}H NMR of 6.9 nm CdSe QDs washed with methanol, 8.0 to 0.0 ppm. Sample 1 refers to unwashed QDs while samples 2-5 are successive washes. Spectra are vertically displaced for clarity

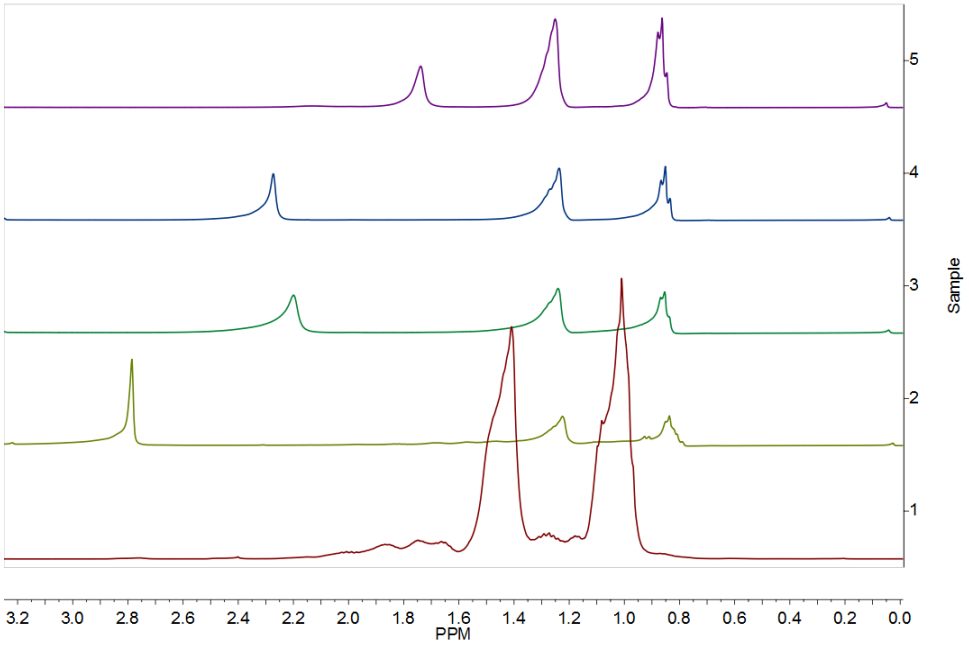

Figure C.18 ^{1}H NMR of 6.9 nm CdSe QDs washed with methanol, 3.25 to 0.0 ppm. Sample 1 refers to unwashed QDs while samples 2-5 are successive washes. Spectra are vertically displaced for clarity

Mass Spectrometry

The presence of octadecylamine (ODA) was confirmed by mass spectrometry through comparison with a 0.24 µM ODA standard. The positive ion electrospray ionization tandem mass spectrum of octadecylamine is shown in SI Figure C.19a. Single reaction monitoring (SRM) scans (mass to charge (*m/z*) 270 → 57 and *m/z* 270 → 85, collision energy = 35 eV, in positive ESI ion mode) were used to confirm the presence of ODA in extracts. SI Figure C.19b shows exemplary ODA signal from 1 µL of supernatant extract 1a (diluted 1000X in methanol + 0.1% formic acid) sampled with the open port sampling interface (200 µL/min methanol + 0.1% formic acid).[3] The data clearly shows ODA signal significantly above background noise. Mass spectra and SRM data were acquired using a SCIEX QTRAP® 5500 mass spectrometer.

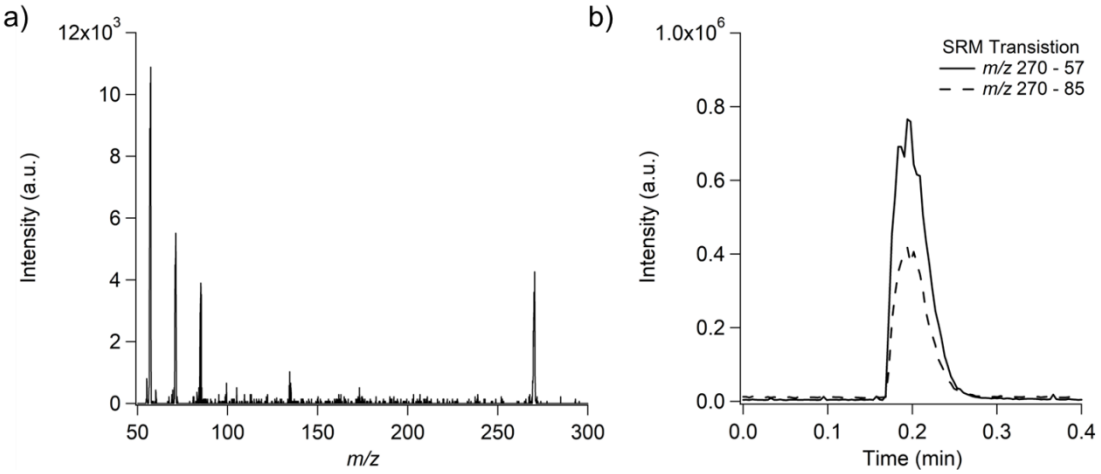

Figure C.19 (a) Tandem ESI mass spectrum of ODA standard. (b) Sampling of 1 µL supernatant extract using open port sampling interface

Packing of Unwashed Samples

Considering the packing and similarity in size of the three samples tested here, the disorder is expected to be very similar for all three sizes as seen below in Figure S20. These results are similar to what has been previously found in the literature.[4-5]

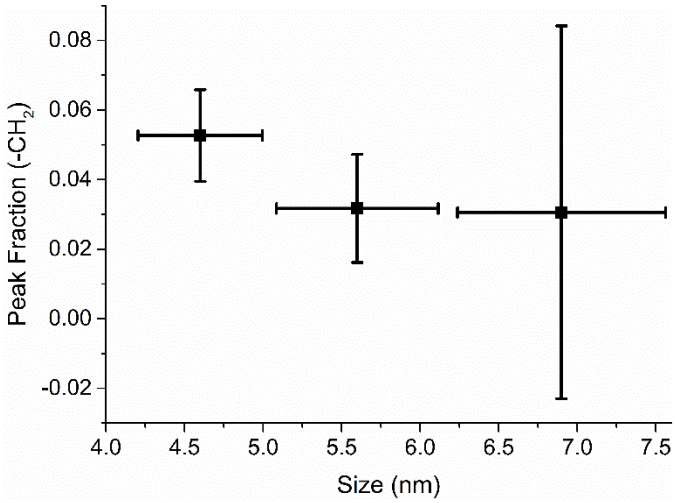

Figure C.20 Peak Fraction of unwashed CdSe QDs

Example of Fitting Curve

Examples of a fitted data are shown below for 6.9 nm quantum dots washed with methanol twice and three times (left and right figure). The raw data is shown in black while the red and the blue curves show fits with unrestricted and restricted parameters, respectively. The shifting in spectral peak position necessitated unrestricted parameters for the fitting.

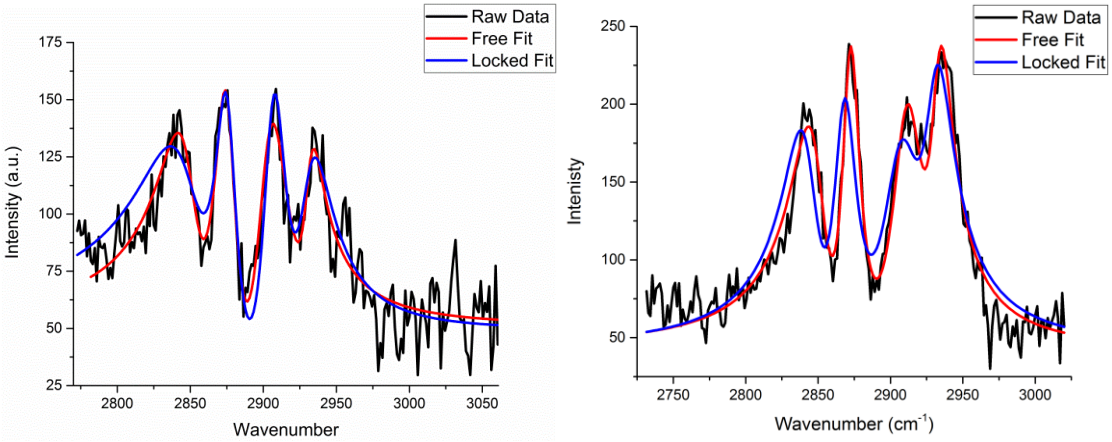

Figure C.21 Free fitting versus locked fit for 6.9 nm CdSe quantum dots with methanol as the nonsolvent

Fitting Values

All vSFG spectra were fitted with four Lorentzians and a nonresonant component. The equation used is shown below in equation 1, where A is amplitude, Γ is line width, ω is frequency. Signal enhancement occurs when the IR pulse is on resonance with the vibrational mode (*v*). Fit amplitude values for the resonant and nonresonant components can be positive or negative depending on the relative phase of overlapping signals.

$$I_{SFG} \propto \left| A_{NR} + \sum_{v}^{N} \frac{A_v}{(\omega_{IR} - \omega_v) + i\Gamma_v} \right|^2 \quad \text{Eq. 1}$$

The tables below show the average of extracted fit parameters from each experimental run fitting for each sample and each size of QD. Frequency (ω), amplitude (A), width (W), and nonresonant components (NR) were tabulated for each trial. For the sample titles, UW refers to the unwashed sample with no ligand removal, while for the remaining sample the letter refers to the nonsolvent and the number refers to the wash number. For example, M1 is the first wash with methanol as a nonsolvent. Peak 1 was assigned as the symmetric $–CH_2$ stretch, Peak 2 as the symmetric $–CH_3$ stretch, Peak 3 as the asymmetric $–CH_2$ stretch, and Peak 4 as the asymmetric $–CH_3$ stretch.

Table C.5 Average fitting parameters for 4.6 nm CdSe quantum dots

4.6 nm	Peak 1			Peak 2			Peak 3			Peak 4			NR
Sample	**ω**	**A**	**W**	**ω**	**A**	**W**	**ω**	**A**	**W**	**ω**	**A**	**W**	
UW	2847.8	11.2	5.2	2867.7	117.6	9.0	2895.6	-70.1	8.4	2907.1	-174.9	9.9	-9.5
M1	2845.2	89.0	14.2	2864.9	59.6	7.0	2905.5	-101.5	9.3	2922.9	-95.6	8.4	-6.9
M3	2846.2	74.8	13.8	2867.5	51.4	6.6	2905.5	-109.5	10.0	2926.0	-79.9	9.4	-6.6
M4	2849.2	77.5	15.7	2870.1	63.2	9.6	2905.3	-110.4	11.3	2925.8	-100.0	11.7	-6.4
A1	2845.2	82.8	15.6	2864.9	41.1	7.4	2904.8	-77.3	8.8	2921.6	-76.2	8.9	-5.4
A2	2847.2	54.3	9.9	2869.6	79.3	12.8	2906.1	-71.1	9.0	2921.9	-116.4	10.9	-6.1
A3	2844.6	60.1	12.4	2869.9	69.9	6.6	2908.2	-102.9	11.3	2929.6	-70.2	7.6	-6.3
A4	2845.7	50.1	12.8	2870.5	57.5	6.5	2911.1	-78.4	12.7	2931.1	-68.2	8.0	-5.0

Table C.6 Average fitting parameters for 5.6 nm CdSe quantum dots

5.6 nm	Peak 1			Peak 2			Peak 3			Peak 4			NR
Sample	**ω**	**A**	**W**	**ω**	**A**	**W**	**ω**	**A**	**W**	**ω**	**A**	**W**	
UW	2849.0	68.7	7.1	2879.3	1217.3	15.5	2885.6	-1645.4	17.1	2904.5	-180.4	9.3	-16.2
M1	2841.0	97.1	15.1	2863.2	130.7	7.9	2897.6	-198.6	11.1	2918.7	-125.7	11.6	-6.9
M2	2839.7	82.4	13.1	2863.4	72.1	6.3	2908.2	-51.6	8.3	2926.3	-154.8	9.3	-5.1
M3	2838.2	81.9	18.2	2862.1	49.7	5.5	2902.2	-65.6	9.1	2924.8	-118.5	10.0	-4.5
M4	2839.0	79.9	13.2	2864.2	72.3	6.6	2903.1	-109.4	11.1	2926.5	-101.6	8.7	-6.2
A1	2848.5	85.8	18.7	2869.0	94.1	8.0	2893.0	-218.2	17.4	2923.6	-48.4	10.0	-9.0
A2	2840.6	78.9	13.6	2863.6	77.0	6.8	2910.2	-70.9	10.0	2925.7	-117.5	8.1	-6.0
A3	2840.5	81.2	13.2	2863.4	71.4	6.6	2909.0	-61.6	10.2	2925.7	-128.3	8.8	-5.5
A4	2839.5	56.2	10.8	2866.3	88.0	6.2	2907.7	-70.2	11.1	2928.5	-114.2	7.8	-5.7

Table C.7 Average fitting parameters for 6.9 nm CdSe quantum dots

6.9 nm	Peak 1			Peak 2			Peak 3			Peak 4			NR
Sample	**ω**	**A**	**W**	**ω**	**A**	**W**	**ω**	**A**	**W**	**ω**	**A**	**W**	
UW	2852.1	14.2	7.9	2877.7	1107.0	14.3	2884.5	-1374.9	13.8	2904.1	-122.5	11.4	-12.9
M1	2839.1	25.6	14.1	2874.1	168.7	15.9	2890.4	-206.6	13.6	2916.3	-18.4	4.6	-8.3
M2	2840.3	50.8	16.0	2865.7	83.8	11.6	2895.9	-110.2	11.5	2918.8	-58.7	9.7	-6.8
M3	2848.8	64.3	14.4	2874.2	107.0	10.0	2907.2	-167.8	13.4	2929.6	-85.5	10.6	-7.6
M4	2851.2	18.5	13.7	2878.6	109.6	14.7	2908.4	-111.4	13.4	2930.1	-85.1	11.6	-6.2
A1	2841.4	36.8	16.0	2876.0	226.7	13.5	2894.1	-283.3	13.8	2922.5	-26.3	12.0	-9.8
A2	2837.1	38.8	16.0	2865.1	75.1	7.4	2895.8	-108.3	15.5	2922.0	-46.4	8.1	-6.3
A3	2844.4	48.3	14.1	2871.2	80.6	6.5	2914.0	-29.2	8.2	2934.1	-170.6	10.8	-5.2
A4	2834.3	42.3	16.0	2863.9	73.1	6.5	2902.7	-57.4	12.2	2924.3	-85.0	8.1	-5.2

Peak Position

Average frequency position of fitted peaks for each size quantum dots and nonsolvent. Spectral shifting of peaks was observed between sizes and nonsolvent used, as can be seen in the Tables below.

Table C.8 Average frequency position for 4.6 nm CdSe quantum dots

4.6 nm CdSe	**-CH_2,*s***	**-CH_3,*s***	**-CH_2,a*s***	**-CH_3,*as***
Methanol	2847	2867	2902	2919
Acetone	2846	2868	2904	2921

Table C.9 Average frequency position for 5.6 nm CdSe quantum dots

5.6 nm CdSe	**-CH_2,*s***	**-CH_3,*s***	**-CH_2,a*s***	**-CH_3,*as***
Methanol	2842	2867	2899	2919
Acetone	2844	2869	2900	2921

Table C.10 Average frequency position for 6.9 nm CdSe quantum dots

6.9 nm CdSe	**-CH_2,*s***	**-CH_3,*s***	**-CH_2,a*s***	**-CH_3,*as***
Methanol	2847	2875	2895	2917
Acetone	2843	2872	2896	2918

Spectral Shift

Peak position shift for fitted SFG spectra for each trial of each size quantum dot and nonsolvent. For each size the left figure shows acetone as a nonsolvent and the right figure shows methanol as the nonsolvent. As shown in the figures there are shifts in all the peak positions. These shifts are attributed to differences in solvation environment which is altered by not only the number of ligands at the surface but also drying the sample of the quartz plate.

CdSe (4.6 nm) Peak shifts

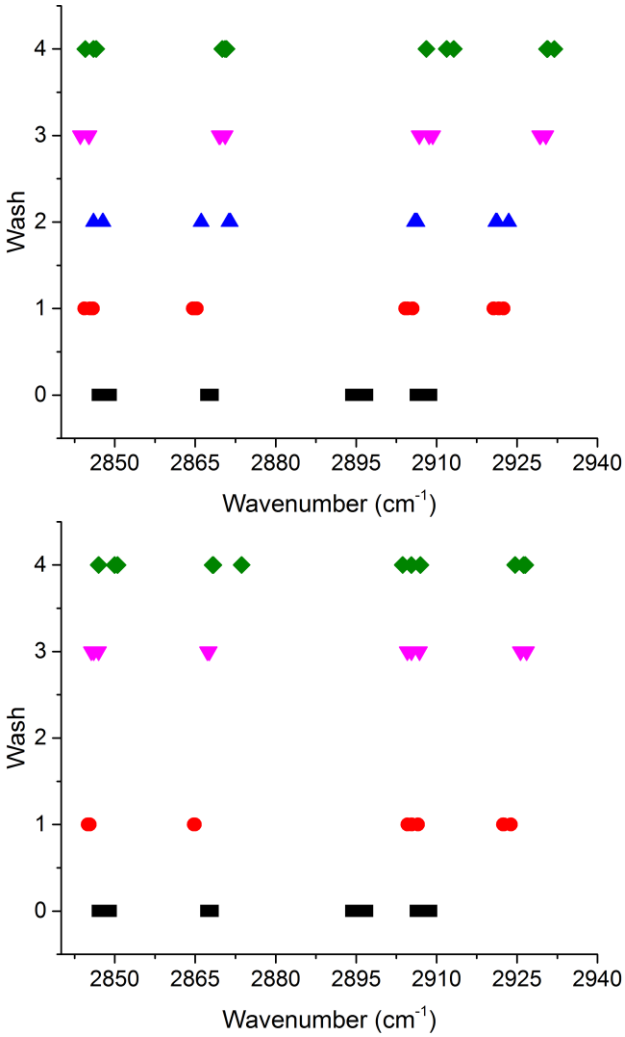

Figure C.22 Spectral shift of fitted peak positions for 4.6 nm CdSe quantum dots with acetone (left) and methanol (right) as the nonsolvent

CdSe (5.6 nm) Peak shifts

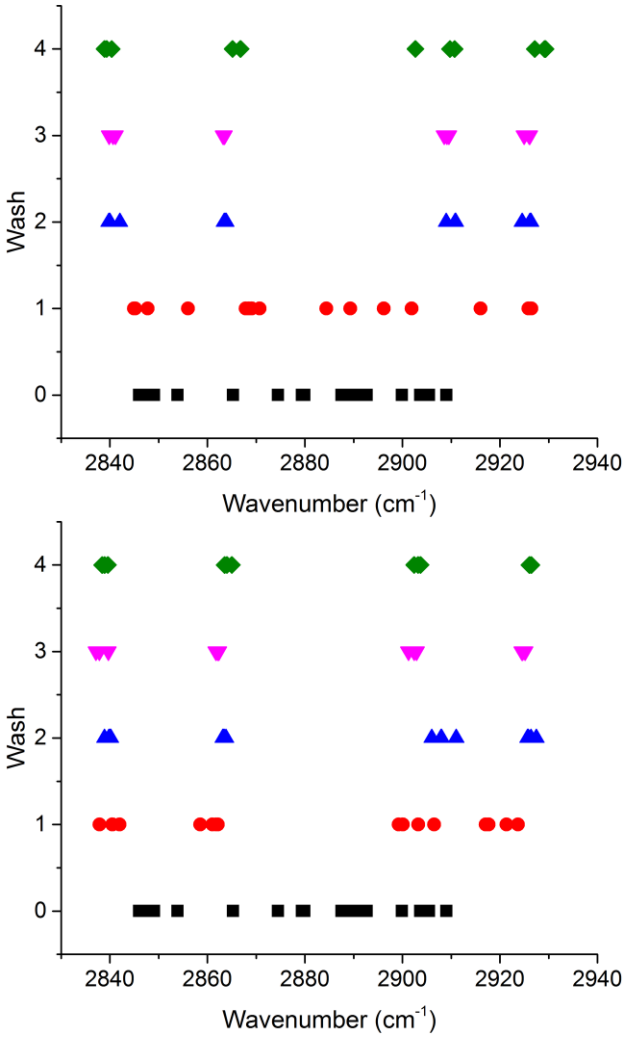

Figure C.23 Spectral shift of fitted peak positions for 5.6 nm CdSe quantum dots with acetone (left) and methanol (right) as the nonsolvent

CdSe (6.9 nm) Peak Shifts

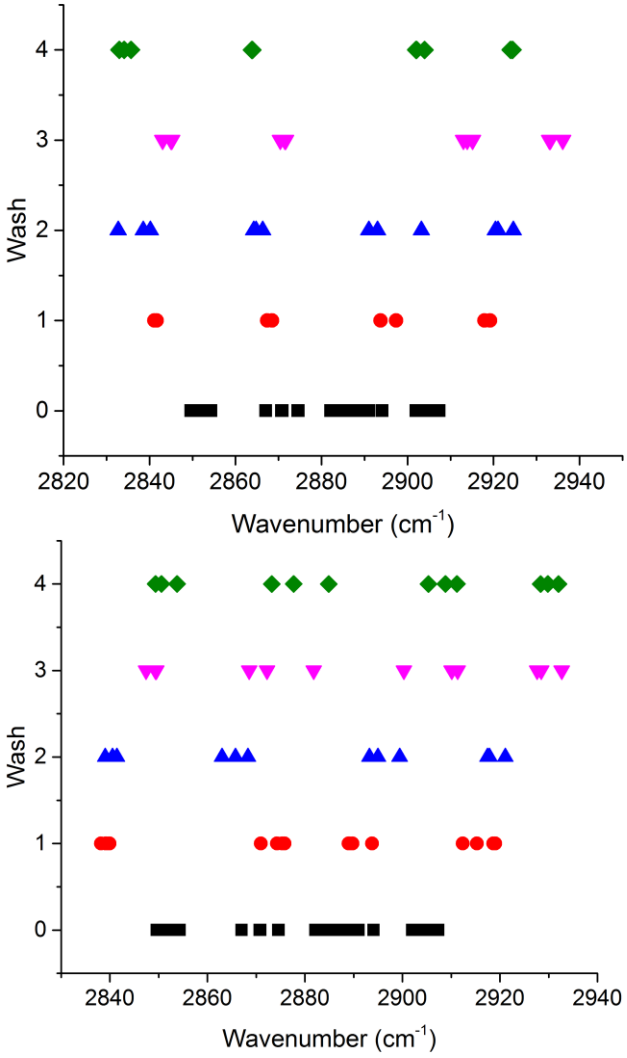

Figure C.24 Spectral shift of fitted peak positions for 6.9 nm CdSe quantum dots with acetone (left) and methanol (right) as the nonsolvent

Table C.11 Spectral shift (in cm^{-1}) from unwashed peak positions

		CdSe600		CdSe620		CdSe640	
	Wash	*Acetone*	*Methanol*	*Acetone*	*Methanol*	*Acetone*	*Methanol*
Peak 1	1	-2.6	-2.6	-0.5	-8.0	-10.8	-13.0
	2	-0.6	-	-8.4	-9.3	-15.0	-11.8
	3	-3.2	-1.6	-8.5	-10.8	-7.7	-3.4
	4	-2.1	1.3	-9.5	-10.0	-17.9	-0.9
Peak 2	1	-2.7	-2.8	-10.3	-16.1	-1.6	-3.6
	2	2.0	-	-15.7	-15.9	-12.5	-11.9
	3	2.2	-0.2	-16.0	-17.3	-6.5	-3.5
	4	2.8	2.4	-13.1	-15.1	-13.8	0.9
Peak 3	1	9.2	9.9	7.4	12.0	9.6	5.9
	2	10.6	-	24.7	22.7	11.3	11.4
	3	12.7	10.0	23.5	16.6	29.5	22.7
	4	15.5	9.8	22.1	17.5	18.2	23.9
Peak 4	1	14.5	15.8	19.1	14.2	18.4	12.3
	2	14.8	-	21.2	21.8	18.0	14.7
	3	22.5	18.9	21.2	20.2	30.0	25.5
	4	24.0	18.7	24.0	21.7	20.2	26.0

Example Spectra with Acetone as the Nonsolvent

The example spectra below are for 5.6 nm CdSe washed with acetone. The spectra do not indicate adsorption of acetone to the surface of the particles. Acetone would be expected to produce a peak between 2920-2925 cm^{-1} which is absent in the measured data.

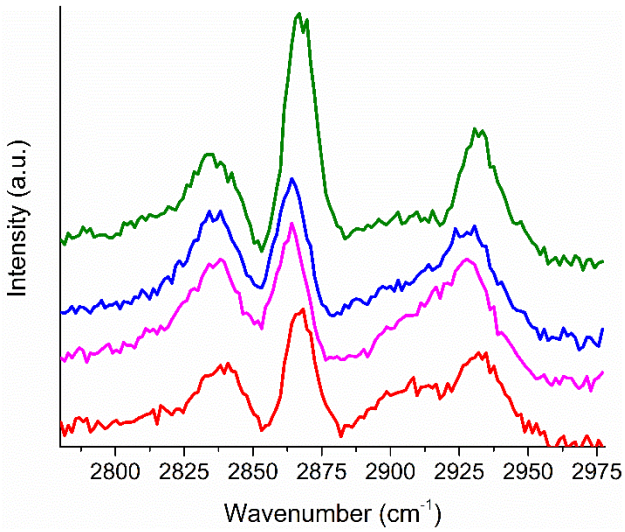

Figure C.25 Example vSFG spectra for 5.6 nm CdSe washed with acetone as the nonsolvent one (red), two (pink), three (blue), or four (green) time

References

1. Cooper, J. K.; Franco, A. M.; Gul, S.; Corrado, C.; Zhang, J. Z., Characterization of Primary Amine Capped CdSe, ZnSe, and ZnS Quantum Dots by FT-IR: Determination of Surface Bonding Interaction and Identification of Selective Desorption. *Langmuir* **2011,** *27* (13), 8486-8493.

2. Ji, X.; Copenhaver, D.; Sichmeller, C.; Peng, X., Ligand Bonding and Dynamics on Colloidal Nanocrystals at Room Temperature: The Case of Alkylamines on CdSe Nanocrystals. *J. Am. Chem. Soc.* **2008,** *130* (17), 5726-5735.

3. Van Berkel, G. J.; Kertesz, V., An open port sampling interface for liquid introduction atmospheric pressure ionization mass spectrometry. *Rapid Commun. Mass Spectrom.* **2015,** *29* (19), 1749-1756.

4. Bordenyuk, A. N.; Weeraman, C.; Yatawara, A.; Jayathilake, H. D.; Stiopkin, I.; Liu, Y.; Benderskii, A. V., Vibrational Sum Frequency Generation Spectroscopy of Dodecanethiol on Metal Nanoparticles. *J. Phys. Chem. C* **2007,** *111* (25), 8925-8933.

5. Frederick, M. T.; Achtyl, J. L.; Knowles, K. E.; Weiss, E. A.; Geiger, F. M., Surface-Amplified Ligand Disorder in CdSe Quantum Dots Determined by Electron and Coherent Vibrational Spectroscopies. *J. Am. Chem. Soc.* **2011,** *133* (19), 7476-7481.

VITA

Brianna Watson was born in Dayton, Ohio to Lesle and Gary Watson. She attended primary school at St. Anthony School and completed her secondary education at Carroll High School. During her time at Carroll high school she was a varsity athlete in both cross-country as well as track and field. At Wittenberg University she received her Bachelors of Science in Chemistry as well as minors in Russian Language and Russian Central Eurasian Studies in 2013. She began to pursue her Doctor of Philosophy of Chemistry in the same year. She completed her PhD in 2018.